論文 / 著書情報
Article / Book Information

題目(和文)	
Title(English)	An Ultra-Low-Power Miniaturized Atomic Clock Based on CMOS Frequency Probing and Synchronization Loop
著者(和文)	ZhangHaosheng
Author(English)	Haosheng Zhang
出典(和文)	学位:博士(学術), 学位授与機関:東京工業大学, 報告番号:甲第11353号, 授与年月日:2019年12月31日, 学位の種別:課程博士, 審査員:岡田 健一,髙木 茂孝,波多野 睦子,德田 崇,伊藤 浩之,柳町 真也 ,五箇 繁善
Citation(English)	Degree:Doctor (Academic), Conferring organization: Tokyo Institute of Technology, Report number:甲第11353号, Conferred date:2019/12/31, Degree Type:Course doctor, Examiner:,,,,,,
学位種別(和文)	博士論文
Type(English)	Doctoral Thesis

An Ultra-Low-Power Miniaturized Atomic Clock Based on CMOS Frequency Probing and Synchronization Loop

by

Haosheng Zhang

A Ph.D. dissertation submitted in partial fulfillment of the requirements for the degree of

Doctor of Philosophy

in

Department of Electrical and Electronic Engineering

in the

Graduate School of Science and Engineering

of

Tokyo Institute of Technology

Supervised by

Professor Kenichi Okada

Winter, 2019

To my family

Acknowledgment

It has been a meaningful and interesting journey for the past five years I spent in this lab as a Ph.D. candidate. Not only plenty of academic rewarding and knowledge but also I have gained much precious friendship and partnership during various challenging projects. It was very lucky for me to settle in such a nice and comfortable place and did so many fancy projects here. Having the chance to access the state-of-art equipment and discuss the techniques problems with intelligent guys in this lab makes me always feel grateful and excited.

I would like to take this special opportunity to thank so many people who have helped and supported me throughout my study in Okada Laboratory, Tokyo Institute of Technology. I will keep this deep in my heart and use it as a consistent impulse to motivate myself and move on to face the following challenges in my career.

First and foremost, I would like to show my highest respects and appreciations to my principal advisor, Prof. Kenichi Okada, who continuously gives me valuable guidance, encouragement, and of course the financial support throughout my study and research in this lab. His passionate commitment to education and research always inspires me for a better solution and progress. Prof. Okada is also very patient and kind to discuss with me on various matters I have met in Japan, which saves me out of a lot of trouble. I take this opportunity to extend my heartfelt thanks for his help.

I would also like to thank Prof. Akira Matsuzawa for his invaluable guidance, countless advice, and also the rich knowledge and experience that he shared with me throughout my research.

I would like to thank my Ph.D. committee members, Prof. Shigetaka Takagi, Prof. Mutsuko Hatano, Prof. Takashi Tokuda, Prof. Hiroyuki Ito, Dr. Shinya Yanagimachi, and Prof. Shigeyoshi Goka for taking the time out of their busy schedule to examine my dissertation and provide lots of valuable advice.

I would like to thank Prof. Atsushi Shirane for his invaluable advice on my research and also many technical supports. And also I would like to thank Yoshino Kasuga and Ayumi Okubo for their kindly help on applications, documents and travel procedures for conferences and workshops during the past five years.

I am also grateful to Dr. Aravind Tharayil Narayanan, Hans Herdian, Dr. Yun Wang, Dr. Bangan Liu and Dr. Jian Pang, Zheng Sun, Yuncheng Zhang, Ibrahim Imad Ibrahim Abdo, Zheng Li, Hongye Huang, Chun Wang, Dongwon You, Xi Fu for their remarkable supports on co-research.

I would like to thank all the lab members, who have supported me with technical discussion and personal help.

Finally, I thank my family for their great support and love.

Abstract

This dissertation presents one chip-scale ultralow-power atomic clock (ULPAC) in the microwave frequency region. Highly stable frequency standard is essential for high-performance networks such as smart power grids, accurate and robust navigation, self-clocked long-time data logging, scientific metrology, and sensing applications. Widely deployed electro-mechanical oscillators such as the quartz crystal and micro-electro-mechanical systems (MEMS) resonators suffer from large frequency shifts due to the high sensitivity of the resonance frequency to external or internal factors. The typical long-term stability of such electro-mechanical oscillators is well below the parts-per-billion level (10^{-9}).

For decades, atomic oscillators have been the sole choice in applications requiring ultra-high precision clocks. The superior frequency stability of atomic clocks can be attributed to the fact that the frequency is determined by the transition of energy levels of atoms. However, adopting the conventional atomic clocks for portable and mobile applications, such as the low-earth-orbit (LEO) small satellite (smallsat) constellations, presents numerous challenges due to the requirements for compact and power-efficient implementation for probing the atomic resonance and preserving the coherence of atoms.

The demonstration of the ULPAC prototype provides one compact, transportable and low-cost frequency standard with atomic grade frequency stability performance, which will enhance or enable various portable and mobile applications. One new suspended compact quantum package architecture along with a fully integrated frequency probing and locking loop implemented in CMOS technology results in a small form-factor package and ultralow-power consumption. In addition, dedicated low-noise magnetic field and temperature control loops are incorporated for isolating and mitigating the internal and external factors affecting the frequency stability. The output frequency of a crystal oscillator is continuously compensated and stabilized by locking to the peak of a coherent population trapping signal, thereby inheriting the superior frequency stability of the atomic clock. The proposed ULPAC system achieves a frequency stability of 2.2×10^{-12} at an averaging time of 10^5 s, while consuming 59.9 mW. The frequency probing and locking circuit implemented in a standard 65-nm CMOS process node occupies an area of

2.55 mm^2. The prototype of this atomic clock occupies a volume of 15 cm^3.

This thesis gives detailed information about the implementation of ULPAC as well as the quantum physical principle behind the tiny atomic clock. Various internal or external perturbations to the frequency stability are analyzed along with the trade-offs of various potential solutions. A throughout characterization of the ULPAC is provided, indicating the robustness, low power and high-frequency stability performance of this work. Besides, ultralow-power circuits such as highly power-efficient CMOS oscillator and injection-locked PLL are proposed to develop next-generation ULPAC targeting power consumption below 25 mW. Finally, potential promising quantum technologies for compact atomic clocks such as laser cooling and optical transition are introduced to achieve better frequency stability performance in the near future.

Contents

List of Figures

List of Tables

Chapter 1

Introduction

Time, as a fourth dimension, plays a ubiquitous role in the physical world and has been an essential subject of study in almost every aspect of human being's activities. In ancient times, the calendar is closely related to agriculture activities. The beginning of the calendar could data back to 6,000 years ago when the moon was used to reckon time [14]. Since then, more accurate and stable methods for measuring and keeping track of time have been discovered or invented such as the sundial, pendulums, crystal oscillator and so on to meet the requirements of new applications or enhance the performance of existing applications.

The brief history of clock development progress of the past 400 years is shown in Fig. 1.1. The pendulum clock was invented in 1656 by the Dutch scientist and inventor Christiaan Huygens. He was inspired by investigations of pendulums done by Galileo Galilei. Galileo discovered that the period of swing of a pendulum is approximately the same for different sized swings [15]. The invention of Harrison chronometer was a milestone for voyage navigation. In the year of 1714, the British government started a contest with financial rewards to seek the solution for determining the longitude at sea [16], where the pendulum can not be used due to the high-frequency sensitivity caused by the temperature and mechanical variations. John Harrison came up with one idea to compensate for the temperature-induced frequency shift by interweaving two materials with opposite temperature coefficients. With estimated time error around 350 ms per day, the Harrison chronometer was accurate enough to reduce navigation errors to acceptable levels for navigation at sea. The Shortt clock was a complex precision electromechanical pendulum clock invented in 1921 by William Hamilton Shortt in collaboration with horologist Frank Hope-Jones. The Shortt clock was the most accurate pendulum clock ever commercially produced and became the highest standard for timekeeping between the 1920s and the 1940s, after which mechanical clocks were superseded by quartz time standards [17].

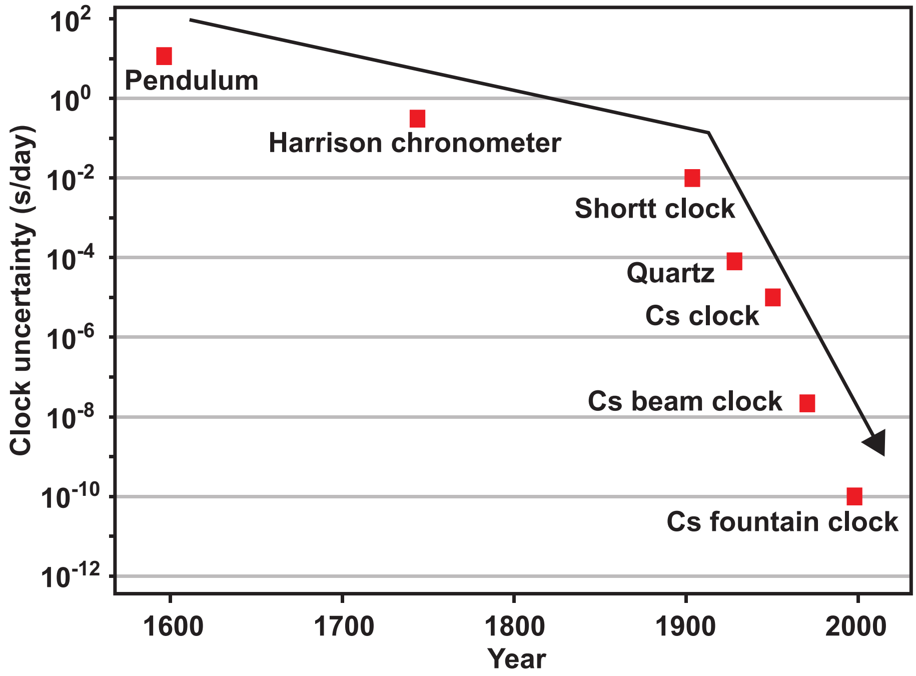

Figure 1.1: History of clock development progress [1].

Quartz crystal oscillators operate based on the piezoelectric effect, whereby mechanical deformation of the crystal induces charge accumulation on the crystal surface. The coupling between crystal strain and electric field results in electromechanical resonance at a frequency determined by the crystal dimensions. Quartz crystal oscillators have been widely used as a reference source in modern electronics due to low cost, relatively small size and high-quality factor compared with on-chip LC-oscillator. However, the long-term frequency stability of crystal oscillators suffers from temperature dependence, aging, and sensitivity to mechanical vibrations. Various package and isolation techniques have been proposed and designed for crystal oscillators to overcome the poor long-term frequency stability performance, such as oven compensated crystal oscillator (OCXO), microcomputer compensated crystal oscillator (MCXO) and temperature compensated crystal oscillator (TCXO) [18]. Until the mid of the last century, the first atomic clock was finally introduced. The operation of the atomic clock is based on transitions between two energy levels of a particular atom. At present, there is no experimental evidence indicating that the properties of atoms change with the variation of space and time (except for relativistic effects). Therefore, the energy transition, as well as the frequency relating to the energy transition, is assumed to be constant [6]. The most stable primary frequency standards so far in the world are atomic clocks, which have been reported to achieve frequency uncertainty as low as 1.4×10^{-18} [19].

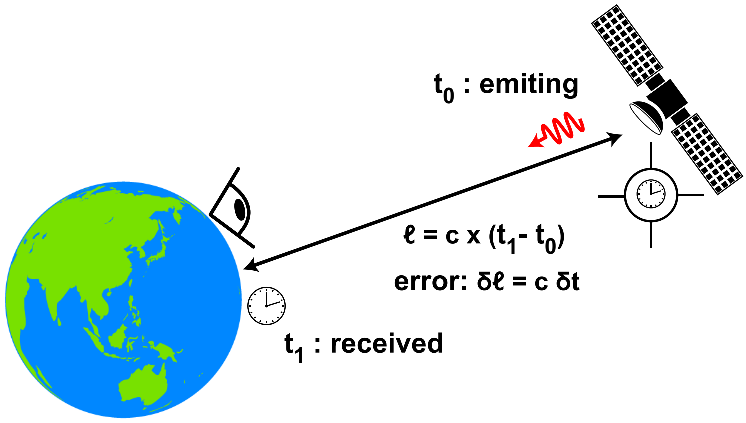

Figure 1.2: Illustration of navigation error for global positioning system.

Along with the development progress of clock technologies, the advancement of science and technology has been driven, in part, by improvements in timekeeping devices. The new timekeeping technologies with better frequency stability and higher accuracy could always enable or enhance various applications. One example is the global navigation satellite system (GNSS). Nowadays, the world is increasingly dependent on the GNSS to provide accurate and stable positioning, navigation and timing services and enable related applications such as autonomous vehicles. The accuracy or precision of GNSS such as the global positioning system (GPS) critically relies on the timing accuracy of the onboard clock, as illustrated by Fig. 1.2. Even if the clock used in the GPS only has a timing error of $1\,\mu$s, the estimated navigation uncertainty would be approximately $300\,$m. The ever-increasing of data rates of the next-generation wireless communication system also demands an ultra-high purity clock source for accurate and tight timing/phase synchronization [20]. And large-scale high-performance networks such as smart power grids or unmanned-aerial-vehicle base stations (UAV-BS) require a strict hold-over time performance [21]. Besides, the highly stable clock is essential for scientific research facilities as well such as particle accelerators and gravitational-wave interferometers [22, 23]. Scientists have become very interested in being able to observe the dynamics of a simple quantum system in most elemental form, which could indicate that the evolution may not be as originally expected. Such kind experiments could indicate and lead to new physics [24–27]. Comparing resonance frequencies of different atoms or molecules may make such effects observable [28]. Thus, the science and technology of timekeeping have been under a long history of consistent pursuit of human beings.

The essential key of timekeeping or timing measure is to obtain a dynamic object or in more precise words, a resonator, based on which the time is tracked by counting the number of the repeats of the periodic dynamics or the resonating cycles. Thus, a more stable and accurate resonator could lead to a better timing keeping device. Widely used crystal oscillator is accurate enough for various electronic systems. But it displays a large frequency shift due to internal or external factors and fails to serve as a long-time stable clock source for high-performance applications, such as GPS. For decades, atomic oscillators have been the sole choice in applications requiring ultra-high precision clocks. However, adopting the conventional atomic clocks for portable and mobile applications presents numerous challenges due to the requirements for compact and power-efficient implementation for probing the atomic resonance and preserving the coherence of atoms. Thus, the new clock technology for high-speed communication, long hold-over networks, and small satellite (smallsat) constellations should embrace a low power and compact package of crystal oscillator, while inheriting the frequency stability of atomic resonator. Recent developments in the photonics and micro-electro-mechanical systems (MEMS) processes show the potential to realize low power consumption and small volume quantum physical package of the atomic clock. Such kind pursuit was first initiated around two decades ago by the National Institute of Standards and Technology (NIST) and active research is still kept going on to fulfill the concept and target of chip-scale atomic clock.

This chapter explains why the atomic clock could demonstrate a superior frequency stability performance as compared with other types of resonators such as electromechanical oscillators. Regarding the implementation complexity and field deployments, the research motivation and perspective of chip-scale ultralow-power atomic clock (ULPAC) are introduced with a summary of the state-of-arts of chip-scale atomic clock or chip-scale molecular clock. The scopes and innovations of ULPAC presented in this thesis are briefly introduced.

1.1 Motivation and Perspective

1.1.1 On-board clock for smallsat constellations

The motivation of this work is to develop a new clock technology for the smallsat constellation, which requires low power, small volume and atomic grade frequency stability clock performance.

Since the beginning of this century, many industrial efforts have been made to deploy the low-earth-orbit (LEO) satellites constellation, as shown in Fig. 1.3. For example, the OneWeb satellite constellation is an initial 650-satellite constellation currently being built out to provide global satellite Internet broadband services. And the Starlink project underway by SpaceX already launched the first 60 operational satellite just in the year of

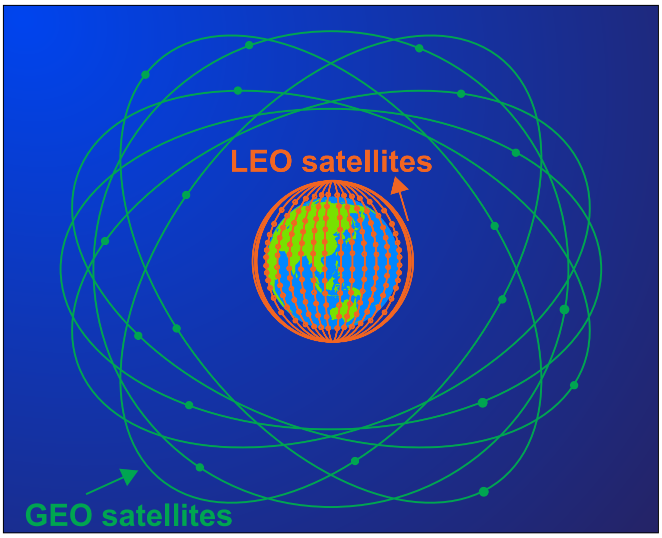

Figure 1.3: Low-earth-orbit (LEO) small satellite (smallsat) constellation and geosynchronous (GEO) satellite constellation

2019 with a plan of 12000 satellites by the mid of 2020s. Compared with the geosynchronous (GEO) satellites, the LEO satellite constellation is much closer to the earth. It can provide the following benefits as compared with the GEO satellite constellation. First, it can easily provide global service such as the Internet or communications because it is not stationary to the earth. Also, it can provide on-demand high-speed communication due to small path delays or enhance the performance of the GNSS like GPS. In the near future, the services provided by such constellations will become increasingly ubiquitous in our society.

The so-called smallsats are adopted in this system for economical and quick deployment considerations. This puts very strict requirements on the board clock. First, the clock should consume very low power consumption. This is because the solar energy obtained by such satellites is quite limited due to the short time exposed to the sun. The volume should be as small as possible because the payload is a very precious resource for such kind small satellite. Last but not least is that excellent frequency stability should be maintained for accurate timing synchronization. For the services like accurate navigation, even 1 µs time error will lead to around 300 m navigation uncertainty. If translating this time error into frequency stability averaged at one day, it is approximately 10^{-11} [29].

The strict timing synchronization requirement of the LEO smallsat constellation limits the choice of clock to be only the atomic clock. The most common commercial compact atomic clock is the Rb frequency standard based on optical pumping [30]. In such a system, a discharge lamp is used, which typically consumes approximately 1 W. An external cavity diode laser (ECDL) can be used instead of the discharge lamp to improve the frequency stability, but the clock still suffers from large power consumption [31]. The microwave cavity used for coupling the radio frequency (RF) signal to the atom ensemble has a minimum size requirement of approximately 0.1 L [32], limiting the volume of such a frequency standard ranging from $155\,\mathrm{cm}^3$ to $755\,\mathrm{cm}^3$. The requirements for on-board clocks for an LEO smallsat are not satisfied by the Rb frequency standard. Thus, innovations on the architecture of compact quantum physical package and ultralow-power frequency probing and locking loop are mandatory to minimize the volume and reduce the power consumption for the clock technology of the LEO smallsat.

The ULPAC presented in this thesis aims to develop one such a clock technology to fulfill the strict requirement of the LEO smallsat with a long-term frequency stability in the level of 10^{-12} and a volume of $15\,\mathrm{cm}^3$, while consuming less 100 mW.

1.1.2 Perspective for ULPAC technology

This miniaturized low power clock technology with an atomic grade performance could be adopted in many existing portable and mobile applications to enhance the system performance, while it can also enable various new applications.

Holdover time of high performance network

It can be used to improve the holdover performance of large-scale high-performance networks, like the power substation local area networks (LANs), wireless network, professional mobile radio, data center, and high-frequency trading [33, 34]. In such networks, strict phase/time synchronization is required with holdover time typically longer than 24 hours. For 1 μs phase/time synchronization requirement, even the OCXO can only maintain within tens of minutes, while the ULPAC could extend the holdover time to several days. For the base stations in the 5G systems, the required time synchronization is as small as 130 ns [35]. The beamforming and multiple-input and multiple-output (MIMO) architectures for supporting high data rates also require very stringent time synchronization and distributions, otherwise the performance will degrade or complicated phase/time mismatch calibration is required. Even though the base station clock can be disciplined by a GPS signal, the jamming concerns, coverage issues, and indoor layout limit the practicality of this solution. An alternative approach would be to build a dedicated precision time protocol networks for distributing time synchronization signals from a primary reference such as ULPAC presented in this thesis.

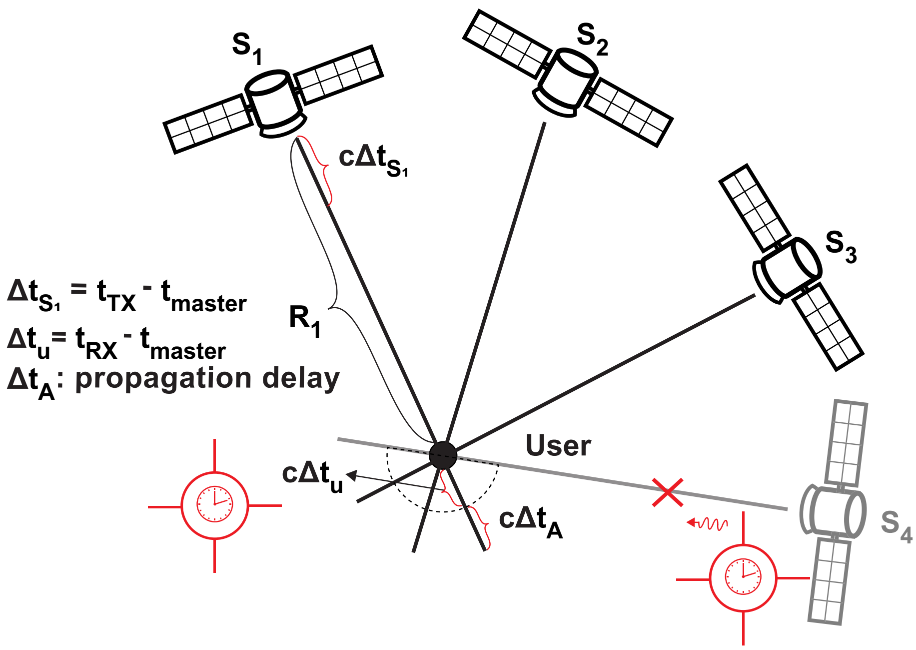

Figure 1.4: Navigation with less than four satellites.

Time stamp for GPS denied environments

An accurate timestamp is required for long-time data logging of large sensor arrays, especially where the GPS signal is not available. This is the case for the ocean bottom seismographs or remote area monitoring sensors. One example will be the oil exploration by deploying a large array of sensors [36]. By correlating the time-stamped reflection data of acoustic pulses, a map of the ocean floor including predicted oil fields can be reconstructed. Since such sensors are deployed for long periods, the clocks should have good long-term frequency stability to provide accurate time stamp for the required accuracy for the reconstructed seafloor map.

Navigation

It could be further adopted to enhance the different aspects of navigation performance beyond the GPS, like the enhanced receivers and navigation from LEO. One example will be the non-civilian GNSS receiver for quick locking. The non-civilian P(Y) code is encoded at a 10 MHz frequency, while the civilian (C/A) code is encoded at a low frequency. Thus, the non-civilian code is more robust for the jamming. However, the P(Y) code is a pseudo-random code with a long repeat cycle of one week. Thus, without accurate timing information, it typically consumes considerable computing power to acquire the P(Y) code via a cross-correlation computation. Timing accuracy within 1 ms is needed for fast acquisition of the P(Y) code and could save a lot of power. Because of an excellent frequency stability performance, an atomic clock can maintain this 1 ms timing error requirement for several days after synchronization, which is considerably longer than that of the quartz oscillator usually found in GPS receiver [37, 38]. Also with an enhanced receiver, the navigation with less than 4 satellites is feasible, as shown in Fig. 1.4. In a GNSS, at least four satellites are required to provide 4 dimensions (x, y, z, t) for a complete navigation solution when the receiver time is unknown. With a stable time base provided by the ULPAC on the receiver part, the required number of satellites can be reduced to be less than four [39–41]. Besides, the low power and compact atomic clock also enables the integrated inertial navigation and underwater navigation, where the GPS signal is typically too much attenuated to be acquired [37,42,43]. One more important application of ULPAC in the navigation would be the LEO satellite navigation, which could increase GNSS resilience and enhance navigation performance. The three-dimensional (3D) positioning error is determined by the geometry of the satellite constellation, which is quantified by the user range error (σ_{URE}) and position dilution of precision (PDOP). An LEO smallsat constellation like OneWeb could have a σ_{URE} three times worse but give a comparable positioning performance as the GPS.

Geodesy and metrology

In physics, time is a link between velocity and distance. The distance is typically measured by the time of flight (ToF) between the instant when the laser pulse is sent and the instant when the laser pulse is received. An accurate portable clock improves the accuracy of the distance measurement as well as the related parameters such as the velocity. Foreseeing the popularity of auto-vehicles and unmanned-aerial-vehicles, the accurate and quick ranging detection for such systems becomes the key challenge for the maximum speed and safety. The accurate clock technology could improve the accuracy of range detection, thus relax the limit on the safety distance between objects and improve the safety for the passengers as well.

1.2 Atomic Clock Technology and Its Characteristics

1.2.1 Superiority of atomic clock

The frequency stability and accuracy of timekeeping were dramatically improved as the invention of electro-mechanical oscillators such as the quartz crystal and MEMS resonator since the resonating frequencies are less affected by environmental variations [44, 45]. Such kind of small form-factor and stable oscillators have been widely adopted in various

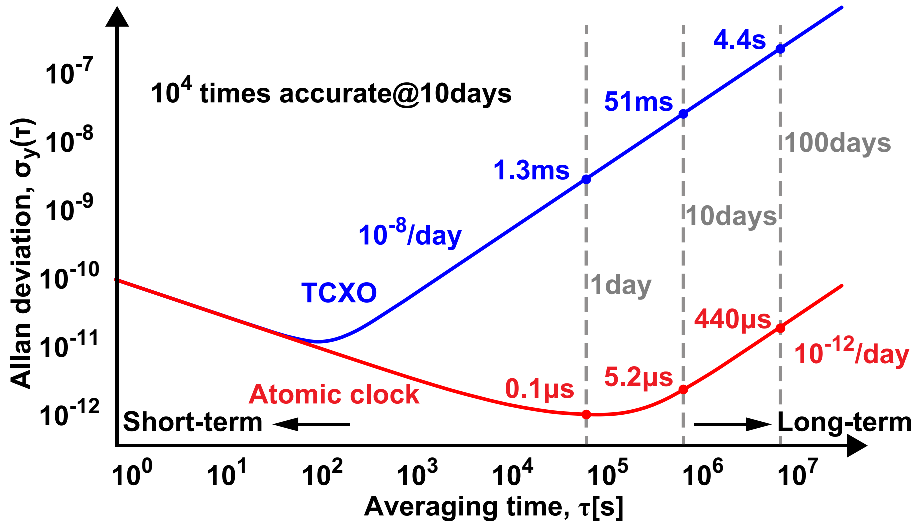

Figure 1.5: Allan deviation and time error of a typical TCXO and a typical compact atomic clock, assuming an initial frequency error of 10^{-8} and 10^{-12}, respectively.

electronics systems or networks such as wristwatches or computers.

However, as the ever-increasing demands of data rates for wireless communication and developments of global scaled networks, the frequency stability requirement on the clock or resonator becomes more and more strict. The typical long-term frequency stability of electro-mechanical oscillators is well below the parts-per-billion level (10^{-9}).

The resonance frequency of the atomic clock is based on the transitions between two energy levels of a particular atom. The frequency of such a transition is given by:

$$\nu_0 = \frac{E_1 - E_2}{h} \tag{1.1}$$

where E_1 and E_2 are the energy of the two levels involved and h is Planck's constant. The energy separation (E_1-E_2) is assumed to be independent of time and space and ν_0 is essentially a constant, characteristic of the two levels 1 and 2 chosen in the energy scheme of a given atom [46, 47].

It seems that the atomic resonance is very attractive and promising for frequency reference. However, many design and implementation difficulties and challenges exist for probing the atomic resonance. One major issue is that the energy levels may be shifted due to various external perturbations. As a result, the resonance frequency is shifted from its nominal value. With the advancement of knowledge about quantum mechanical physics and implementation technology, the atomic clock finally came true in the middle of the last century and the performance of frequency stability keeps improving over the past decades.

The superiority of the atomic clock over the electro-mechanical oscillator based clock is illustrated in Fig. 1.5. One detailed comparison between the atomic clock and the pendulum is listed in terms of temperature sensitivity and reproducibility as follows to validate the superiority of atomic clock [29]:

Pendulum:

i) Temperature sensitivity:

$$f = [g/\ell]^{1/2}/(2\pi) \tag{1.2}$$

$$\delta\ell = \ell\alpha(\delta \mathrm{T}) \tag{1.3}$$

$$\delta f/f_o = -1/2\alpha(\delta \mathrm{T}) \tag{1.4}$$

where ℓ is the length of the pendulum, and α is the coefficient of thermal expansion with a typical value of $10^{-8}/^{\mathrm{o}}C$. Thus, the frequency sensitivity is:

$$\delta f/f_o \cong -5 \times 10^{-9}/^{\mathrm{o}}C \tag{1.5}$$

ii) Reproducibility:

The pendulum length ℓ depends on the manufacture variations.

The gravitational acceleration value changes geographically.

Aging or wear issue is severe.

Atomic clock:

i) Temperature sensitivity (relativistic time dilation):

$$(f_o(\mathrm{T}) - f_o(\mathrm{T}=0))/f_o = -1/2 < (\upsilon/c)^2 > \cong -1.4 \times 10^{-13}\mathrm{T/M(u)} \tag{1.6}$$

where υ is the speed of atom and M is the atomic mass. For ^{133}Cs, M equals to 133 u. Thus, the frequency sensitivity is:

$$\delta f/f_o \cong -1 \times 10^{-15}/^{\mathrm{o}}C \tag{1.7}$$

ii) Reproducibility:

Atoms of a particular kind are identical.

Atoms don't wear out.

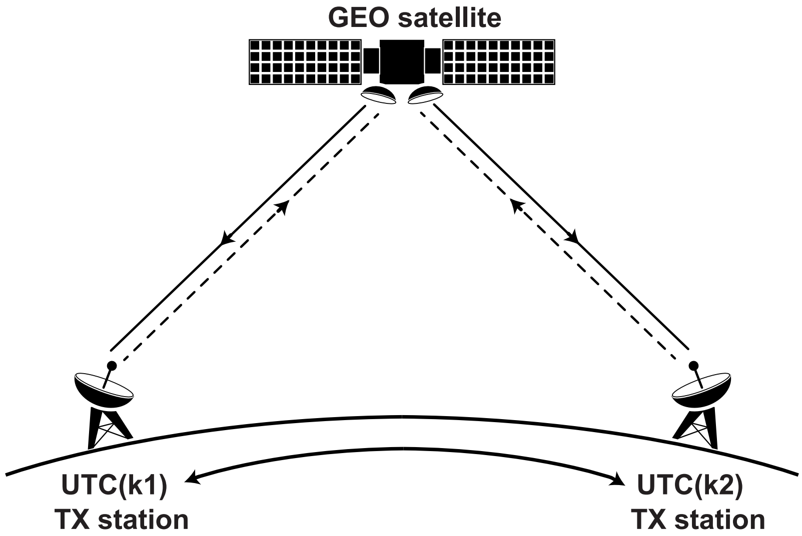

Figure 1.6: Illustration of GPS based time transfer system for coordinated universal time (UTC).

Thus, theoretically, the frequency sensitivity of the atomic clock due to temperature variation is six orders in magnitude better than that of a mechanical clock. Meanwhile, the excellent reproducibility of the atomic clock ensures the accuracy of the time for different clocks built from the same atom as well the aging performance. With the superior frequency stability obtained by the quantum mechanical resonance, the time unit of "second" in the International System of Units (SI) was defined by the unperturbed ground-state hyperfine transition frequency of ^{133}Cs atom. Atomic clock marks a new era for timing transfer and synchronization. The atomic clock has already been the sole choice in applications requiring ultra-high precision clocks, like the GPS. Besides the navigation function, the GPS also has proven itself to be an important and valuable utility for the timekeeping community. In the GPS based timing transfer system, each satellite is equipped with 4 atomic clocks on-board acting like a portable clock above the earth and providing timing information for the receiver with a theoretical accuracy around 14 ns [48, 49]. The GPS also offers a method for clock comparisons that provides the data for the calculation of International Atomic Clock (TAI), as shown in Fig. 1.6. Since 1972, the Coordinated Universal Time (UTC) is calculated by subtracting the accumulated leap seconds from (TAI), which is a coordinate time scale tracking notional proper time on the rotating surface of the Earth (the geoid). As with TAI, UTC is only known with the highest precision in retrospect. Users who require an approximation in real time must obtain it from a time laboratory, which disseminates an approximation using techniques such as GPS or radio time signals. Such approximations are designated UTC(k), where k is an abbreviation for

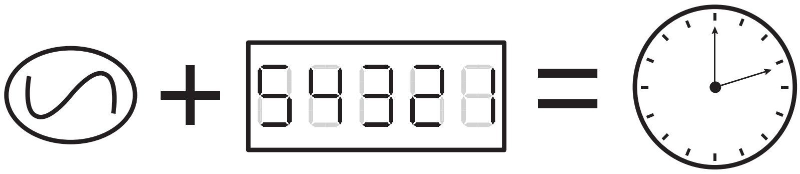

Figure 1.7: Clock made of a resonator and a counter.

the time laboratory [50].

1.2.2 Characterization of atomic clock

All kinds of clocks are made of a resonator and a counter, as shown in Fig. 1.7. The counter simply registers the number of periods of resonances and tells the accumulated passing time from an initial point. The characteristics of the resonator determine the key performance of the clock. As stated above, the reason why the atomic clock is superior to an electro-mechanical oscillator based clock is because the atomic resonance is much less affected by internal or external factors.

However, for a practical implementation, statistical errors and errors from the systematic effect corrections that used to probe frequencies exist [28]. The frequency stability and accuracy are the two key parameters for evaluating the performance of a resonator. They are closely related but indicate different aspects of clock performance. The accuracy indicates how much the resonance frequency deviates from the ideal resonance frequency, while the frequency stability tells how stable the resonance frequency can be kept as time goes by. Figure 1.8 shows one resonance signal in the dash line and one discriminator signal of the resonance signal in the black line. Two types of noise exist in probing the center of the resonance signal. Type I noise affects the detected signal amplitude, which affects short-term frequency stability performance. The type II noise affects the accuracy when locking to the center of the resonance signal. The dc value of type II mainly causes a fixed frequency shift, while other noise contributors may also affect the frequency stability in the long-term. Thus, the observed reference frequency could be written as:

$$\nu_{\text{observed}} = \nu_0 \times (1 + \varepsilon + y(t)) \tag{1.8}$$

where ε represents the fractional frequency offset and $y(t)$ represents the fractional frequency fluctuations. The accuracy is the overall uncertainty on ε and the frequency stability is the statistical properties of $y(t)$. Four types of oscillators could exist with different accuracy and stability performance combinations. The ideal oscillator would be the one demonstrating both stable and accurate resonating frequency. The clock based on such an

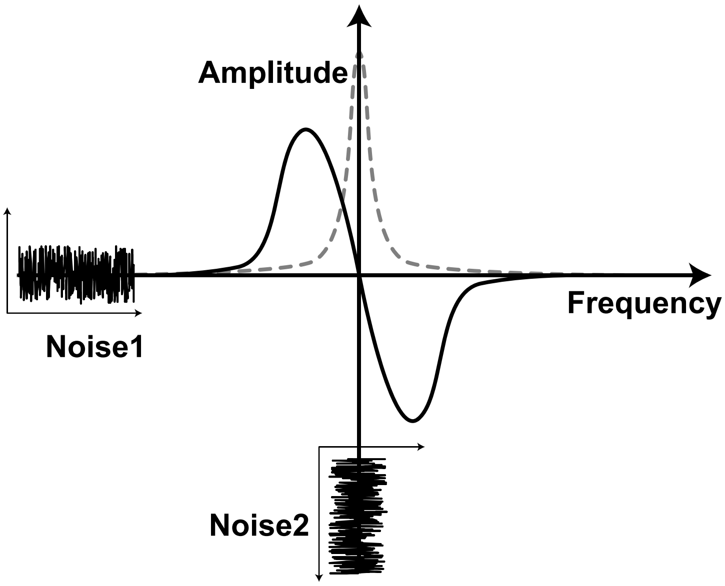

Figure 1.8: Two types of noise affect the different aspects of locking to the resonance frequency.

oscillator is referred to as a master clock. However, this kind type of clock is extremely difficult to obtain and be maintained. In most cases, the frequency stability performance is preferred over the accuracy since the inaccuracy can be mathematical compensated if the resonator demonstrates a stable frequency shift. Thus, for the general purpose applications, frequency stability is the most important performance parameter.

For the frequency stability performance of atomic clock, it is typically divided into short-term, medium-term and long-term stability depending on the averaging time. For the very short-term stability, the qualify factor Q, defined as the ratio of the atomic resonance frequency to the full width at half maximum (FWHM) of the resonance line, is commonly used to indicate the performance. In passive atomic clock, the Q is of great importance, because a narrow line will remove some burden on the electronic system used to detect its center.

For the medium-term and long-term stability, Allan deviation is typically used to evaluate the frequency stability performance because it can converge well for a long averaging time [51, 52]. Allan deviation is a statistical measure of fractional frequency inaccuracy at different averaging times. The Allan variance is defined as:

$$\sigma_y^2(\tau) = \frac{1}{2(M-1)} \sum_{i=1}^{M-1} \left[\langle y(\tau) \rangle_{i+1} - \langle y(\tau) \rangle_i \right]^2 \tag{1.9}$$

where $\langle y(\tau)\rangle_i$ is the i-th measurement of the averaged fractional frequency difference over duration τ and the fractional frequency difference y is defined as:

$$y \equiv (f_c - f_s)/f_0 \tag{1.10}$$

where f_c is the measured clock frequency, f_s represents an ideal clock whose value is close to f_c and f_o is the ideal reference frequency (f_c may be shifted from f_o).

One more efficient method to use the measured data is the "overlapping" Allan variance, which improves the statistical confidence of the calculated result . This and other more sophisticated methods, which can treat various power-law noise types differently, conveniently allow to identify different noise type and estimate the strength of each noise [53, 54]. The identification of different noise types is important for the system-level analysis, the result of which could be used to further improve the performance by mitigating all kinds of noise contributors. Many stationary sources of noise are well behaved for a longer averaging time, which improve the precision of measured frequency and frequency stability. However, other noise contributors, such as long-term frequency shifts, will cause Allan deviation to level off or even increase with increased averaging time.

1.2.3 Survey of atomic clock technologies

Depending on the implementation loop, atomic clocks are divided into active and passive atomic clocks.

A passive atomic clock is the most common type, as shown in Fig. 1.9 (a). In this system, a frequency generated by a crystal oscillator or other frequency source is used to trigger or excite an atomic resonance (discriminator) that produces a correct signal in a feedback frequency control loop to lock and stabilize the oscillator to the atomic reference [54]. The crystal oscillator provides a stable output frequency. Depending on the probing frequency range, the passive atomic clock can be further divided into microwave and optical atomic clock. Also depending on the physical package types, passive atomic clocks are categorized as:

- Rubidium Gas Cell
- Cesium Beam Tube
- Passive Hydrogen Maser
- Trapped Mercury Ion
- Cs or Rb Fountain
- Optical Standard (Several Species)
- Coherent Population Trapping (CPT)

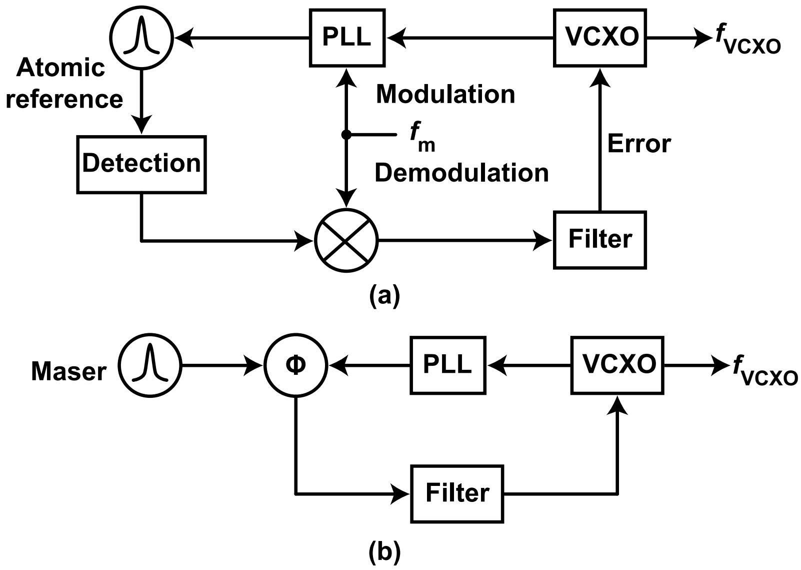

Figure 1.9: (a) Simplified block diagram of a passive atomic clock. (b) Simplified block diagram of an active atomic clock.

The simplified block diagram of the active atomic clock is shown in Fig. 1.9 (b). The active atomic clock is an actual atomic oscillator. Compared with the passive atomic clock, the active atomic clock is based on a phase-locked loop. The active hydrogen maser is the most common implementation, which excels as a frequency source having the best short-term stability.

Passive atomic clocks are preferred as primary (absolute) standards (particularly the beam and fountain devices) because of the ability to evaluate and reduce their bias corrections and accuracy limitations. For example, the Cs fountain clock shown in Fig. 1.10 (a) used as a primary frequency standard demonstrates a significantly high accuracy and frequency stability [2, 55, 56]. The gas-cell based passive atomic clock is also popular as a commercial compact frequency standard, as shown in Fig. 1.10 (b). The typical long-term frequency stability performance of such frequency standards is in the range of 10^{-11} to 10^{-13} [30, 57].

The general procedure for implementing an atomic clock involves four steps: 1) confinement; 2) preparation/state selection; 3) interrogation; 4) detection. The confinements of the atomic beam and laser cooling typically result in a bulky implementation. Also, the cavity limits the quantum physical package dimension beyond the wavelength of the microwave radiation. The microwave cavity interrogation demands relatively large power consumption. The CPT method indicates an all-optical implementation, which is important for a small form-factor implementation and low cost. The performance of atomic clock has not changed for several decades. Active hydrogen maser is used in small num-

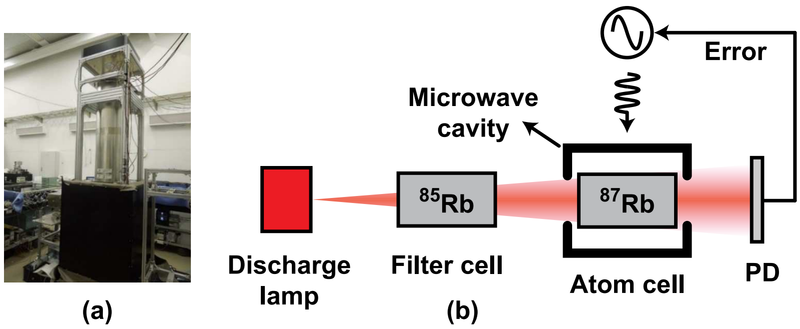

Figure 1.10: (a) Cs fountain clock NMIJ F2 [2]. (b) Commercial compact Rb frequency standard.

bers for their superior stability. Among the passive atomic frequency technologies, the Cs beam and Rb gas cell are the most common. In recent years, Rb frequency standards have found widespread use in commercial telecom applications.

1.3 Transportable Atomic Clock Technology

The technology development directions of atomic clocks can be divided into two general categories: 1). Relative accuracy; 2). Compact and low power. The main purposes behind the different development directions are the different application requirements. The extremely low relative accuracy atomic clock aims to serve as a master clock for global timing transfer systems like the UTC. While the compact and low power atomic clock aims for various portable and mobile applications, where the frequency stability requirement can only be met by the atomic clock. Figure .1.11 shows the development history of high accuracy atomic clock. The atomic clock uses a hyperfine transition frequency in the microwave range and optical atomic clocks are the two major high-performance clock for accuracy. In 2013, the optical atomic clock demonstrates the frequency stability in the region of 10^{-18} [58, 59] in a lab environment, which is the most accurate measured atomic clock performance. But the applications of such atomic clock technologies are limited due to the large power consumption and bulky implementation. For example, the fountain clock NIST-F1 consumes 500 W and occupies a volume of approximately 3 m^3. Even the compact Rb frequency standard consumes around several to tens of watts with a volume ranging from 155 to 755 cm^3. For mobile or portable applications, the power consumption should be below 100 mW and the volume should be below 20 cm^3 for SoC integration. The quartz crystal oscillators easily meet these requirements. But their frequency stability performance is far from the timing synchronization requirement of high performance and large scale networks, such as LEO smallsat constellation.

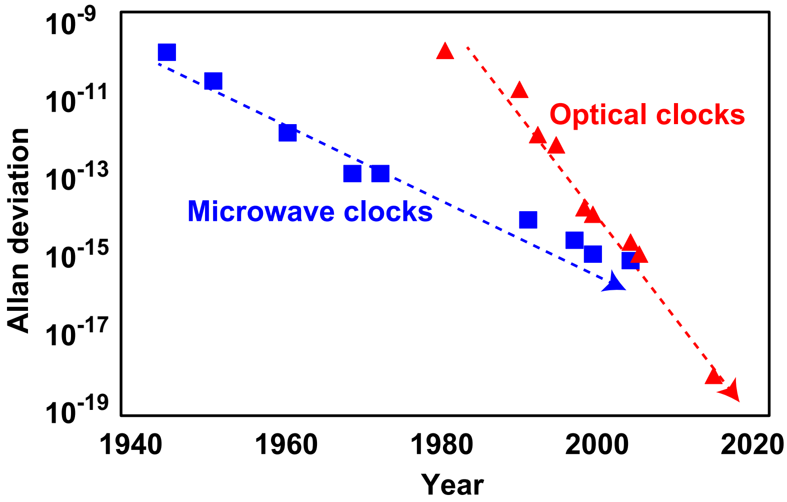

Figure 1.11: Accuracy of the high-performance atomic clocks.

The concept of chip-scale atomic clock (CSAC) was first proposed by the NIST at the beginning of this century, whose design goals include short-term stability, σ_y (τ=1 hour), of 1×10^{-11} with a total power consumption of 30 mW and an overall device volume of 1 cm^3 [60]. With almost two decades of development progress, the pioneering and notable work from NIST and Microsemi has already demonstrated the feasibility of this concept. The realized CSAC consumes 120 mW with a volume of 16 cm^3. Another interesting work based on chip-scale molecular clock [61] done by MIT features low power consumption, low cost, high reliability, and system simplicity because of the absence of lasers. However, due to insufficient systematic study of buffer gas, the quality factor of the molecular clock is degraded, which is entirely limited by the Doppler broadening at present. Besides, the high probing frequency, which is set to be approximately several hundred gigahertz, presents numerous design challenges, especially for complementary metal-oxide-semiconductor (CMOS) implementation [62]. The difficulty of probing terahertz frequency is solved by adopting an optical comb in the optical atomic, which offers a promising solution for high-frequency stability chip-scale atomic clock if a microfabricated optical comb is available [63].

The present work continues the CPT approach as already adopted in the CSAC and demonstrates recent advancements in reaching ultralow-power operation and excellent long-term frequency stability by featuring an efficient vertical-cavity surface-emitting laser (VCSEL), a robust quantum physical package, and low noise probing and locking circuits [64]. The present work achieves an optimum balance between the power consumption and frequency stability among chip-scale atomic/molecular clocks [8, 60, 61, 65–69]. The performance comparison of this work with other types of compact or chip-

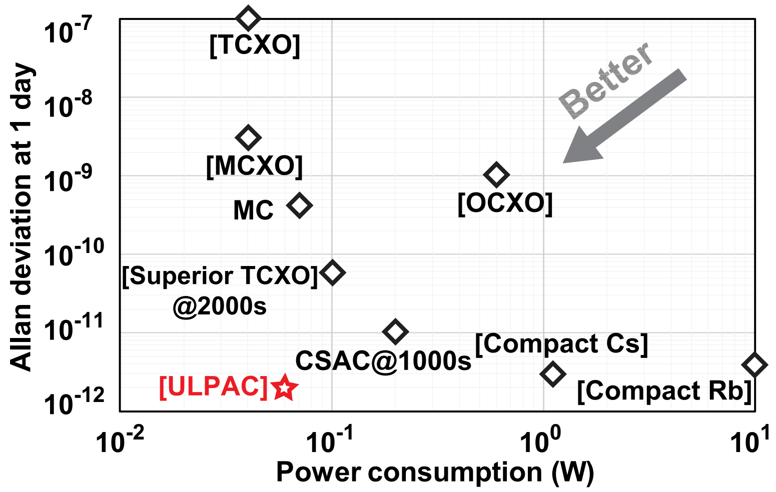

Figure 1.12: Allan deviation and power consumption performance for compact atomic clocks and various crystal oscillators.

scale clocks is shown in Fig. 1.12.

1.4 Thesis Organization

As shown in Fig. 1.12, this thesis focuses on achieving ultralow-power and excellent long-term frequency stability performance of the atomic clock. To achieve the low power consumption operation, a full CMOS frequency probing and locking loop is implemented with power-efficient circuit design techniques. Meanwhile, the short-term frequency stability is maintained by low noise circuit design techniques and loop bandwidth optimization. In addition, a dedicated stable magnetic field, optimization of the operation condition of the VCSEL and temperature control loop are incorporated for isolating and mitigating the internal and external factors affecting the long-term frequency stability. This thesis introduces the implementation details of frequency probing and locking loop together with other control loops. Besides, system-level modeling and analysis are provided for performance optimization and evaluating the atomic clock performance.

Chapter 2 of this thesis starts with an introduction to the physical principle of ULPAC. It explains the concept of CPT. The superiority of the CPT approach for realizing a compact atomic clock is illustrated with a comparison of electromagnetically induced transparency (EIT) method. Chapter 3 gives the implementation details of ULPAC regarding the quantum physical package, frequency probing and locking loop as well as other control loops like the magnetic, temperature loops. Chapter 4 includes the evaluations and characterizations of the ULPAC performance. One thorough performance analysis is carried out for diagnosing the short-term noise contributor and major frequency shift. Chapter 5 focuses on the low power circuit design techniques for next-generation 20 mW ULPAC. One novel power-efficient CMOS oscillator with low phase noise performance and one ultralow-power injection-locked phase-locked loop (PLL) are introduced. Chapter 6 introduces promising potential quantum technologies that can be adopted in the future to improve frequency stability performance. Conclusions are also included in this final chapter.

Chapter 2

CPT Interrogated Atomic Clock Operating Principle

Conventional atomic clocks demonstrate superior frequency stability and accuracy over electro-mechanical oscillator based clock. But due to the complicated confinement and interrogation methods, huge power consumption and bulky design are needed, which severely limit the applications of such atomic clocks for the mobile or portable applications.

The most common commercial compact frequency standard is based on the Rb gas cell, as shown in Fig. 2.1 (a). It adopts the double-resonance method and EIT, in which the Rb gas cell is placed inside a microwave cavity [70, 71]. In order to make the microwave field modes resonate, the cavity dimension must be equal to the wavelength of the microwave radiation, which is around several centimeters for Rb. Further miniaturization of these conventional designs appear challenging. Besides a discharge lamp is required for the optical pumping, whose power consumption is typically larger than 1 W. So far, the applications of such frequency standards are still quite limited.

As mentioned in Chapter 1, the CPT method allows an all-optical implementation with a vapor atom cell, which enables a small form-factor design. The architecture of CPT based atomic clock is shown in Fig. 2.1 (b). As compared with the double-resonance method, this architecture adopts a low power VCSEL instead of a discharge lamp. The microwave cavity is not required for the implementation. Probing the atomic reference with the light eliminates the need for a bulky microwave cavity and allows a dramatic size reduction of quantum physical package over the clocks based on EIT. This chapter introduces the CPT interrogation method and the atomic clock architecture based on this principle.

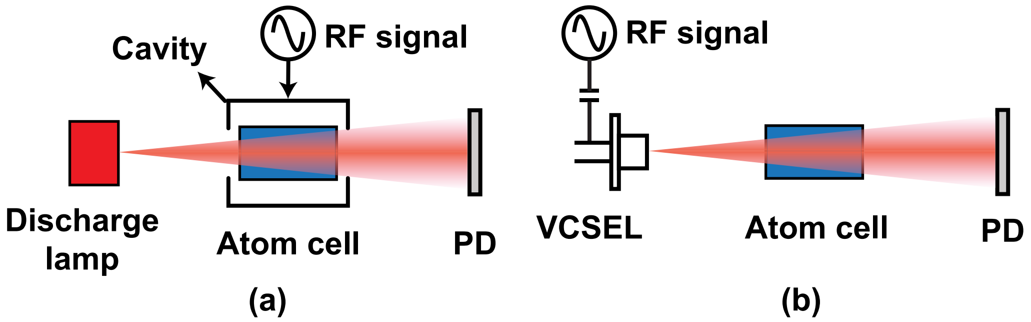

Figure 2.1: (a) Commercial compact Rb frequency standard. (b) ULPAC based on coherent population trapping (CPT) principle.

2.1 Selection of Atoms and Optical Line

The selection of atoms and optical line determines the probing and locking frequency, the signal contrast η_{CPT} (defined as the signal level of the CPT resonance over the back-ground dc level), the laser wavelength, the circuit design complexity and power consumption, et al. Some performance trade-offs also exist, which require system-level optimization and understanding.

2.1.1 Atom selection

Hydrogen, certain ions, and alkali atoms are typically adopted for implementing the atomic clocks since they share many similar physical properties like the symmetry of the unpaired-electron wave-function. The hydrogen atom has been used for building the most stable atomic clock, hydrogen maser. And certain ions like Hg^+ and Ba^+ are typically used for a single trapped ion atomic clock with laser cooling method. For a small gas-vapor cell-based atomic clock, the alkali atoms are typically selected because of their comparatively simple energy structures [9]. And the probing frequencies of alkali atoms happen to be approximately several gigahertz, which is design-friendly for low-power CMOS circuits. Rb atoms are commonly used in most commercial frequency standards for mature laser technologies with the Rb optical pumping wavelength. The ^{133}Cs atom is adopted in this work partly because it is also used to define the time unit of "second" in the SI.

2.1.2 Fine structure and optical line selection

The spin-orbit interactive causes one particular energy levels of alkali atoms to split into two sub-levels, noted as $6^2P_{3/2}$ and $6^2P_{1/2}$ for Cs atom, as shown in Fig. 2.2. Therefore,

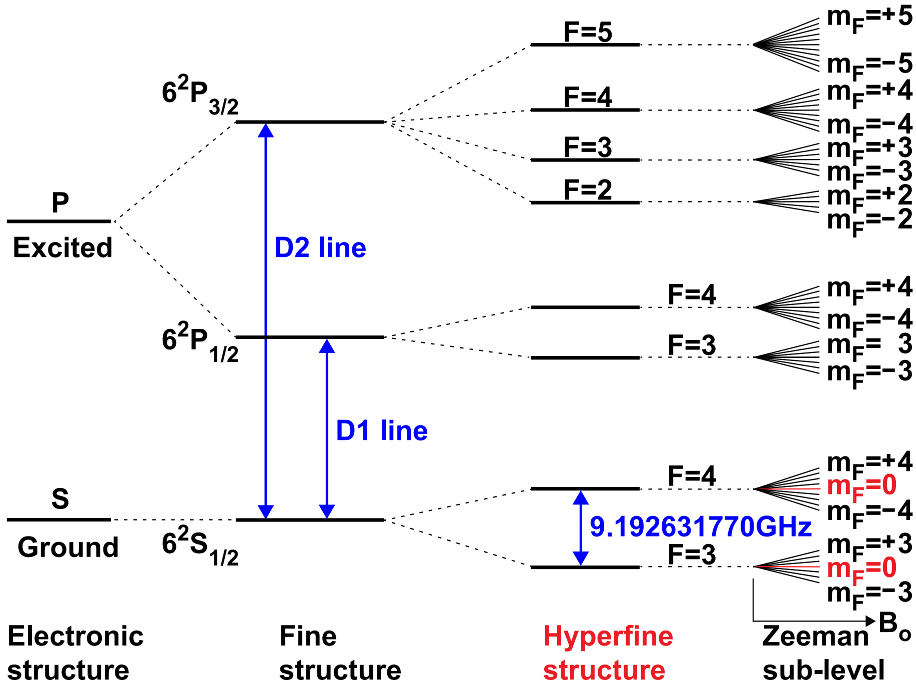

Figure 2.2: Energy levels of the valence electron in a Cs atom.

two possible optically excited states can be used in the alkali atoms, corresponding to lines D1 and D2 [72–75]. The difference arises from the sub-level numbers in these two excited states in the hyperfine structure. Experiments show that the contrast η_{CPT} using line D1 is much stronger than that using line D2, which could result in a better frequency stability performance [60]. In the case of Cs atom, the $6^2P_{1/2}$ has only 2 sub-levels, while $6^2P_{3/2}$ has 4 sub-levels. The laser light in a vapor atom cell is typically Doppler broadened to several hundred megahertz. The F=4 and F=3 levels in both the $6^2P_{1/2}$ and $6^2P_{3/2}$ are not well resolved in such case. Both F=4 and F=3 levels contribute to the CPT signal. However, the F=2 and F=5 levels in the $6^2P_{3/2}$ provide additional loss channels for the ground-state coherence, which contributes to the width of the CPT signal and also introduces background absorption. However, it is quite challenging and difficult to acquire a robust and high-performance VCSEL with a wavelength of 894.6 nm for ^{133}Cs line D1 absorption [76]. Following the VCSEL development history of CSAC for Cs line D1 absorption [77], a custom-designed low power VCSEL is presented as well in this work.

2.2 Hyperfine Structure and Coherent Population Trapping

The proton and the electron possess a magnetic moment and interact through magnetic forces. This creates, in the energy levels, a splitting that we call hyperfine splitting. For the alkali atoms like the Cs, the ground energy level is further splitting into two sub-ground levels (state $|1\rangle$ and state $|2\rangle$) for the hyperfine structure as shown in Fig. 2.2 [78]. The frequency difference between these two sub-ground states is called hyperfine frequency Δ_{hf}, whose value is exactly equal to 9.192631770 GHz, corresponding to the definition of the one second.

The CPT phenomenon is first qualitatively explained here together with the double-resonance phenomenon. As shown in Fig. 2.3 (a), the atom ensemble is illuminated by an optical source, resonant with the transition between one of the hyperfine ground states (state $|2\rangle$ here) and an excited state. The electron jumps either from state $|1\rangle$ or state $|2\rangle$ to state $|3\rangle$. The transmitted light intensity is detected by a photodetector (PD). The electron in the excited state can decay into either state $|1\rangle$ or state $|2\rangle$. Eventually, a large fraction of atoms will accumulate in the state $|1\rangle$ due to optical pumping [79]. When the RF signal is absent, the ground state $|2\rangle$ will thus be depleted limiting the absorption. When the RF radiation is applied, resonant with the ground state hyperfine splitting, the atoms can be repumped from state $|1\rangle$ to state $|2\rangle$. The impact of the RF on the optical transmission, as a function of RF detuning, is indicated in Fig. 2.3 (a) as well.

The CPT interrogation technique is illustrated in Fig. 2.3 (b). In this approach, a pair of collinear, circularly-polarized laser lights are simultaneously applied to the atom ensemble. If these two lights are tuned so as that each couples one of the ground hyperfine states to the same excited state, a coherence is generated in the atom ensemble. It is assumed as one destructive quantum interference, which largely reduces the jumping probabilities from both ground states to the excited state for the atom, so it appears dark [80–83].

The simple three-level model shown in Fig. 2.4 lends an easy quantitative analysis of the CPT [4]. Two light fields E_1 and E_2 with frequencies ω_1 and ω_2 and phase ϕ_1 and ϕ_2 can couple the electric dipole transitions $|1\rangle \leftrightarrow |3\rangle$ and $|2\rangle \leftrightarrow |3\rangle$. In the thermal equilibrium state, it is assumed that both ground states have equal populations. If the frequency difference between the two light fields $\omega_1 - \omega_2$ is equal to the hyperfine frequency Δ_{hf}, then the atoms will be pumped into a coherent state $|\mathrm{NC}\rangle$, which is referred to as "dark state". Instead of using the energy eigenstates $|1\rangle$ and $|2\rangle$, a new basis pair of linear combinations

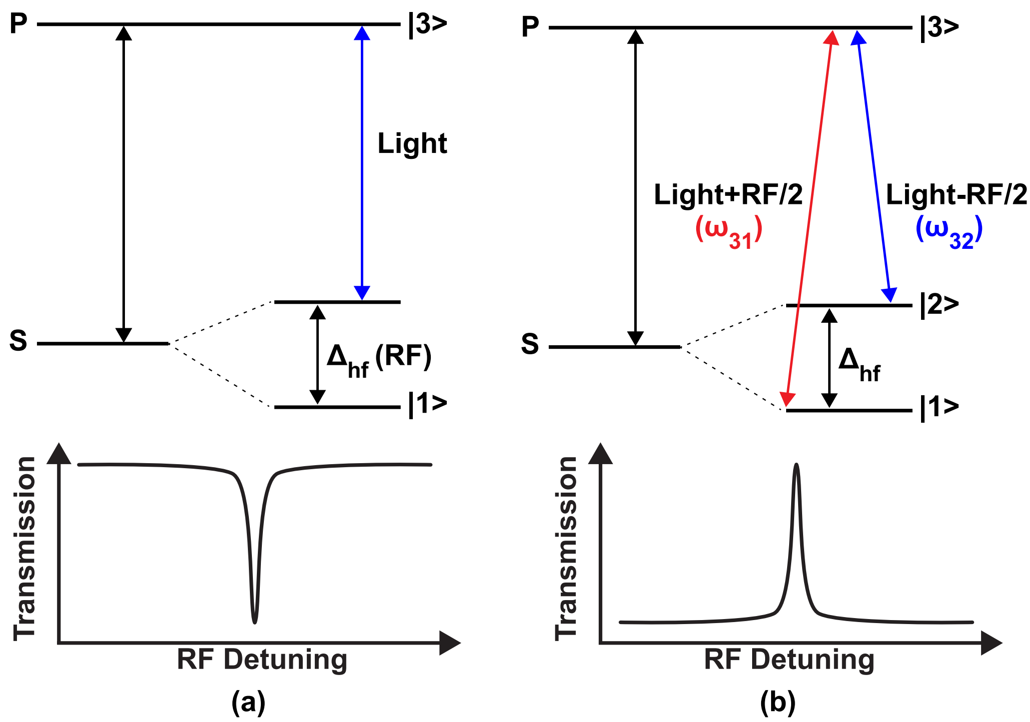

Figure 2.3: Relevant energy levels and resonance line shapes for (a) a double-resonance interrogation and (b) CPT interrogation [3].

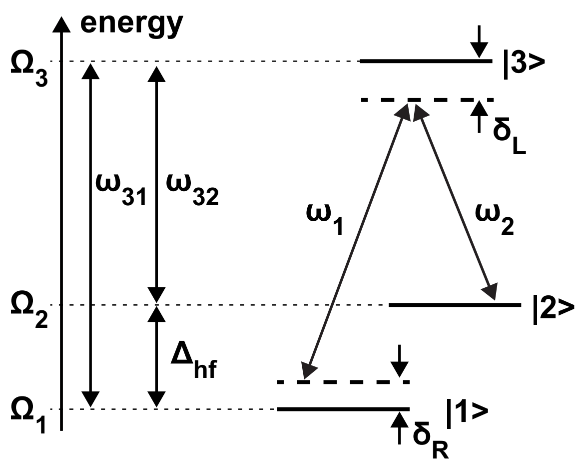

Figure 2.4: Three-level Λ model for quantitative analysis [4].

of $|1\rangle$ and $|2\rangle$, $|C\rangle$ and $|NC\rangle$ are introduced:

$$|C\rangle = \frac{1}{g_\Lambda}(g_1^*|1\rangle + g_2^*|2\rangle) \tag{2.1}$$

$$|\mathrm{NC}\rangle = \frac{1}{g_\Lambda}(g_1|1\rangle - g_2|2\rangle) \tag{2.2}$$

where the Rabi frequencies g_i is defined by the transition dipole moment:

$$g_1 = -d_{31}E_1/\hbar \tag{2.3}$$

$$g_2 = -d_{32}E_2/\hbar \tag{2.4}$$

$$g_\Lambda = \sqrt{|g_1|^2 + |g_2|^2} \tag{2.5}$$

$$d_{3i} = -e\langle 3|r|i\rangle, i = 1, 2. \tag{2.6}$$

for $\Delta_{\mathrm{hf}} \neq 0$ the new states are nonenergy eigenstates but develop in time:

$$|\mathrm{C}\rangle\,(t) = \frac{1}{g_\Lambda}\mathrm{e}^{-\mathrm{i}\Omega_1\mathrm{t}}(g_1^*\,|1\rangle + \mathrm{e}^{-\mathrm{i}\Delta_{\mathrm{hf}}\mathrm{t}}g_2^*\,|2\rangle) \tag{2.7}$$

$$|\mathrm{NC}\rangle\,(t) = \frac{1}{g_\Lambda}\mathrm{e}^{-\mathrm{i}\Omega_1\mathrm{t}}(g_1\,|1\rangle - \mathrm{e}^{-\mathrm{i}\Delta_{\mathrm{hf}}\mathrm{t}}g_2\,|2\rangle) \tag{2.8}$$

In the rotating wave approximation, the electric dipole operator coupling ground and excited states is:

$$\begin{aligned} V_{\mathrm{dip}} =& \frac{\hbar g_1}{2}\exp(-\mathrm{i}w_1 t - \mathrm{i}\phi_1)\,|3\rangle\,\langle 1| + \mathrm{c.c} \\ &+ \frac{\hbar g_2}{2}\exp(-\mathrm{i}w_2 t - \mathrm{i}\phi_2)\,|3\rangle\,\langle 2| + \mathrm{c.c} \end{aligned} \tag{2.9}$$

So that with $\Delta\phi = \phi_1 - \phi_2$, the transition dipole matrix elements into the excited state are:

$$\begin{aligned} \langle 3|V_{\mathrm{dip}}|\mathrm{C}\rangle =& \frac{\hbar}{2g_\Lambda}\exp[-\mathrm{i}(\Omega_i + \omega_1)t - \mathrm{i}\phi_1] \\ &\times (|g_1|^2 + |g_2|^2\exp[\mathrm{i}\delta_{\mathrm{R}}t + \mathrm{i}\Delta\phi]) \end{aligned} \tag{2.10}$$

$$\begin{aligned} \langle 3|V_{\mathrm{dip}}|\mathrm{NC}\rangle =& \frac{\hbar g_1 g_2}{2g_\Lambda}\exp[-\mathrm{i}(\Omega_i + \omega_1)t - \mathrm{i}\phi_1] \\ &\times (1 - \exp(\mathrm{i}\delta_{\mathrm{R}}t + \mathrm{i}\Delta\phi)) \end{aligned} \tag{2.11}$$

When the frequency difference of the two light fields equls to the ground state splitting and $\delta_{\mathrm{R}} = 0$ condistion is met at proper relative phase ($\Delta\phi = 0$), only one transition is possible:

$$\langle 3|V_{\mathrm{dip}}|\mathrm{C}\rangle = \frac{\hbar}{2g_\Lambda}\exp[-\mathrm{i}(\Omega_i + \omega_1)t - \mathrm{i}\phi_1] \tag{2.12}$$

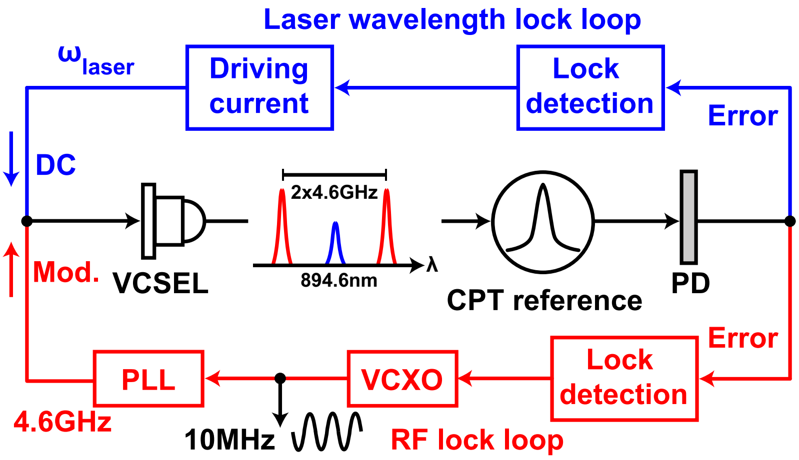

Figure 2.5: Simplified system diagram of ULPAC based on CPT principle.

$$\langle 3|V_{\text{dip}}|\text{NC}\rangle = 0 \tag{2.13}$$

where $|\text{NC}\rangle$ is called the coherent dark state. Thus, the population that is optically pumped out of state $|\text{C}\rangle$ becomes trapped in $|\text{NC}\rangle$.

The three-level model provides an effective easy understanding and explanation for the CPT phenomenon. However, some non-ideal effects are missing from this model, like the Zeeman effect as will be explained in Section 2.4.2 and reduced signal contrast. The Zeeman effect introduces additional incoherent trapping states, which make the Λ scheme not closed anymore. Consequently, it is necessary to use a four-level system including a trap for the theoretical analysis [84].

2.3 Miniaturized Ultra-low-power Atomic Clock

The architecture for ULPAC using CPT interrogation method is disclosed in this section. The ULPAC is based on the Cs atom D1 absorption line. The simplified ULPAC architecture is shown in Fig. 2.5. It mainly consists of three parts: i) a quantum physical setup for the CPT atomic resonance; ii) a laser wavelength locking loop; iii) an RF modulation frequency locking loop. The quantum physical setup is the main setup for the CPT resonance, which mainly includes one VCSEL as a light source, one vapor cell containing Cs atom ensemble, and one PD to detect the light absorption and converts the signal from light domain to current domain. The RF-signal modulated VCSEL is used to produce the bichromatic light for the atom cell containing the Cs atoms. The interference light triggers the CPT resonance in the vapor cell, which provides an atomic frequency reference signal. The resonance signal detected by a PD is then used for correcting and stabilizing the voltage-controlled crystal oscillator (VCXO) frequency. One current-source bank is used to lock the wavelength of the VCSEL to 894.6 nm for Cs D1 line absorption, and one PLL is used to lock the frequency of the modulation RF signal to half of the hyperfine frequency by applying a multiplication operation to the crystal oscillator frequency. When the dip of the CPT resonance signal is detected and locked by these feedback loops, the 10-MHz output from the VCXO inherits the frequency stability of the CPT resonance of the ^{133}Cs atom.

2.4 Frequency Stability Analysis

The quantum mechanical resonance is known to be independent of its position in the universe and will remain the same as long as the particle itself exists except for the relativistic effects [46, 47]. However, noise arising from the frequency probing and locking loop could affect the frequency stability of the system. In addition, the natural resonance frequency of the atoms can be shifted from the unperturbed values by many environmental effects. The former noise contributors mainly affect the short-term frequency stability, while the latter frequency shift contributors impact the frequency stability in the long averaging time. For the systematic frequency shift contributors, it is common to divide them into those resulting from environmental variations and those which referred to as observational shifts [28].

2.4.1 Short-term frequency stability analysis

The definitions of short term, medium term, long term are not well clarified in previous papers. The analysis of stability in this section mainly applies to the case, in which the averaging time τ is less than 100 s for the short-term stability.

The linear model of the frequency servo loop of ULPAC is shown in Fig. 1.9 (a). Because the spectral densities of most stationary noise sources drop with increasing Fourier frequencies, a modulation-demodulation method technique is adopted in this work instead of a pure dc detection for the CPT resonance signal [4]. A small frequency f_{m} is used to modulate the frequency control word (FCW) of the PLL. Then, the modulated RF signal f_{RF} is used to excite the CPT resonance. A discriminator signal detected by a lock-in amplifier is then demodulated with the same frequency f_{m} and used to correct and stabilize the VCXO frequency by always locking to the dip of the CPT resonance signal.

Note that there are two major noise contributors for this system: i) the CPT resonance detection noise, which affects the spectrum of the detected f_{CPT} signal, and ii) the noise of the VCXO, which affects the output frequency spectrum directly. Following the linear

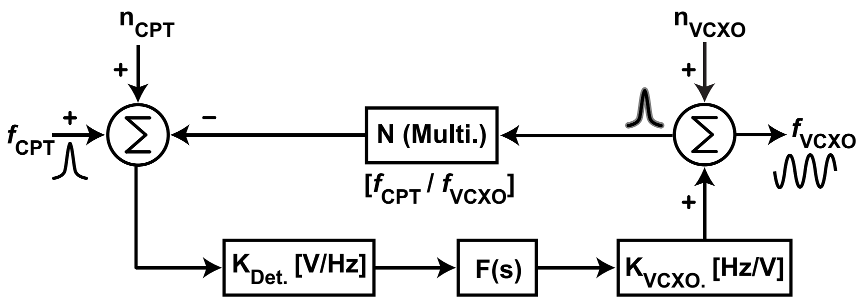

Figure 2.6: Frequency domain noise model for short-term frequency stability analysis.

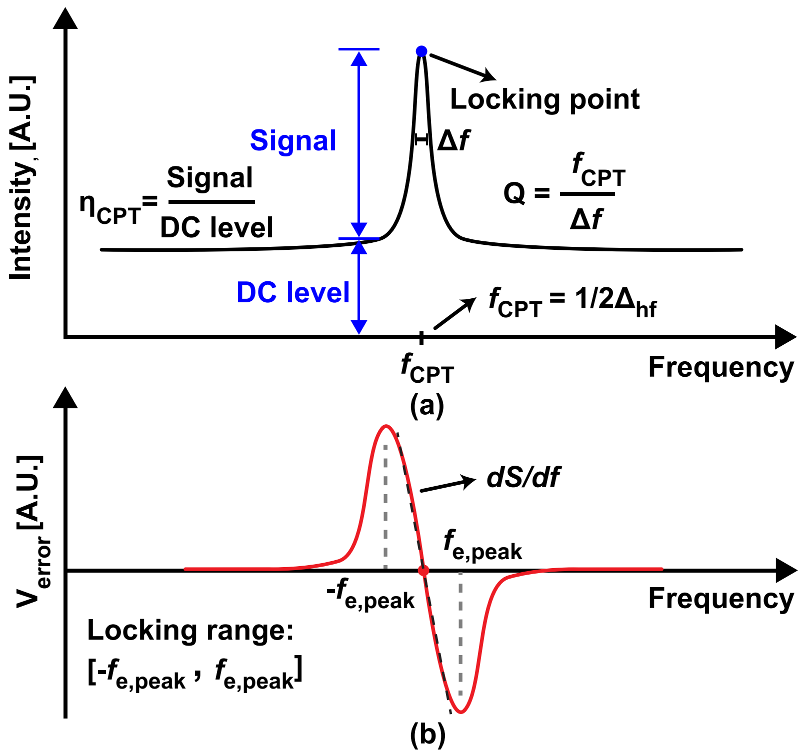

Figure 2.7: (a) Lorentzian profile of CPT resonance. (b) Discriminator signal of CPT resonance signal.

model of the frequency servo loop, the frequency noise model is shown in Fig. 2.6 [85]. The noise in the detection loop is referred to as the n_{CPT}. The $\mathrm{K}_{\mathrm{Det.}}$ represents the frequency discriminator sensitivity of the CPT resonance signal coupled to the photo-detector. $\mathrm{K}_{\mathrm{VCXO}}$ represents the VCXO frequency coefficient. The transfer function of the loop filter is F(s), and N(Multi.) is the frequency multiplication ratio of the PLL.

Previous frequency-stability studies on the microwave resonance signal of passive atomic clock can be applied to the case of CPT resonance signal with a minor modification because these implementations share a similar signal excitation and detection principle [86, 87]. Fig. 2.7 (a) shows a Lorentzian profile of the CPT resonance signal. Note that the center frequency of the CPT resonance (f_{CPT}) in the present study equals $1/2\Delta_{\mathrm{hf}}$ because the VCSEL is RF signal modulated and the two first sidebands of the VCSEL outputs are used as the interference light for the CPT resonance. In order to lock to the peak of the CPT resonance signal, a small frequency-modulated (FM) RF signal is adopted, as mentioned previously, and a sensitive discriminator signal dS/df is extracted by a lock-in amplifier, as shown in Fig. 2.7 (b). Assuming a signal fluctuation δS caused by the noise in the detection loop, the corresponding frequency shift δf that is detected is given by:

$$\delta f = \frac{\delta S}{dS/df} \tag{2.14}$$

The fractional frequency errors δy_{e} during one measurement period is given by (assuming the averaging frequency during the measurement time is equal to the nominal resonance frequency, f_{CPT}) [28]:

$$\delta y_{\mathrm{e}} = \left(\frac{\delta f}{f_{\mathrm{CPT}}}\right)_{\mathrm{e}} = \frac{\delta S}{f_{\mathrm{CPT}}(dS/df)} \tag{2.15}$$

In order to minimize the δy_{e}, the discriminator sensitivity dS/df should be maximized, while the δS itself should be minimized. Equation (2.15) can be rewritten as:

$$\delta y_{\mathrm{e}} = \frac{1}{(S/N)Q} k_S \tag{2.16}$$

where $(S/N) = (S/\delta S)$ is the signal-to-noise ratio, $Q \equiv f_{\mathrm{CPT}}/\Delta f$ is the quality factor of the resonance signal (Δf is the FWHM of the CPT resonance signal), and $k_S \equiv (dS/df)\Delta f/S$ is a parameter related to the line shape of the CPT resonance signal.

The CPT resonance is mostly affected by the shot noise from the PD, the intensity and frequency fluctuations of the VCSEL. The latter includes the phase noise of the RF signal used to modulate the VCSEL, current noise of the dc biasing circuit and the amplitude-modulated (AM) and phase-modulated (PM) noise of VCSEL.

Shot noise is a quantum noise effect, related to the discreteness of photons and electrons. The short-term frequency stability due to the shot noise can be given approximately by [87–89]:

$$\sigma(\tau) = \frac{\chi}{4f_{\mathrm{CPT}}} \sqrt{\frac{e}{I_{\mathrm{bg}}}} \frac{1}{Q} \tau^{-1/2} \tag{2.17}$$

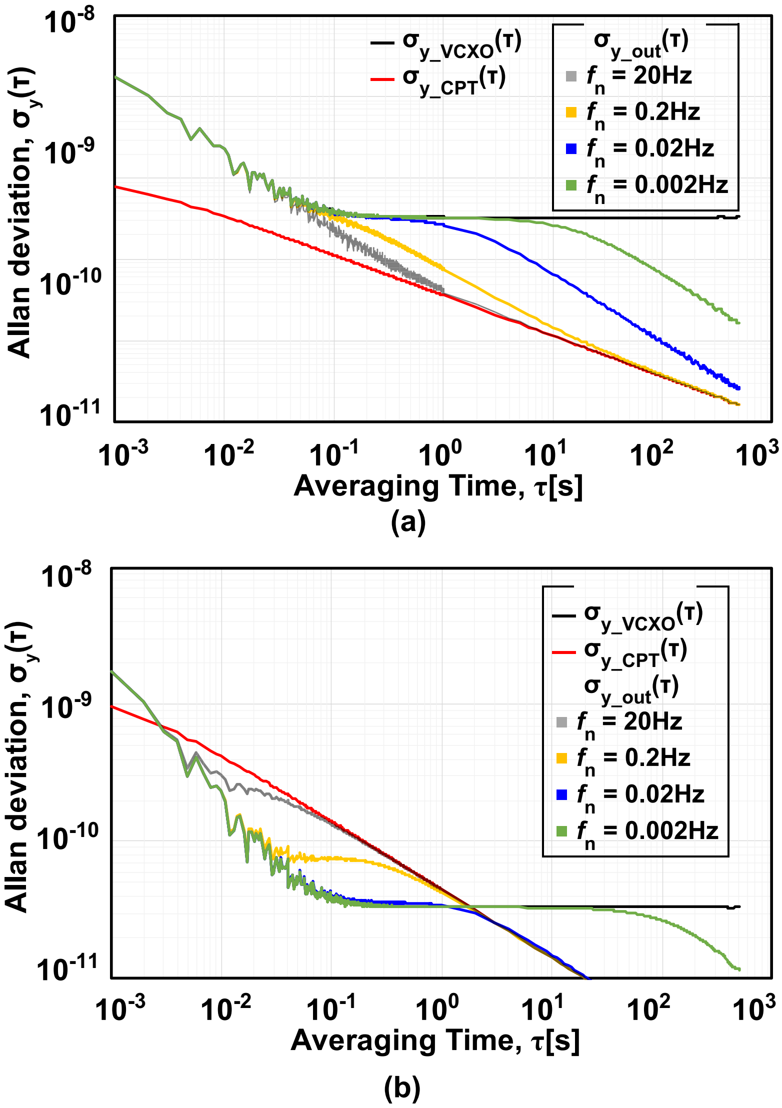

Figure 2.8: Calculated σ_{y_out} for case (a) an excellent σ_{y_CPT} in conventional highly accurate and stable atomic clock and case (b) a degraded σ_{y_CPT} in a compact or chip-scale atomic clock.

where χ is a parameter related to the shape of the CPT resonance signal, e is the electron charge, I_{bg} is the background current of PD.

If only white frequency noise is assumed, the frequency stability of the detected CPT signal σ_{y_CPT} is given as follows [28, 90]:

$$\sigma_{y\_CPT} = \frac{\chi}{QS/N} \frac{1}{\sqrt{\tau}} \tag{2.18}$$

Thus, for the short-term frequency stability of the detected CPT signal, the S/N ratio and Q factor are the two major factors. More specifically, the phase noise at the harmonics of the modulation frequency $f_{\rm m}$, the noise of lock-in amplifier, the shot noise of the PD, and the fluctuation of the laser output power affect the S/N of the detected CPT resonance signal, among which the latter two are the dominant contributors.

The detected CPT stability $\sigma_{\rm y\_CPT}$ is transferred to the stability of the crystal oscillator through the frequency servo loop. The equations describing the servo loop for the frequency fluctuations can be derived from the frequency domain model shown in Fig. 2.6 (b) [85, 91, 92]:

$$S_{\rm y\_out}(f) = \frac{(f/f_n)^2}{1+(f/f_n)^2} S_{\rm y\_VCXO}(f) + \frac{1}{1+(f/f_n)^2} S_{\rm y\_CPT}(f) \tag{2.19}$$

where $S_{\rm y\_out}$, $S_{\rm y\_VCXO}$ and $S_{\rm y\_CPT}$ are power spectral density of fractional frequency fluctuations of output port, VCXO and physical package, respectively. The open-loop unity-gain bandwidth f_n is defined as:

$$f_n = \frac{NK_{\rm Det.}K_{\rm VCXO}}{2\pi RC} \tag{2.20}$$

where a first-order low-pass loop filter is assumed with a transfer function of $F(s) = (1/RCs)$. Then, the two-sample time-domain stability $\sigma_{\rm y\_out}$ can be calculated by [93]:

$$\sigma^2_{\rm y\_out} = 2\int_0^\infty S_{\rm y\_out}(f) \frac{\sin^4 \pi f \tau}{(\pi f \tau)^2} \left| \frac{1}{(1+f/f_c)^2} \right| df \tag{2.21}$$

where $f_{\rm c}$ is the cutoff frequency of the one-pole filter assumed to be present at the input of the time-domain measurement system. Figure 2.8 shows the calculated $\sigma_{\rm y\_out}$ results for two cases. In Fig. 2.8 (a), the $\sigma_{\rm y\_CPT}$ is always better than $\sigma_{\rm y\_VCXO}$. Under such a situation, the loop bandwidth $f_{\rm n}$ should be designed large enough to suppress the noise contributor from the VCXO. In Fig. 2.8 (b), the $\sigma_{\rm y\_CPT}$ is worse than $\sigma_{\rm y\_VCXO}$ for some ranges. In this situation, an optimal loop bandwidth $f_{\rm n}$ exists, which should be large enough to suppress the noise contributor from VCXO for the long averaging time and small enough to suppress the noise contributor from CPT for the very short averaging time. The former case is a typical case for conventional highly accurate and stable atomic clock and the latter is the common case for the compact or chip-scale atomic clock, especially when high-performance VCXO is adopted. Thus, it is important to optimize the loop bandwidth for the compact atomic clock for better overall frequency stability performance.

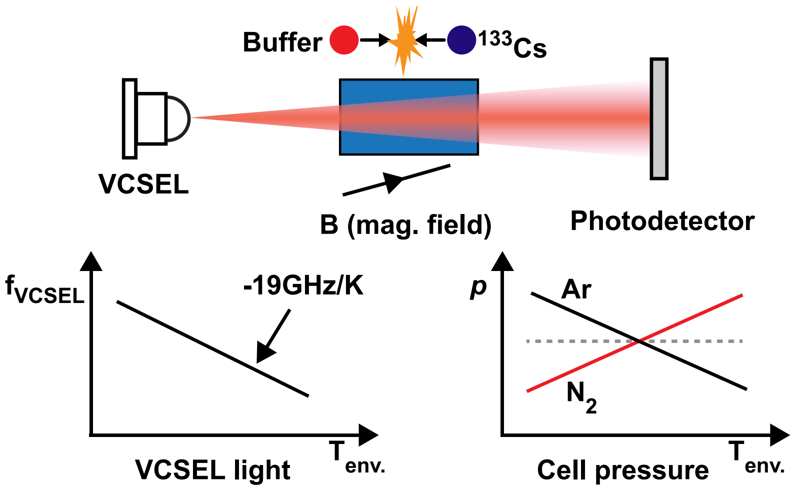

Figure 2.9: Frequency shift contributors for ULPAC.

2.4.2 Frequency shift contributors

Based on the stability analysis in the previous section, the stability of the atomic clock will follow the intrinsic stability of the CPT resonance signal as $\tau^{-1/2}$ when the averaging time is increased, which is not realistic in most implementations of the atomic clock. When the averaging time becomes large, the Allan deviation indeed will first decrease with $\tau^{-1/2}$ because most stationary noise is well averaged and will then level off or increase due to environmental or internal perturbations. The natural atomic resonance frequencies can be shifted from their unperturbed values by many systematic frequency shifts contributors like the magnetic field, light field, and buffer gas, as shown in Fig. 2.9. The frequency shifts do not cause a major problem for the compact atomic clock, which is not used as a master clock. The characteristics of such frequency shifts are typically adopted to build high sensitivity sensors [32, 94]. However, the instability of these frequency shifts typically affect the long-term frequency stability. Detailed physical mechanisms and explanations of these frequency shifts can be found in [4, 4, 6, 28, 38, 95–98]. Here, only important and necessary physical information related to the implementation is provided.

As mentioned before, the systematic frequency shift contributors are divided into two types: i) Environmental induced perturbations like the electric or magnetic fields; ii) Observational shifts like the instrumental effect and Doppler shift [28]. From the effects on the resonance signal, the frequency-shifting effects can also be distinguished into two categories [4]. The first category refers to the shift of the resonance center, which leads to a shift of the locking point. The second category refers to the line broadening the resonance signal, which also results in a shift of the lock point. In this part, we will focus on the first category of frequency shift contributors and leave the second category to the following part of this section. We will analyze different types of frequency shifts for the case of vapor-cell based CPT atomic clock and the effects on the resonance signal, which in turn help us to identify the specific frequency shift during characterization. This process also helps to track the limiting factor during a specific averaging time range for frequency stability performance.

Zeeman effect

One magnetic field is needed to provide an axis of quantization for the system and a reference axis for laser radiation polarization for an atomic clock. However, an undesired effect, referred to as the Zeeman effect, happens for the energy level of the atom. A constant dc magnetic field, applied to alkali atoms, splits the energy levels, as shown in Fig. 2.2, which is called the Zeeman effect. Thus, instead of having just two ground states, there are $4I + 2$ (I is the nuclear spin quantum number, $I = 7/2$ in Cs atom) energy sub-levels, allowing the formation of several Λ systems, depending on field direction and laser polarizations. This subject is extremely important to the atomic clock since the ground levels are displaced by the magnetic field. The Δ_{hf} is shifted from its nominal value, which means the accuracy of the atomic clock degrades. In order to compensate for the inaccuracy, a knowledge of the local magnetic field should be obtained. Also, the fluctuation of the magnetic field degrades the long-term stability performance of the atomic clock. The frequency shift Δf_{M} from the unperturbed resonance frequency f_{CPTo} caused by the magnetic field has the following form [28]:

$$f_{\mathrm{CPT}} - f_{\mathrm{CPTo}} = \Delta f_{\mathrm{M}} = C_{\mathrm{M1}}B + C_{\mathrm{M2}}B^2 + C_{\mathrm{M3}}B^3 + ..., \tag{2.22}$$

where f_{CPTo} is the resonance frequency when there is no external magnetic field, and C_{M1}, C_{M2}, and C_{M3} are the coefficients of different orders. Fortunately, for the resonance frequency of Λ system with $\Delta m = 0$ (referred as $\langle 0 - 0 \rangle$ resonance), C_{M1} is equal to 0, and $\Delta f_{\mathrm{M}} \approx C_{\mathrm{M2}}B^2$ when the magnetic field is small. For the case of Cs atom, C_{M2} is equal to 427.45×10^8 Hz/T^2.

Thus, an ideal magnetic field should be large enough to select the narrow $\langle 0 - 0 \rangle$ resonance signal and small enough to reduce the second-order effect on the $\langle 0 - 0 \rangle$ resonance frequency. Moreover, the direction of magnetic field should be well controlled because the amplitude of the CPT resonance signal is proportional to $\cos^2(\theta)$, where θ is the angle between the direction of laser propagation and the magnetic field [4].

The other Zeeman sub-levels may play a role in the evolution of the system. Decay from the excited state takes place to all ground-state Zeeman sublevels due to spontaneous emission and atomic collisions when the buffer gas is used. Consequently, atoms may find a path to a Zeeman sublevel not involved in the Λ scheme. In such a case, the system is no longer closed and atoms may be trapped in a level like $m_F = +4$ or $m_F = -4$ for Cs atom as shown in Fig. 2.2, depending on the polarization used. Consequently, it is necessary to use a four-level system including a trap to explain some of the results obtained, like reduced signal contrast [84].

Stark effect, light shift

An electric field applied to an atom also produces a frequency shift of atomic resonance frequency. This is called the Stark effect [99]. The light field not only induces optical transitions but also shifts the relative energy levels of the two states through the AC Stark effect [96]. Compared to optically pumped atomic clocks, light shifts are reduced in CPT atomic clock, because of a more symmetric system. The theory of the CPT maser developed in [97] shows that the residual light shift caused by the difference of intensity of the radiation field involved in Λ scheme excitation is given by:

$$\Delta\omega_{LS} = -\frac{1}{4}\left(\frac{\Delta_o}{(\Gamma^*/2)^2 + \Delta_o^2}\right)[\omega_{1R} - \omega_{2R}] \tag{2.23}$$

where it is assumed that the frequencies of the two light fields ω_1 and ω_2 are detuned from ω_{31} and ω_{32} by the same quantity Δ_o, ω_{1R} and ω_{2R} are the Rabi frequency of these two light fields, Γ^* is the decay rate from the excited state to the ground-state levels.

The laser radiation, at each of the transitions of the Λ scheme interacts with the other transition and is out of resonance for that particular transition. Further, sidebands of the modulating RF signal and the carrier are non-resonant with the various transitions as illustrated in Fig. 2.4. A more comprehensive calculation for the light shift has been done in [5]:

$$\Delta\omega_{LS} = \left(\frac{\omega_{RL}}{\omega_{hf}}\right)^2\left\{\Theta(m) + \xi(m)\left(\frac{\Delta_0}{\omega_{hf}}\right)^2\right\} \tag{2.24}$$

where ω_{RL} is the Rabi frequency of the laser radiation without frequency modulation, m is the modulation index, $\Theta(m)$ and $\xi(m)$ are defined as:

$$\Theta(m) = J_0^2(m) + \frac{1}{2}J_{p/2}^2(m) - 2\sum_{n=1,n\neq p/2}^{\infty} J_n^2(m)\frac{p^2}{(2n)^2 - p^2} \tag{2.25}$$

$$\xi(m) = 4J_0^2(m) + \frac{1}{2}J_{p/2}^2(m) - 8\sum_{n=1,n\neq p/2}^{\infty} J_n^2(m)\frac{12n^2 + p^2}{((2n)^2 - p^2)^3}p^4 \tag{2.26}$$

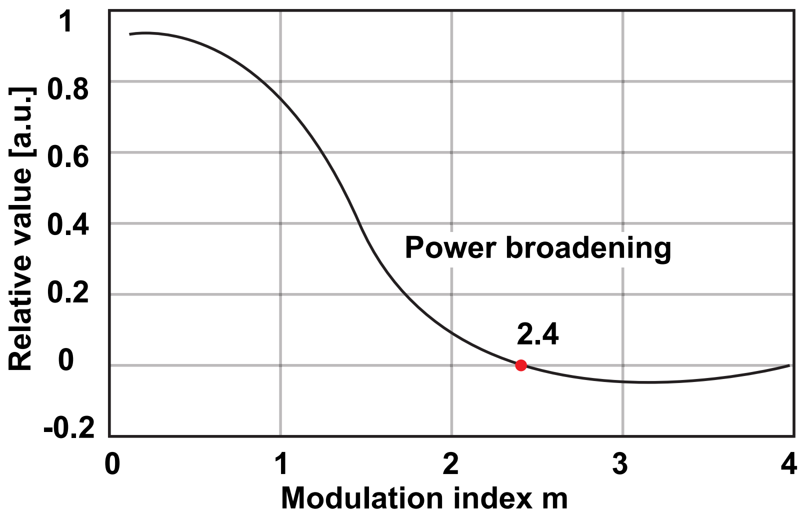

Figure 2.10: Graphical representation of the power light shift coefficient in the CPT atomic clock [5].

where J is the angular momentum operator, p is the frequency division of hyperfine frequency and modulation frequency (is equal to 2 in ULPAC). The $\Theta(m)$ and $\xi(m)$ represent the power light shift and quadratic light shift, respectively. The power light shift is independent of laser tuning, while the quadratic light shift depends on the square of frequency tuning of the laser. These contributions can be explained qualitatively by means of a simple three-level model. The light shift originates from the combined effects of the residual carrier and the sidebands on the optical transitions that are part of the CPT Λ scheme. It was found that both contributions may be made to vanish with a proper modulation index m. From Fig. 2.10, it is obvious that when the modulation index of the laser is around 2.4, the power light shift coefficient is close to zero.

A strategy to reduce the signal fluctuation due to the light shift is one of the key issues for improving long-term stability. A method to stabilize the light shift, different from the previous report [100], is considered as an optimization of driving condition for VCSEL, and it is applied for ULPAC.

Doppler effect

The Doppler effect is illustrated in Fig. 2.11, where a source emits a wave propagating at speed c. When the source is at still, the wavelength and frequency observed obey the relation:

$$\lambda_0 \nu_0 = c \tag{2.27}$$

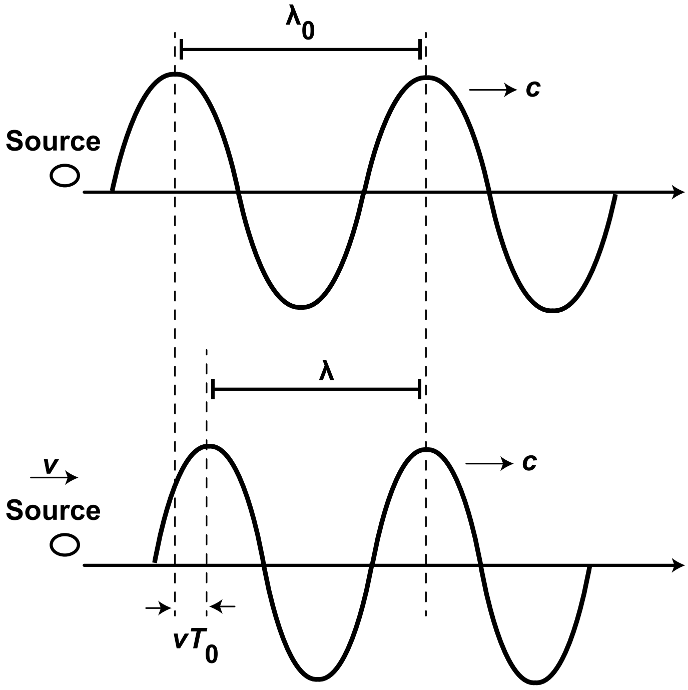

Figure 2.11: Illustration for the classical Doppler effect [6].

with the period given by:

$$T_0 = 1/\nu_0 \tag{2.28}$$

If the source is moving in the direction of wave propagation with a speed of υ, then the wavelength becomes:

$$\lambda = \lambda_0 - \upsilon T_0 \tag{2.29}$$

From Eqs. (2.27), (2.28) and (2.29), we obtain:

$$\lambda = \lambda_0(1 - \upsilon/c) \tag{2.30}$$

and

$$\nu = \frac{\nu_0}{1 - \upsilon/c} \cong \nu_0(1 + \upsilon/c) \tag{2.31}$$

where it has been assumed that $\upsilon/c \ll 1$. The above simple classical approach shows the observed frequency has a first-order relationship with the source speed, as indicated by the term $\nu_0 \upsilon/c$ in Eq. (2.31). By the rigorous relativistic approach, higher-order Doppler shifts can be theoretically calculated as well [28,46]:

$$f' = f\gamma\left(1 - \frac{\upsilon'_{\parallel}}{c}\right) \tag{2.32}$$

where f is the nominal probing frequency, f' is the frequency observed in a moving frame, $\gamma = [1 - (\upsilon'/c)^2]^{-1/2}$, υ' is the velocity of atom relative to the laboratory frame, $\upsilon'_{\parallel}$ is the velocity of atom along the probing laser beam direction. The frequency servo loop ensures that the probing frequency equals the atomic resonance frequency f_0; that is, $\langle f' \rangle = f_0$, where the angle brackets denote the appropriate average over the laser probe duration. If assuming that f is constant over this duration, then $\langle f \rangle = f$, and we have:

$$\frac{f - f_0}{f_0} = \frac{\langle \upsilon \rangle}{c} - \frac{\langle \upsilon^2 \rangle}{2c^2} + \frac{\langle \upsilon_{\parallel} \rangle^2}{c^2} + O(\upsilon/c)^3 \tag{2.33}$$

The first term in Eq. (2.33) represents the first-order Doppler shift. The next two terms in Eq. (2.33) represents the second-order Doppler shifts, which can be largest systematic uncertainty in the case of ion optical clocks [28]. Thus, for the atomic clock where an ensemble of atoms are adopted, the Doppler shifts should be considered.

Buffer gas shift

One technique for reducing the Doppler effect is to restrict the motion of atoms while they are in interaction with the radiation [101]. This is typically realized by inserting buffer gas into the vapor atom cell. In the vapor cell based atomic clock, the spin depolarization of atoms caused by collisions between the atoms and untreated glass cell walls also broadens the line width of the CPT. The addition of the inert buffer gas mitigates the collision effect as well. Gases such as N_2, Ar and He interact only very weakly with the spin of alkali atoms and hence the atoms can undergo many collisions with the buffer gas before spin depolarizes.

However, the collisions between the atoms and buffer gas still produce frequency shift. This shift is proportional to the buffer-gas density or to atom cell pressure P. Furthermore, this shift is affected by temperature variations. The shift caused by the buffer gas is given as [6]:

$$\Delta\nu_{\text{bg}} = P_{\text{o}}[\beta_{\text{o}} + \delta_{\text{o}}(T - T_{\text{o}}) + \gamma_{\text{o}}(T - T_{\text{o}})^2] \tag{2.34}$$

where P_{o} is the buffer gas pressure, β_{o} is the pressure-shift coefficient, δ_{o} and γ_{o} are the first- and second-order temperature coefficients, respectively, T is the temperature of the

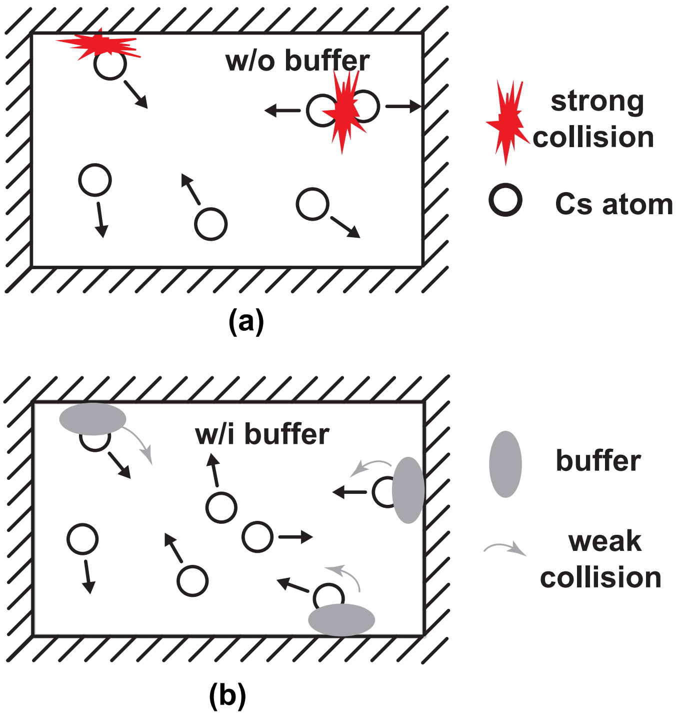

Figure 2.12: (a) Illustration of collisions between the atoms. (b) Illustration of collisions between the atom and buffer gas.

atom cell, and T_o is the reference temperature at which the coefficients are measured. The cell pressure variation is solved by using a mixture of two or several types of buffer gases, such as Ar and N_2 because they have opposite temperature-dependent pressure characteristics. When the ratio of these two gases is 2.55, then the pressure can be kept relatively flat in the typical operation temperature range.

2.4.3 Line broadening mechanisms

The narrow CPT resonance width is the one key characteristic for the superiority of the atomic clock over an electro-mechanical based clock, which also determines the quality factor. Every excited quantum state has an intrinsic lifetime before it spontaneously decays to a lower energy state. The natural width of the spectral line is decided by the uncertainty principle. The energy level above the ground state with energy E and lifetime Δt has uncertainty in energy:

$$\Delta E \Delta t \sim \hbar \tag{2.35}$$

A photon emitted in a transition from this level to the ground state thus has a range of frequencies:

$$\Delta\nu \sim \frac{\Delta E}{h} \sim \frac{1}{2\pi\Delta t} \tag{2.36}$$

This is referred to as natural broadening. The lifetime Δt determines the natural linewidth. The natural line profile is a Lorentzian line sharp:

$$\phi(\nu) = \frac{\gamma/4\pi^2}{(\nu-\nu_0)^2 + (\gamma/4\pi)^2} \tag{2.37}$$

where γ is the spontaneous decay rate. The signal width of the atomic resonance signal is inversely proportional to the lifetime of the coherent state. Since the ground hyperfine states have equal parity, the dominant radiative decay process is the magnetic dipole transition connection between these two states with a spontaneous lifetime of several thousand years [4]. Thus, decoherence is determined by all kinds of line broadening mechanisms. The line broadening affects the signal amplitude, contrast and qualify factor, degrading the short-term frequency stability performance. Furthermore, the perturbations that cause the line broadening are very often the cause of important frequency shifts. The broadening mechanisms can be divided into two major types: i) energy levels are not infinitely sharp; 2) atoms are moving relative to the observer. The former includes the natural broadening, power broadening and pressure broadening for the vapor-cell based atomic clock, while the latter mainly refers to the Doppler broadening.

Pressure broadening

One of the major contributions for the resonance linewidth is collisions between the atoms and the cell walls. To mitigate this effect, additional buffer gas is inserted into the atom cell, which slows down the averaging velocity of the thermal atoms and increases the time to reach the cell wall. The buffer gas has an additional benefit for eliminating the Doppler broadening through Lamb-Dicke narrowing [6, 101]. The insertion of buffer gas introduces a diffusive motion for the alkali atoms in the cell. Thus, two effects exist for the linewidth. One is the diffusion of the atoms and the other is the buffer gas collision, which is affected by the buffer gas pressure [9]. Because the relaxation from the walls is inversely proportional to buffer gas pressure, while the relaxation from buffer gas collisions has a proportional relationship with the buffer gas pressure. Thus, there is an optimal pressure value for the relaxation rate, which plays an important role in signal amplitude. The relaxation rate for a diffusion mode ν is then given by [79]:

$$\Gamma_\nu = \gamma_0\left(\frac{P}{760Torr}\right) + \frac{D_0}{\Lambda_\nu^2}\left(\frac{760Torr}{P}\right) \tag{2.38}$$

where δ_0 and D_0 are the relaxation rate and diffusion constant of alkali atoms at $760Torr$, and Λ_ν is the diffusion length for the mode ν. Because of other order diffusions decay too rapidly, typically only the lowest-order diffusion mode is considered, for which $\Lambda_\nu \approx L$, where L is the length of the atom cell. For a cylindrical cell of radius a and length L, the diffusion length of the lowest-order is given by [6]:

$$\frac{1}{\Lambda_0^2} = \left[\frac{(2.405)^2}{a^2} + \frac{\pi^2}{L^2}\right] \tag{2.39}$$

From Eq. (2.38), the relaxation rate of the lowest-order diffusion mode exhibits a minimum broadening near a pressure of:

$$P_{\text{opt}} = \sqrt{\frac{D_0}{\gamma_0}\frac{1}{\Lambda_0}}(760Torr) \tag{2.40}$$

for which the relaxation rate is $\Gamma_0 = 2\frac{\sqrt{\gamma_0 D_0}}{\Lambda_0}$ and the broadened transition linewidth is given by:

$$\Delta\nu_{\text{BG}} = \frac{2}{\pi}\frac{\sqrt{\gamma_0 D_0}}{\Lambda_0} \tag{2.41}$$

The buffer gas also causes considerable depolarization for the excited state, which is typically around several hundred megahertz [102]. The broadening of the excited states should be kept less than the ground-state hyperfine frequency, beyond which the signal contrast of the atomic resonance is drastically reduced [98, 103, 104].

Power broadening

The line profile of CPT resonance may also be affected by the radiation intensity, referred to as power broadening. For any wavelength detuning, an increase of laser intensity causes more population to visit the excited state, and so increases the signal. The line width is determined by the range of detuning for which the excited state acquires an appreciable transient population during excitation pulse; because this detuning range increases with the excitation intensity, such observations display power broadening [105]. Thus, the laser output power should be carefully controlled to minimize the power broadening for the resonance CPT signal. A linear relation between the FWHM and g_Λ^2 is expected [4,98]:

$$\mathrm{FWHM} = 2\Gamma_{12} + g_\Lambda^2/(\gamma_1 + \gamma_2) \tag{2.42}$$

where Γ_{12} is the dephasing of the ground state coherence, γ_1 and γ_2 are the population decay rates from the excited state into ground states $|1\rangle$ and $|2\rangle$, respectively. However, the linear relationship of Eq. (2.42) is assuming that the intensity of the laser is below the coherence saturation intensity:

$$I_\mathrm{c} = 4\pi hc\Gamma_{12}/3\lambda^3 \tag{2.43}$$

where λ is the wavelength of the laser output light.

Doppler broadening

The Doppler effect not only shifts the frequency of the CPT resonance signal but also broadens the linewidth since the motion of the individual atoms is random. This effect depends on the mass of the atom, the frequency of the line and the temperature. Doppler broadening largely determines the shape of the lines in most stratospheres where the low-pressure limits pressure broadening and the high temperatures increase the effect of Doppler broadening. The width at the half the height is given by [6]:

$$\Delta\nu_\mathrm{D} = 2\nu_0\left(\frac{2k_\mathrm{B}T}{Mc^2}\ln 2\right)^{1/2} \tag{2.44}$$

The buffer gas used to mitigate the Doppler shift also effectively narrows the Doppler broadening.

All of the frequency shift contributors and line broadening mechanisms mentioned in this section should be carefully mitigated to obtain excellent frequency stability and are well addressed in the implementation of ULPAC.

Chapter 3

Atomic Clock Implementation

For a chip-scale size, a novel and compact architecture is required for the quantum physical package, while maintaining robust and long-term operation. Frequency probing and locking circuits implemented in CMOS technology achieve low power consumption. Besides low noise circuit design techniques and long-term frequency shift control loops are incorporated to reach the frequency stability specifications of LEO smallsat constellations.

The complete detailed system diagram is shown in Fig. 3.1. It mainly consists of three parts: 1) quantum physical package; 2) frequency shift control loops; 3) probing and locking circuits. This chapter gives the details of the implementation of the whole system.

3.1 Quantum Physical Package

As the core component of the compact atomic clock, the performance of the quantum physical package is of great importance for the system performance. The interior part of the quantum physical package is the main physical setup for the excitation of atomic CPT resonance, as shown in Fig. 3.2.

The size of the quantum physical package typically determines the volume of the atomic clock, which is dominant by the size of the vapor atom cell. Even though there is no fundamental limit on the atom cells for the CPT based atomic clock as compared with that of the optical pumping based atomic clock, the size of the vapor cell in CPT is still limited by some practical implementation factors. One major consideration is the line broadening caused by the collisions between alkali atoms. There is a trade-off between the cell size and alkali atom density for maintaining the constant resonance signal amplitude. Besides the gas leakage and mechanical robustness become serious issues when the

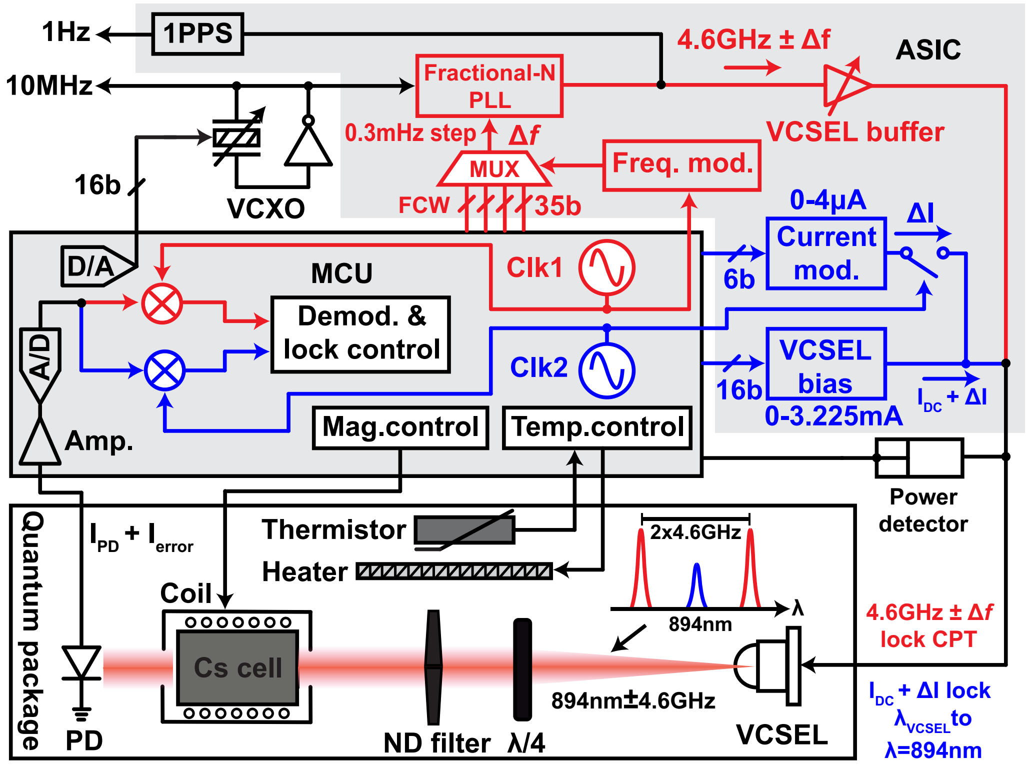

Figure 3.1: Complete system diagram of ULPAC.

atom cell becomes relatively small. These affect the long-term frequency stability and aging performance. The manufacturing yield becomes low if the vapor atom cell is reduced to be very small, which adds the cost considerably.

The size of the atom cell also sets a lower bound for the power consumption of the quantum physical package since most of the power budget is used to heat and maintain Cs atoms in the gas phase. In order to increase power efficiency, special design techniques are applied to the quantum physical package.

Figure 3.3 (a) shows the top-down view of the integration of a heater, a VCSEL, and a thermistor as a temperature sensor on the same base. The VCSEL is located in the center of the base. The thermistor layouts close to the VCSEL and is used to detect the internal temperature. Since the temperature affects the wavelength of VCSEL and various performance of the atom cell, the internal temperature should be monitored and controlled with high accuracy. The heater pattern is circular around the VCSEL and tries to heat the VCSEL and the atom cell equally. The light of the VCSEL is circularly polarized by a $\lambda/4$ plate for the $\langle 0-0 \rangle$ resonance, and the intensity is adjusted by a neutral density (ND) filter. The light is then used to trigger the atomic resonance in the atom cell. Finally, the CPT resonance signal is detected by a PD.

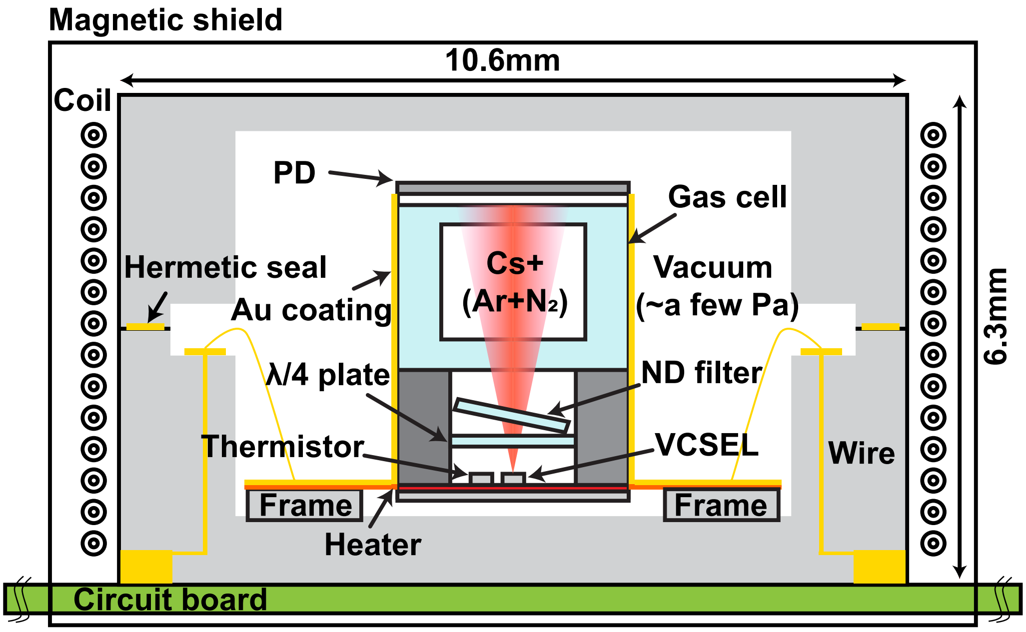

Figure 3.2: Compact quantum physical package architecture for ULPAC.

The vapor cell filled with Cs atoms is entirely composed of silica glass. Cs vapor is introduced into the silica glass container through a distillation process, and then it is preserved by glass fusion sealing.

The VCSEL is a key component of the quantum physical package. The requirements of the atomic clock on the VCSEL are quite demanding, as compared with those of data communication applications. First, the VCSEL should have a single-mode operating at a wavelength of 894.6 nm. Mode competition in a conventional VCSEL can cause amplitude noise in light power [106, 107]. In addition, due to the high-temperature sensitivity (around 19 GHz/K), the wavelength of the VCSEL should be accurate to be within ±0.5 nm for a typical temperature control accuracy. The linewidth of the VCSEL should be less than 100 MHz for better short-term stability of the atomic clock. The frequency noise of the VCSEL light will affect the signal amplitude of the optical pumping, thus degrading the S/N ratio of the CPT.

The schematic of the VCSEL is shown in Fig. 3.4. A bottom-distributed Bragg reflector (DBR), quantum wells and a top-DBR are grown on a GaAs substrate. The bottom-DBR is designed with n-doped $\lambda/4$ layers and the top-DBR is designed with p-doped layers. The reflectivity of the bottom-DBR is higher than that of the top-DBR for light efficiency. The quantum wells formed in the active region provide an optical gain near 894.6 nm within about ±10 nm full width at a temperature of $80\,^oC$, which is the operating temperature of the quantum physical package. A mesa structure is formed by the

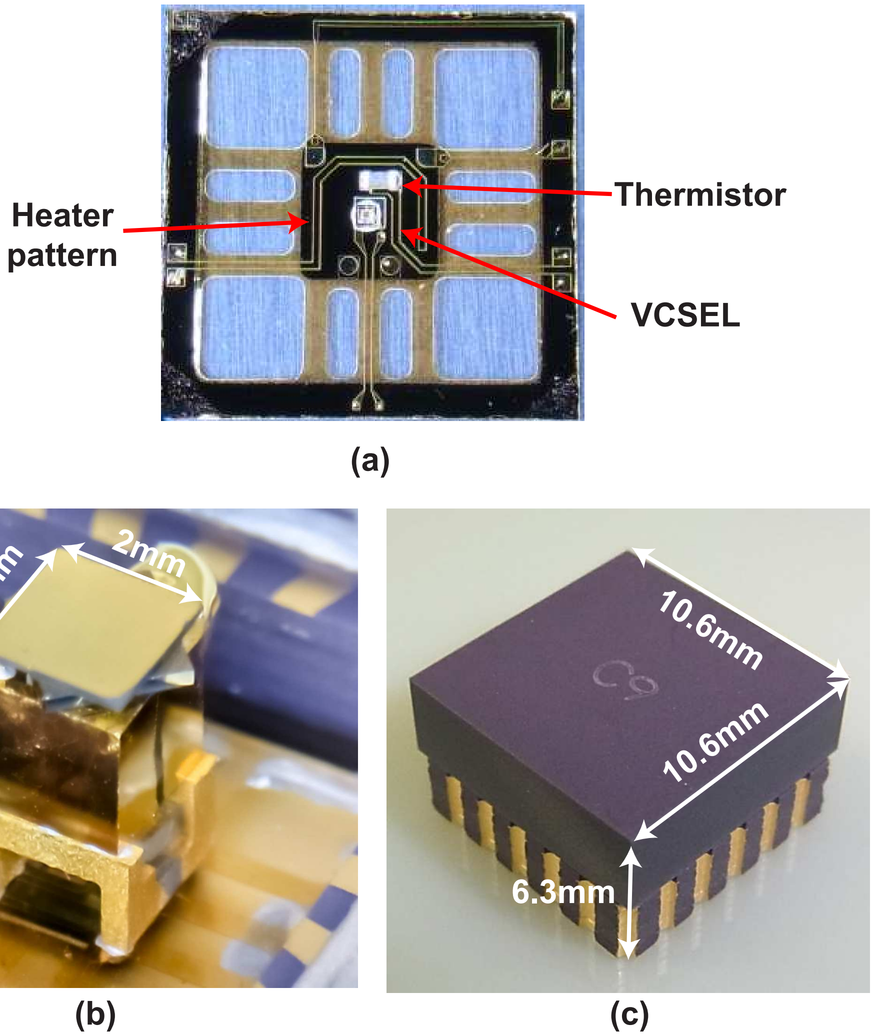

Figure 3.3: (a) Top-down view of integration base. (b) Photograph of interior design of the quantum physical package. (c) Photograph of the sealed quantum physical package.

dry etching technique. An oxide aperture in the top-DBR is formed to limit the current to the center of the mesa structure and also for lateral optical confinement. A polyimide layer is embedded around the mesa structure in order to reduce the parasitic capacitance for high-frequency tuning.

For the low power consumption, a new suspended architecture of the interior setup is designed. A coating of Au is adopted in order to improve the thermal isolation, and a vacuum package is realized using a hermetic seal to reduce the heat conversion. By these techniques, the heater consumes only 9.1 mW power to maintain the temperature at 80 ^{o}C.

Figure 3.3 (b) shows the interior design of the quantum physical package with a size of only 2 mm $\times$ 2 mm $\times$ 4 mm, and Fig. 3.3(c) shows the sealed quantum physical pack-

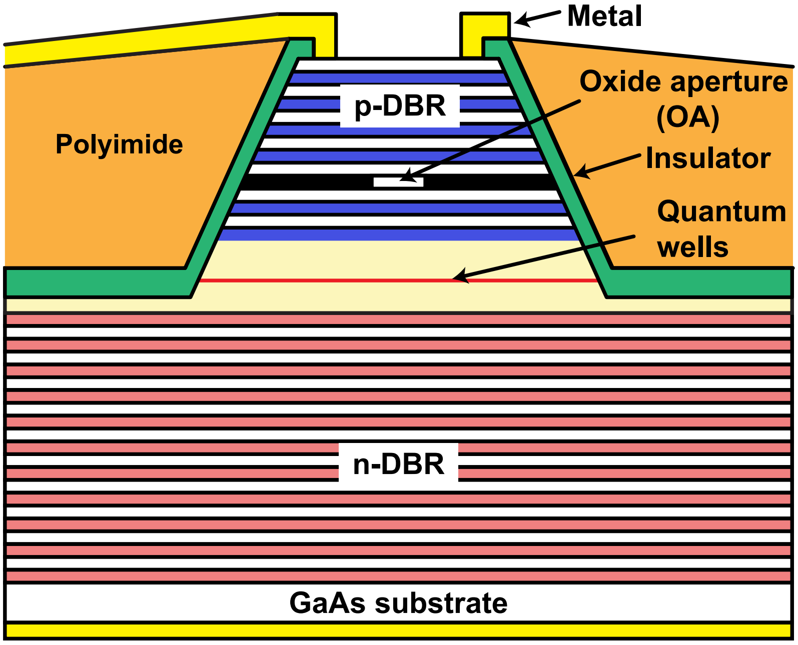

Figure 3.4: VCSEL cross-sectional schematic diagram.

age with a volume of only 10.6 mm × 10.6 mm × 6.3 mm.

Further miniaturization of this quantum physical package using MEMS technology (to a promising size of less than 1 cm^3) is also under development [68, 108, 109].

3.2 Additional Control Loops

For a high-performance atomic clock, additional control loops and design considerations are needed to address the internal or external frequency perturbation factors.

i) Temperature control loop: Constant temperature is needed to minimize buffer gas shift, maintain the constant wavelength of VCSEL and the pressure of atom cell. Due to the high-frequency stability requirement of the atomic clock, the temperature control accuracy should be below ±1 mK. A heater is used to heat both the VCSEL and the atom cell and to maintain a constant temperature in conjunction with a thermistor. The temperature accuracy is controlled within ±1 mK by a microcontroller unit (MCU) with a 16-bit DAC. In this way, both the wavelength of the VCSEL and the pressure of the atom cell are kept constant in order to mitigate the frequency shift caused by the light shift and buffer gas.

ii) The magnetic field has twofold effects on the CPT resonance. On one side, a small magnetic field is required to select $\langle 0 - 0 \rangle$ resonance, whose resonance frequency is almost first-order independent of the magnetic field. One the other hand, large external

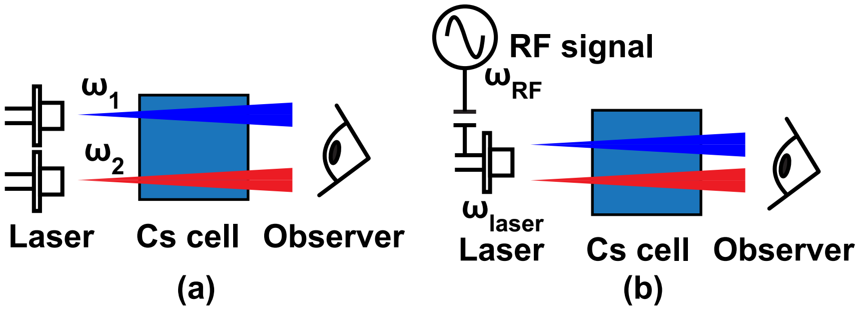

Figure 3.5: Methods of generating two phase coherent light fields: (a) two lasers method and (b) RF modulated single laser method.

magnetic field such as the earth magnetic field should be well shielded to reduce the second-order effect on the resonance frequency. The magnetic field is carefully controlled for the quantum physical package. First, a 10 μT unidirectional magnetic field required by the detection of the $\langle 0-0 \rangle$ CPT resonance signal is produced by controlling the current driving the coil in the quantum physical package. The external environmental magnetic field (particularly, the earth magnetic field) is shielded by the magnetic shield package. The supporting materials inside the package are also chosen to be less magnetic in order to further reduce the variations.

iii) The coherence loss due to the collision between the atoms and the cell wall is mitigated by inserting additional buffer gas into the atom cell. The cell pressure variation is solved by inserting a mixture of Ar and N_2 because these two buffer gases have opposite temperature-dependent pressure characteristics. If the ratio of these two gases is 2.55, then the pressure can be kept relatively flat in the typical operating temperature range.

3.3 Probing and Locking Circuits

Instead of using two lasers to produce two phase coherent light fields as shown in Fig. 3.5 (a), a RF modulated single laser is adopted to generate the required light fields for the CPT resonance, as shown in Fig. 3.5 (b). Thus, the laser wavelength should be locked to 894 nm and the RF modulation signal should be locked to half of the hyperfine frequency. The circuit implemented in a standard CMOS 65 nm is shown in Fig. 3.6.

3.3.1 Laser wavelength locking loop

In order to lock the wavelength of the VCSEL to 894.6 nm, a modulated dc current source is used. The wavelength of the VCSEL has an almost linear relationship with the driving

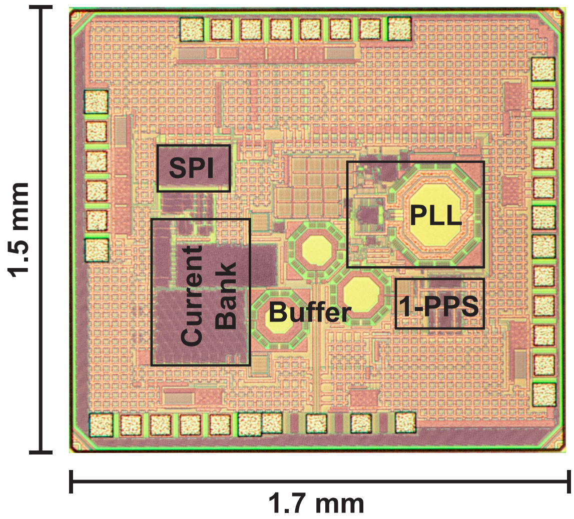

Figure 3.6: Chip die photo of probing and locking circuit as well as out ports circuit.

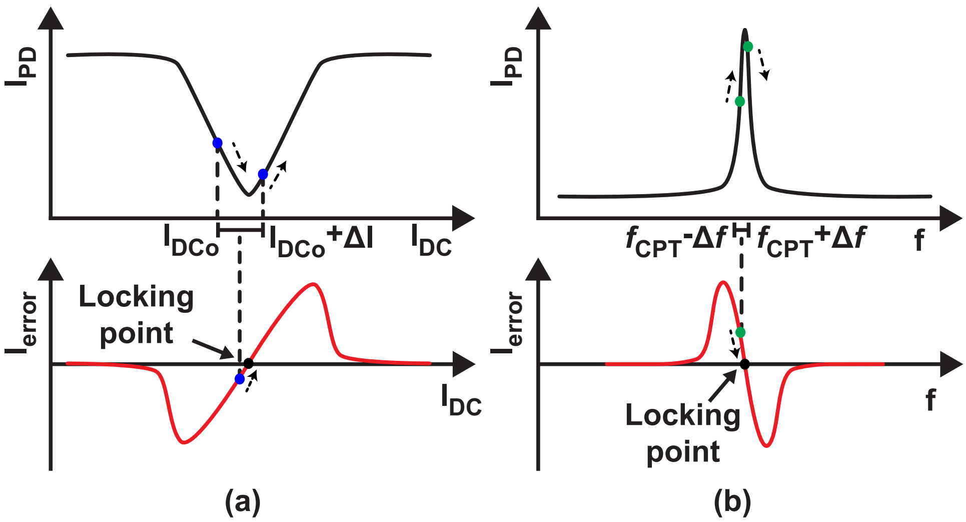

Figure 3.7: (a) Modulation dc current source for the wavelength loop. (b) Modulation RF signal for the frequency locking loop.

current. As shown in Fig. 3.7 (a), if the driving current for the VCSEL is swept, then the PD current reflects the optical pumping of the Cs atoms inside the atom cell. The bottom peak is the locking point for the VCSEL wavelength. The peak of maximal light absorption is the locking point for the VCSEL wavelength when the RF modulation is not applied. Here, a small modulated current is combined with a dc current to produce I_{DCo} and $I_{DCo} + \Delta I$ as two search values. The averaged error signal after demodulation indicates the direction of the next step movement of the dc current. The detailed modulation and demodulation methods are shown in Fig. 3.8. In this way, the wavelength of the

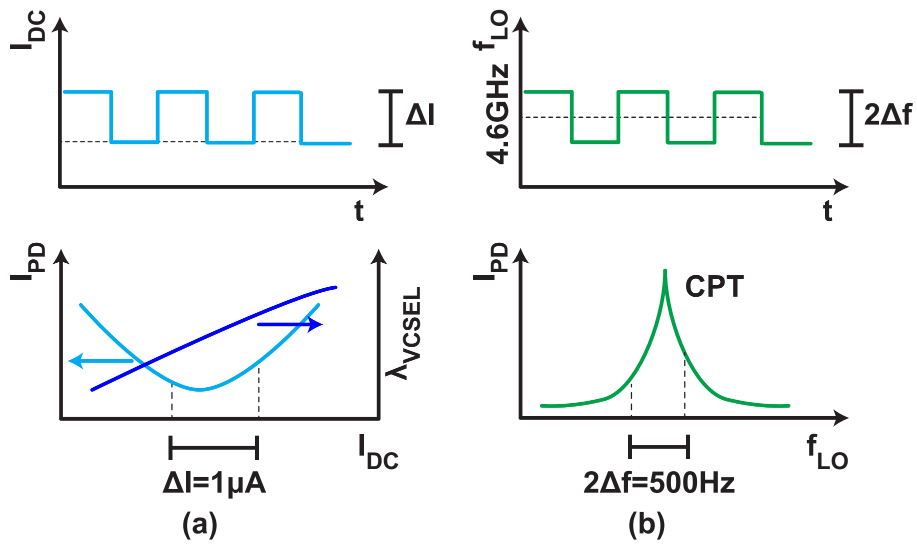

Figure 3.8: The detailed modulation and demodulation (a) current domain wavelength locking loop, (b) frequency domain RF signal locking loop.

Table 3.1: The general design requirements on the current source.

Parameter	Target	Reasons
Current turning range	>3 mA	VCSEL tuning characteristics
Current resolution	<0.4 μA/bit	Quality factor
RMS current noise	<0.1 μA	Short-term stability
Temperature coefficient	<100 ppm/C	Short-term stability
Supply variation	<100 μA/V	Short-term stability

VCSEL is well locked.

The general requirments on the current source are listed in Table 3.1. Two prior arts of current source are shown in Fig. 3.9. Both architectures are quite simple. But they suffer from the noise from the R-DAC, large area and worse linearity. Also the temperature coefficient of on-chip resistor is typically larger than 200 ppm/C. The detailed circuit implementations of the dc current source and the modulated current source are shown in Fig. 3.10 (a). The dc current source is further divided into a fine current bank and a coarse current bank with a current range of 0-3.225 mA. The modulating current source can provide a range of 0-4 μA, which is modulated at 9.7 kHz. Since an RF signal also exists at the VCSEL port, an isolation consisting of an inductor and a capacitor is used to reduce the dc current sensitivity due to the RF amplitude. All of these current source

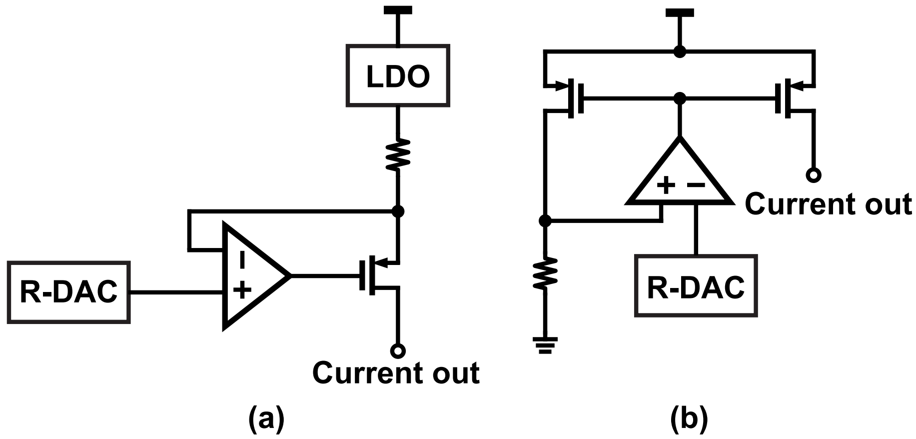

Figure 3.9: Two prior arts of current source: (a) LDO based current source (b) op-amp based current source.

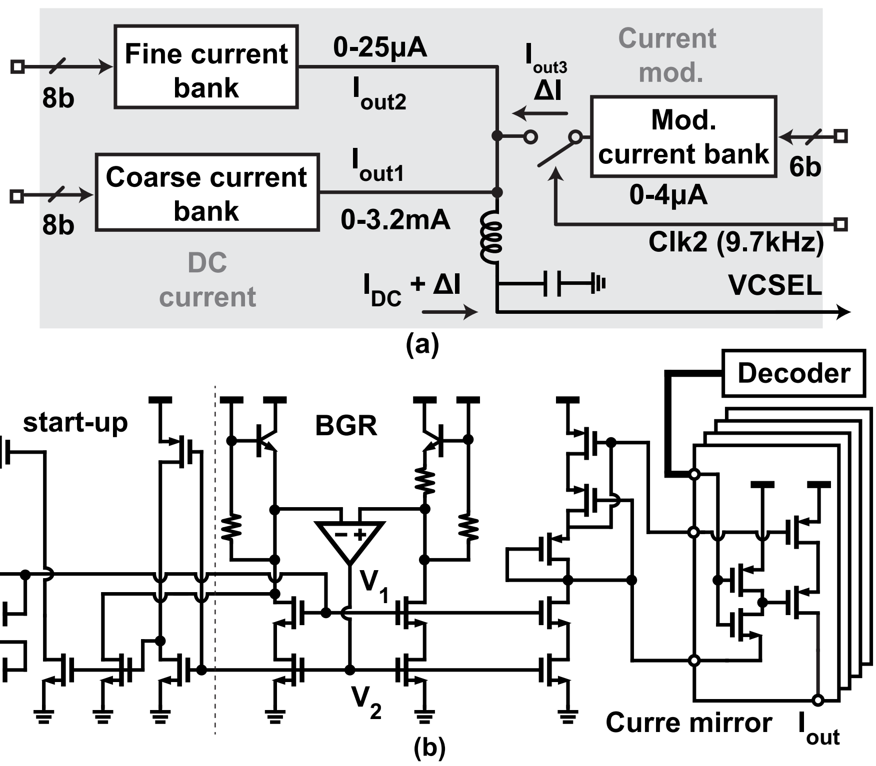

Figure 3.10: (a) Circuits of the wavelength locking loop. (b) Current source bank architecture.

banks are programmable and share a similar architecture, as shown in Fig. 3.10 (b). In order to achieve better linearity, a binary-to-thermometer decoder with the same unit current source is adopted for each control bit. The root-mean-square (RMS) current noise

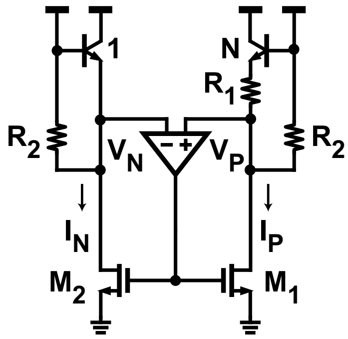

Figure 3.11: Simplified bang gap reference for temperature coefficient analysis.

of the current source should be kept smaller than 0.1 μA, otherwise, the RMS wavelength offset of laser will be larger than 100 MHz, which causes obvious asymmetry of the line shape from an ideal Lorentzian line. Also, the resonance signal amplitude and contrast will be affected. The current noise of the current source bank is dominated by the flicker noise, which is reduced by optimizing the transistor size. The biasing voltages (V_1 and V_2) for the current mirror in the current source banks are generated from a bandgap voltage reference, as shown in Fig. 3.10 (b), in order to further reduce the current variation due to temperature changes. The cascode structure is adopted in the bandgap core to improve the power rejection ratio. The temperature coefficient on-chip resistor is compensated by two resistors on the right side of the BGR core with the opposite temperature characteristic of V_{BE} and V_{t} of the bipolar trasistor, as shown in Fig. 3.11. The voltage drop on the R_1 can be derived as:

$$V_{\mathrm{R1}} = \Delta V_{\mathrm{BE}} = V_{\mathrm{t}} \ln \tag{3.1}$$

The currents of $\mathrm{I_N}$ and $\mathrm{I_P}$ can be calculated as:

$$I_{\mathrm{N}} = I_{\mathrm{P}} = \frac{V_{\mathrm{R1}}}{R_1} + \frac{V_{\mathrm{BE}}}{R_2} \tag{3.2}$$

Every parameter in the right hand of Eq. (3.2) has a temperature coefficient, thus Eq. (3.2) can be further expressed:

$$I_{\mathrm{N}} = \frac{V_{\mathrm{R1,0}}(1 + TC_{\mathrm{VR1}} \cdot T)}{R_{1,0}(1 + TC_{\mathrm{R}} \cdot T)} + \frac{V_{\mathrm{BE,0}}(1 + TC_{\mathrm{VBE}} \cdot T)}{R_{2,0}(1 + TC_{\mathrm{R}} \cdot T)} \tag{3.3}$$

where the $V_{\mathrm{R1,0}}$, $R_{1,0}$, $V_{\mathrm{BE,0}}$ and $R_{2,0}$ are temperature-independent constants of V_{R1}, R_1, V_{BE} and R_2, respectively. And TC_{VR1}, TC_{R}, TC_{VBE} and TC_{R} are the temperature coefficients of V_{R1}, R_1, V_{BE} and R_2, respectively. Thus, in order to get temperature-independent current,

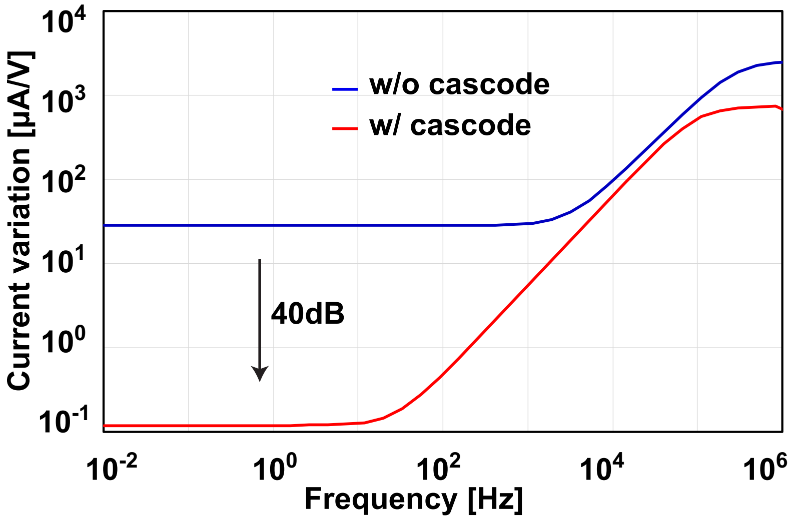

Figure 3.12: Simulated current variation results with supply noise.

the following equation should be satisfied:

$$\frac{\partial I_{\mathrm{N}}}{\partial T} = \frac{V_{\mathrm{R1,0}}(TC_{\mathrm{VR1}} - TC_{\mathrm{R}})}{R_{1,0}(1 + TC_{\mathrm{R}} \cdot T)^2} + \frac{V_{\mathrm{BE,0}}(TC_{\mathrm{VBE}} - TC_{\mathrm{R}})}{R_{2,0}(1 + TC_{\mathrm{R}} \cdot T)^2} = 0 \tag{3.4}$$

which also translates into:

$$\frac{R_{2,0}}{R_{1,0}} = -\frac{V_{\mathrm{BE,0}}(TC_{\mathrm{VBE}} - TC_{\mathrm{R}})}{V_{\mathrm{R1,0}}(TC_{\mathrm{VR1}} - TC_{\mathrm{R}})} \tag{3.5}$$

Since TC_{VBE} is below 0, solution for Eq. (3.5) is available if TC_{R} is smaller than TC_{VR1}.

Figure 3.12 shows the simulated current variation results with supply noise. The cascode structure improves 40 dB for the low-frequency supply noise as compared with that of non-cascode structure. The on-chip decoupling capacitor is used to filter the high-frequency supply noise. The simulated temperature characteristic of this bandgap is shown in Fig .3.13. 0.7% current output error is achieved in the temperature range from -60 ^{o}C to 80 ^{o}C under the supply voltage range from 2.7 V to 3.3 V. Even in the temperature range of -80 ^{o}C to 80 ^{o}C, only 1.65% current output error is maintained. Since the required operating temperature range of ULPAC is from -10 ^{o}C to 70 ^{o}C, less than 0.7% current variation is anticipated. The temperature characteristic of the current source bank biased by the bandgap reference is also simulated and shown in Fig. 3.14. The maximum temperature coefficient for this current source bank is 50 ppm/^{o}C. By these techniques, the theoretically calculated VCSEL wavelength variation could be ensured to be less than

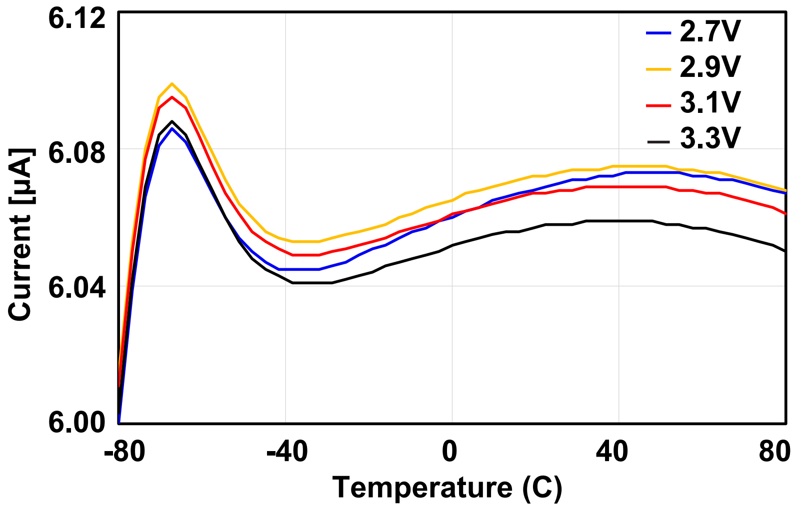

Figure 3.13: Simulated current variation results with temperature variations and voltage variations.

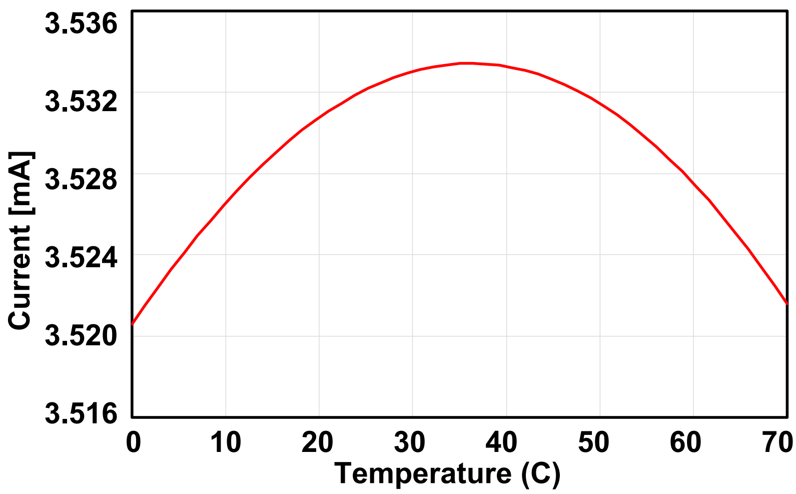

Figure 3.14: Simulated current variation of current source bank when the temperature changes.

100 MHz. The performance summary of this current source and comparison with other work are listed in Table 3.2.

3.3.2 RF modulation frequency locking loop

Following the wavelength locking method, a modulated fractional-N PLL is used to generate $f_{\text{CPT}} - \Delta f$ and $f_{\text{CPT}} + \Delta f$ to search the peak of the CPT resonance signal, as shown in Fig. 3.7 (b). One VCSEL buffer is designed to amplify the RF signal to reach the required

Table 3.2: Performance comparison of current source.

	Target	This work	[110]	[8]
Implementation	On chip	On chip	Off chip	Off chip
Cuurent turning range	>3 mA	3.2 mA	N/A	N/A
Current resolution	<0.4 μA/bit	<0.1 μA/bit	N/A	N/A
RMS current noise	<0.1 μA	<0.102 μA	N/A	N/A
Temperature coefficient	<100 ppm/C	50 ppm/C	2 ppm/C	180 ppm/C
Supply variation	<100 μA/V	10 μA/V	200 μA/V	N/A

power level to drive the VCSEL. The detailed schematics of the PLL and VCSEL buffer are shown in Fig. 3.15.

The PLL mainly consists of a phase-frequency detector (PFD), charge pump (CP), low pass filter (LPF), voltage-controlled oscillator (VCO), multi-module divider (MMD) and delta sigma modulator (DSM). The PFD compares both frequency and phase differences between reference signal and feedback signal from the divider and generates the error signal that is proportional to the phase difference. This error signal is converted from time domain to the voltage doain by using CP and LPF. The LPF also filters the high frequency component of the error signal, which helps to reduce the spur. The VCO produecs an output frequency that is proportional to the voltage input from the LPF. The DSM controlled MMD forms a fractional-N divider. The fractional-N divider divides the high output frequency of VCO to a low frequency FB signal, whose frequency should be exactly equal to the reference signal in the locked state.

First, the PLL should oscillate at 4.596315885 GHz with at least 0.5 mHz frequency tuning resolution to search the center frequency of CPT resonance signal. This requirement eliminates the possibility of a dgital PLL. The reason is twofold: the digital PLL is difficult to achieve 0.5 mHz frequency resolution since in most cases a varactor based small capacitor bank is used for fine resolution with DSM dithering technique. The linearity of such capacitor bank is typically bad and the layout area is kind large; High freuency DSM dithering technique for further improving the frequency resolution demands huge power consumption. The frequency resolution of DSM based fractional-N PLL is determined as:

$$f_{\text{res}} = \frac{1}{2^N} \cdot f_{\text{ref}} \tag{3.6}$$

where N represents the number of bits in the DSM accumulator, f_{ref} represents the input reference frequency. 10 MHz crystal oscillator is used here for the reference signal of the

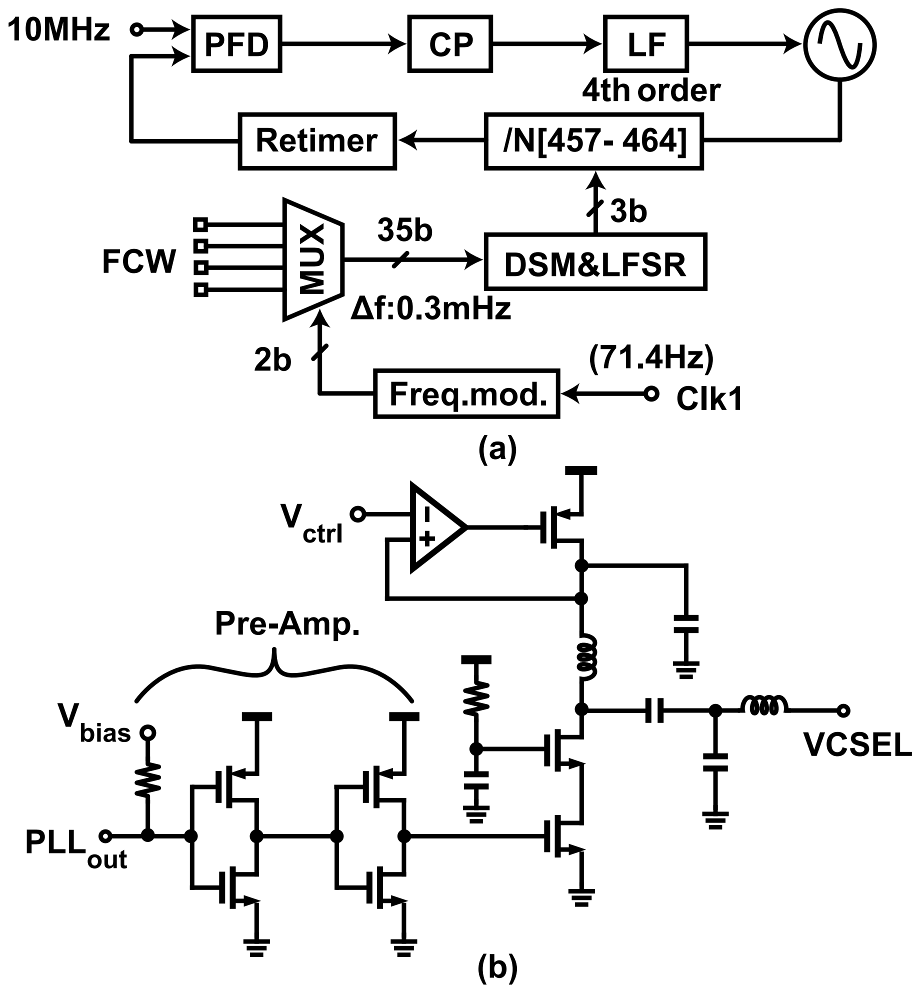

Figure 3.15: (a) Fractional-N PLL schematic diagram. (b) Power amplifier (PA) schematic.

PLL. Simple calculation indicates a 35bit DSM is needed to ensure the fine frequency resolution, which sets a power consumption limitation. A hardware reduced DSM architecture should be adopted for the low power consumption target [7]. One two-stage bus-splitting DSM is shown in Fig. 3.16. The N-bit input can be written as:

$$X = X_{\mathrm{MSB}} \cdot 2^{N_{\mathrm{MSB}}} + X_{\mathrm{LSB}} \tag{3.7}$$

where X_{MSB} and X_{LSB} correspond to the MSBs and LSBs respectively, and the total number of bits is equal to $n = N_{\mathrm{MSB}} + N_{\mathrm{LSB}}$. The output of the bus-splitting 1-3 DSM can be expressed in the Z-domain as:

$$Y_{13}(z) = \frac{X(z)}{2^N} + \frac{(1 - z^{-1})\varepsilon_{\mathrm{Q1}}(z)}{2^{N_{\mathrm{LSB}}} \cdot 2^{N_{\mathrm{MSB}}}} + \frac{(1 - z^{-1})E_{13}(z)}{2^{N_{\mathrm{MSB}}}} \tag{3.8}$$

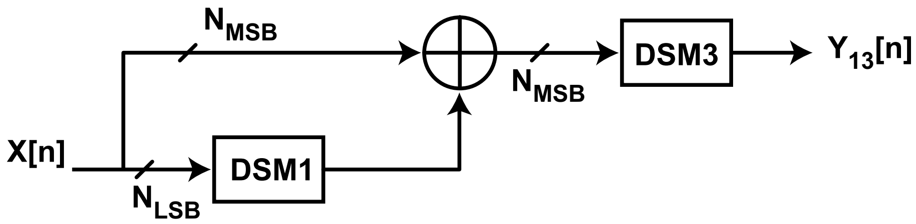

Figure 3.16: Block diagram for bus-splitting 1-3 DSM [7].

where $\varepsilon_{\mathrm{Q1}}(z)$ and $E_{13}(z)$ are the quantization errors of DSM1 and DSM3 in Fig. 3.16.

However, compared with commonly used MASH 1-1-1 structure, the bus-splitting DSM has some intermediate quantization error, like $\varepsilon_{\mathrm{Q1}}(z)$. Fortunately, as the above transfer function shows, the extra quantization errors are scaled by some factors. In order to hide such extra quantization noise below the main quantization, there are some limitations on the choices of number of bits for N_{MSB} andN_{LSB} [7]. Compared with MASH structure, the hardward reduced structure could save 20% digital standard cell, which also means 20% power consumption reduction.

Besides, the low reference frequency makes the sharped noise of DSM appear in the lower frequency region, which is also difficult to be filtered by the loop filter. Thus, the pll will display a noise peaking in the lower offset frequency region caused by the shaped DSM noise. However, the phase noise at the harmonics of the modulation frequency f_{m} of the oscillator is important for the short-term stability. The phase noise at the even harmonics of the modulation frequency degrades the resolution for locking a probe signal to a resonance. The limits to short-term fractional frequency stability due to PM noise at even harmonics of the modulation frequency in a quasi-static approximation are given by [111–114]:

$$\sigma_{\mathrm{PN}}(\tau) = \sqrt{\sum_{\mathrm{n}=1}^{\infty} C_{2\mathrm{n}}^{2} S_{\phi}(2nf_{\mathrm{m}})\tau^{-1/2}} \tag{3.9}$$

where C_{2n} is the coefficient of the $2n^{\mathrm{th}}$ harmonic of f_{m}, and S_{ϕ} is the oscillator phase noise.

From Eq. 3.9, a large f_{m} would appear to result in better short-term stability because, at a large offset frequency, the phase noise improves for a typical frequency synthesizer. However, this is not true because the coefficient C_{2n} is also proportional to f_{m}, which is

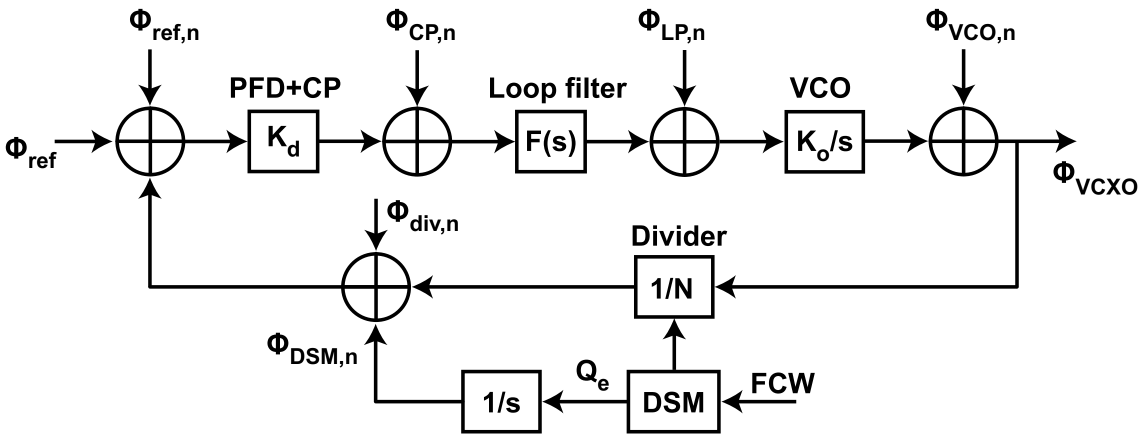

Figure 3.17: Phase noise model of fractional-N PLL.

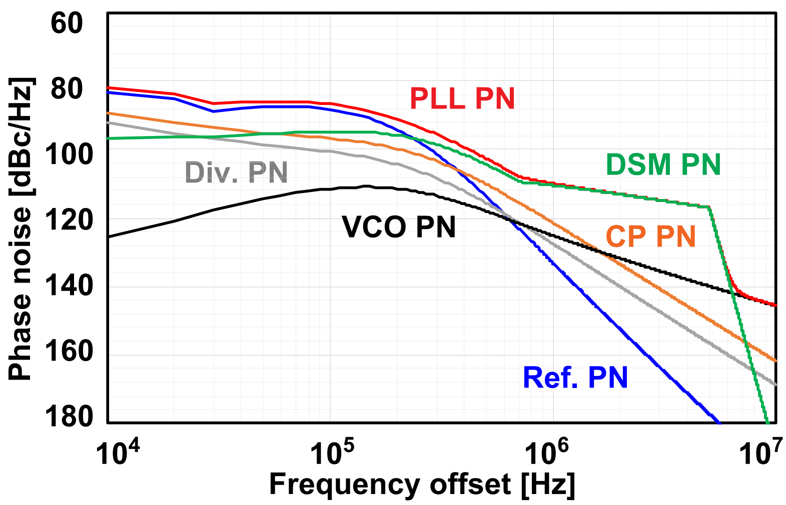

Figure 3.18: Phase noise analysis of fractional-N PLL.

given as follows:

$$C_{2n} = \frac{2n}{(2n-1)(2n+1)} \frac{f_{\mathrm{m}}}{f_{\mathrm{CPT}}} \tag{3.10}$$

In the present study, $f_{\mathrm{m}} = 71.4\,\mathrm{Hz}$ is selected to be an optimum value. Based on the theoretical calculation and experimental data, the phase noise of the RF signal must be lower than -50 dBc/Hz at an offset frequency of $2 \times f_{\mathrm{m}}$ for an over-all short-term stability better than 10^{-10} [115, 116]. The f_{m} value is also 10 times smaller than the dc current modulation frequency in order to avoid the cross-talk issue.

The phase noise model of fractional-N PLL is shown in Fig. 3.17. The open loop transfer function of PLL can be derived as:

$$G(s) = K_\mathrm{d} \cdot F(s) \cdot \frac{K_0}{s}\frac{1}{N} \tag{3.11}$$

The noise transfer fucntions of each major noise contributor in the PLL can be expressed by:

$$NTF_{\mathrm{ref,n/div,n/DSM,n}} = \frac{N \cdot G(s)}{1 + G(s)} \tag{3.12}$$

$$NTF_{\mathrm{CP,n}} = \frac{N \cdot G(s)}{K_\mathrm{d}(1 + G(s))} \tag{3.13}$$

$$NTF_{\mathrm{LP,n}} = \frac{N}{K_\mathrm{d}F(s)}\frac{G(s)}{1 + G(s)} \tag{3.14}$$

$$NTF_{\mathrm{VCO,n}} = \frac{1}{1 + G(s)} \tag{3.15}$$

From the noise transfer functions, it is easy to see that the reference noise, divider noise and DSM noise are loop-pass filtered. Thus, the in-band phase noise and spur of PLL are mainly determined by noise coming from the VCXO reference, fractional-N divider and DSM due to the low reference frequency of 10 MHz. The phase noise analysis of the integer-N PLL is shown in Fig. 3.18. Ths, in system-level, a narrow loop bandwidth is designed to suppress the noise contribution from the VCXO reference. A third-order bus-splitting DSM is adopted in order to improve the randomness, which helps the noise shaping. However, higher order DSM will casue noise peaking for the relative low in-band range since the DSM clock reference frequency (here same as the reference frequency) is low. A fourth-order loop filter is thus carefully designed to suppress the noise from the DSM, while maintain the loop stability. A retimer after the fractional-N divider suppresses the jitter accumulation in the long divider chain. A fourth-order loop filter is used to suppress the high out-band phase noise caused by the third-order DSM noise shaping. Since the CPT resonance signal is only a few kilohertz, a frequency resolution of 0.3 mHz is realized with a 35-bit DSM in order to search the peak of the resonance signal. Four FCW inputs are designed for both the calibration of different prototypes and frequency modulation.

Similar to the DSM noise, the fractional spur caused by the limited period of the DSM and nonlinearity of loop needs to be addressed as well. In the DSM part, a built-in linear-feedback shift register (LFSR) is adopted to further increase the period of the DSM

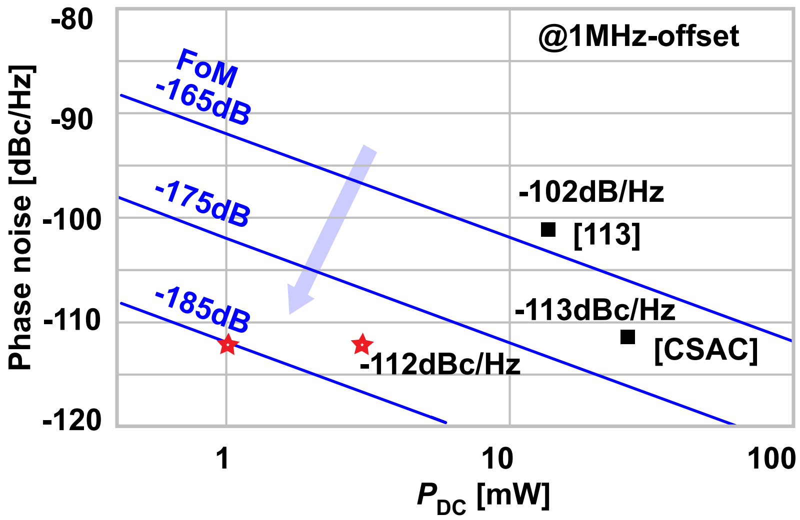

Figure 3.19: The figure of merit (FoM) of VCOs used in compact atomic clock with design targets of this work.

output. The different path delay time of divider for different divider ratio is compensated by inserted additional buffer, while helps to improve the linearity of the divider itself. The outputs signal of PFD, named as Up and Down, are used to switch on and off of PMOS and NMOS switches in the CP, respectively. However, one inverter should be added for the Up signal to enable the PMOS. Thus, a path delay mismatch exists for the Up path and Down path. The delay mismatch is simulated together with the PMOS and NMOS switches in the CP since the turning on time for PMOS and NMOS is also different, which then is compensated by manually designed buffer. Besides, the clock feedthrough, charge shaping and current mismatch of CP are addressed with various circuit techniqes [117].

For the VCO design, power consumption and phase noise are the two major aspects. The figure of merit (FoM) is typically adopted to evaluate the performance of the VCO, normalizing the phase noise, oscillation frequency and power consumption. Two prior arts of VCOs used in compact atomic clock are listed in Fig. 3.19. Ref [118] reduced more than half of power consumption compared with the VCO used in CSAC. But the phase noise degraded more than 10 dB. Our initial target was to maintain a similar phase noise as the VCO used in CSAC, while reducing the power consumption to 5 mW. For the following target, we further aimed to reduce the power consumption below 1 mW. In order to design a high-performance CMOS oscillator, we have to first review the basic design rules for the common VCO architectures. Typically there are two design regions for a VCO design, as shown in Fig. 3.20. The FoM is first limited by the current, in which region you can improve the FoM by increasing the biasing current. However, when

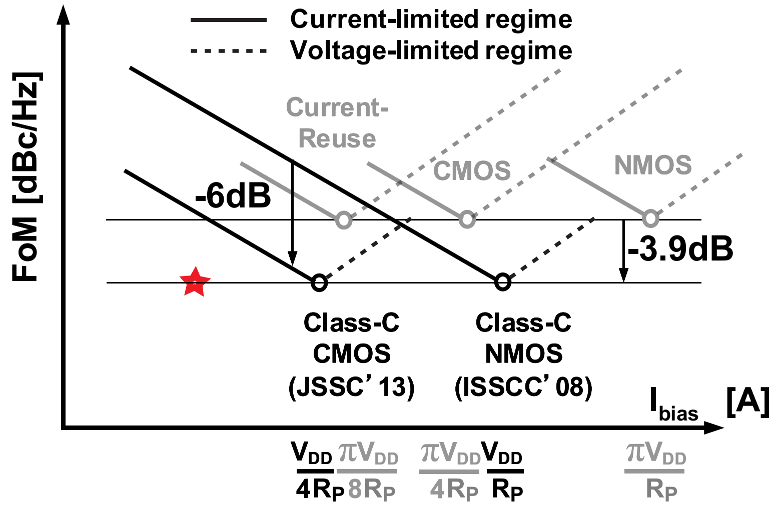

Figure 3.20: Basic design rules for common VCO architectures.

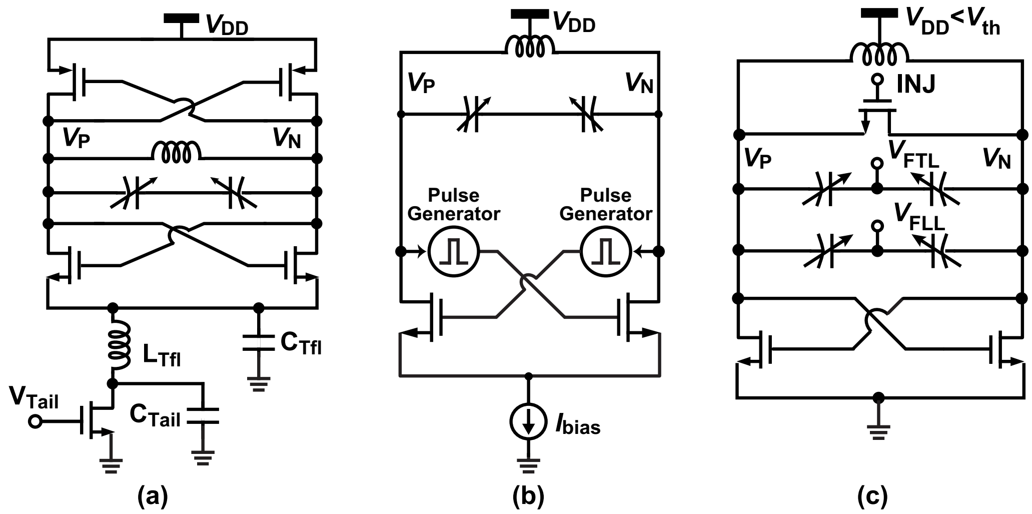

Figure 3.21: VCO designed in this work: (a) tail filter CMOS VCO, (b) pulse VCO and (c) class-D VCO.

you enter into the voltage limited region, even you increase the biasing current, the phase noise won't improve anymore. As a result, the FoM degrades. The NMOS VCO is the most common type oscillator due to its simple architecture. The CMOS VCO is more power-efficient compared with NMOS since the current is reused in the top cross-coupled PMOS pair. The class-C oscillator can further improve the power efficiency by reducing the conducting angle of the cross-couple transistors. However, there is a design trade-off between the robust start-up and phase noise for the Class-C VCO, as will be explained in Chapter 5.

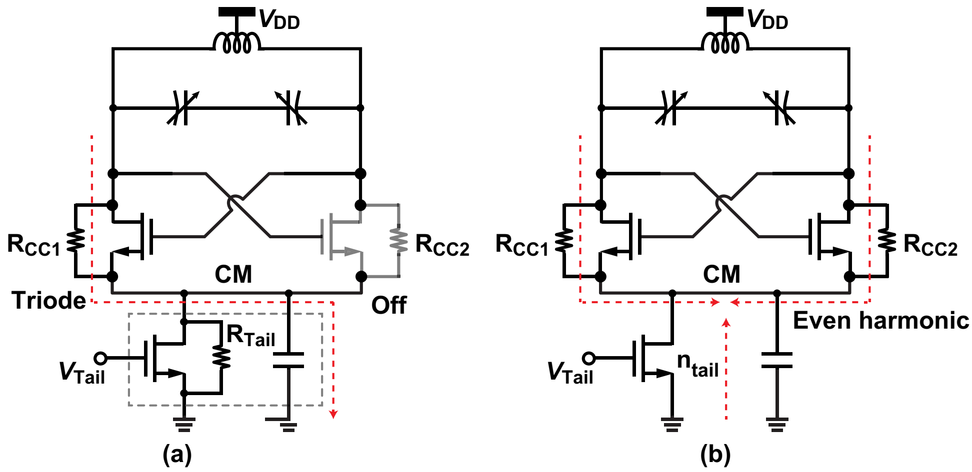

Figure 3.22: Illustrations of (a) loading effect and (b) tail noise mixing using NMOS VCO.

Three different architectures of VCO have been designed in this work to meet the low power and phase noise requirement of the atomic clock, as shown in Fig. 3.21. For power consumption, one push-and-pull VCO is first designed. The power efficiency is improved by the current reuse of the top cross-coupled PMOS pair, while the phase noise is maintained by mitigating the loading effect and tail noise mixing using a tail filter [119]. The large amplitude of VCO required to lower down the phase noise binds the operating region of the cross-coupled transistors within the off and triode region. When one transistor is turned off, the other transistor is in the triode state, which can be modeled as an ideal transistor with a relatively low impedance R_{CC1} or R_{CC2} as shown in Fig. 3.22.

The loading effect can be analyzed by using Fig. 3.22 (a). The tail transistor can be modeled as an ideal transistor with an impedance R_{Tail}. A large value capacitor is typically adopted filtering the noise of the tail transistor. The oscillation frequency at the common point is twice the oscillation frequency. By this configuration, the equivalent impedance of the transistor and capacitor R_{equiv} is also small at the second harmonic oscillation frequency, which means a low impedance path exists from the tank to ground through the common point. As a result, both the tank amplitude and qualify factor are severely degraded due to this low impedance path. Both factors affected the phase noise considerably [119].

The tail noise mixing mechanism can be understood by Fig. 3.22 (b). The switching action of the cross-coupled transistors commutates the noise in the tail currents like a single-balanced mixer. The tank current due to the switch operation of the cross-coupled transistor can be expressed by:

$$I_{\mathrm{ds}}(\phi) = \begin{cases} \beta\left(V_{\mathrm{DD}} - V_{\mathrm{th}} - \frac{V_{\mathrm{ds}}(\phi)}{2}\right), & -\Phi < \phi < \Phi \\ 0, & \phi < -\Phi, \Phi < \phi \end{cases} \tag{3.16}$$

where ϕ is the conduction angle of the cross-coupled transistors. The DC component of the MOS current must be equal to the tail bias current I_{bias} over one oscillation period:

$$I_{\mathrm{bias}} = \frac{1}{2\pi}\int_{-\Phi}^{\Phi} I_{\mathrm{ds}}(\phi)\mathrm{d}\phi \tag{3.17}$$

Using Eqs. (3.16) and (3.17) and Fourier's theory, we notice that the tank current can be decomposed into odd and even harmonics as the fundamental harmonic can be calculated by:

$$I_{\mathrm{bias}} = \frac{1}{2\pi}\int_{-\Phi}^{\Phi} I_{\mathrm{ds}}(\phi)\cos(\phi)\mathrm{d}\phi \tag{3.18}$$

The odd harmonics circulate the differential path in the tank, and don't flow through the tail transistor. However, the even harmonics flow through the common mode path in the VCO and flow through the tail transistor. Thus, the tail noise is upconverted or downconverted by these even harmonics to around fundamental frequency. Assuming a noise with modulating frequency ω_{m} is injected into the tank, the tank voltage output can be calculated by:

$$v_{\mathrm{out}} = V_0 \sin\omega_0 t + A\sin(\omega_0 - \omega_{\mathrm{m}})t + B\cos(\omega_0 - \omega_{\mathrm{m}})t + C\sin(\omega_0 + \omega_{\mathrm{m}})t + D\cos(\omega_0 + \omega_{\mathrm{m}})t \tag{3.19}$$

We notice that the tail current noise originating from low ω_{m} and $\omega_{\mathrm{m}} + 2\omega_0$ are the most problematic since the conversion gain of a balanced mixer drops rapidaly for higher harmonics. The low frequency current noise is upconverted to around fundamental frequency, while the second frequency current noise is downconverted to around fundamental frequency. According to [120], the upconverted noise only contributes the AM noise for $A = C$ and $B = -D$, while the downconverted noise is decomposed into half AM and half PM noise for $A = -C$ and $B = D \approx 0$. Since one of the cross-coupled transistors is in the triode region, the noise related with the tail transistor mixes with the tank through this low impedance path. We also notice that the AM noise can be problematic through AM-PM conversion by the varactor in the VCO tank.

A high impedance is required at the second harmonic at the common point preventing

Table 3.3: The general comparison of three VCO architectures designed in this work.

	Tail-filter CMOS VCO	Pulse VCO	Class-D VCO
Power efficiency	✓	✓✓	✓✓
Phase noise	✓	✓✓	✓
Issues	FET noise	Pulse Gen.	Supply pushing

Table 3.4: The performance comparison of three VCO architectures designed in this work.

	Frequency range (nm)	Phase noise @1 MHz (dBc/Hz)	Power (mW)	FoM (dBc/Hz)
Tail filter CMOS VCO	4.4 4.9	-116	0.65	-191
Pulse VCO	4.5-5.2	-120	1.35	-191
Class-D VCO	2.2-2.5	-110	0.12	-188

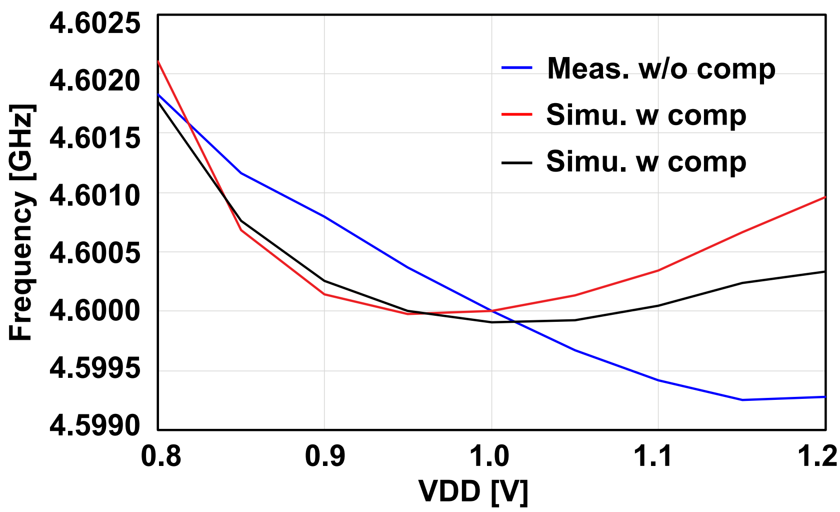

Figure 3.23: Frequency compensation by using one additional varactor in the VCO tank.

the formation of the low impedance path from above discussion. The tail filter technique creates a high impedance path preventing the loading effect and the tail transistor noise mixing. By doing so, the VCO removes additional noise contributors, improving the phase noise performance.

In this design, one additional varactor is inserted in the VCO tank to compensate for

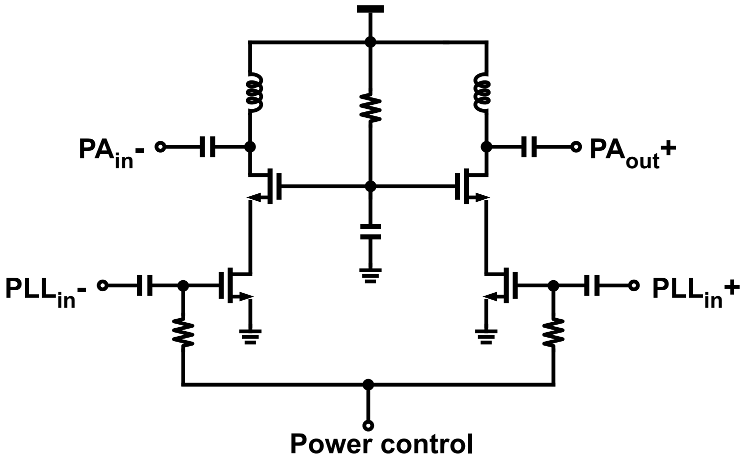

Figure 3.24: VCSEL buffer used in [8].

the frequency shift caused by the power supply noise. One node of the varactor is connected to the VDD supply line to sense the supply noise, while the other node is biased to a fixed voltage depending on the K_{VDD} with some design margin. The simulation result is shown as the black line in Fig. 3.23. Without the frequency compensation, the K_{VDD} is 6.98 MHz/V around 1 V supply voltage range, while in case of compensation it is quite flat around 0.95 V supply voltage. In order to further improve the power efficiency, one pulse VCO and class-D VCO have also been designed [121–123], which will be introduced in Chapter 5. The pulse VCO is more robust to start-up and shows a potentially higher voltage efficiency by driving the cross-coupled transistors with a pulse waveform, compared with the conventional current efficient class-C VCO. The class-D can achieve extremely low power consumption under low supply voltage. The general comparison and performance comparison are given in Table 3.3 and Table 3.4, respectively.

For the VCSEL buffer, one prior art used in the compact atomic clock is shown in Fig. 3.24. It is a differential class-C PA, which helps to suppress the even harmonic. But it suffers from the balun loss, inferior turning resolution and low backoff power efficiency. The design history for VCSEL buffer in this work is shown in Fig. 3.25. Initially, a calss-AB two-stage PA is designed with a programmable attenuator. Then a more power efficient programmable two-stage class-C PA is adopted instead of using a programmable attenuator. The detailed circuit schematics for class-AB abd class-C PAs are shown in Fig. 3.26. In the latest version, a class-E power amplifier (PA) is designed in order to further improve power efficiency, as shown in Fig. 3.15 (b). The performance comparison of these three PAs is shown in Table 3.5.

In the class-E PA, the pre-amplifier state converts the sine-wave output from the VCO into the squre waveform for the class-E operation. The last state is a cascode amplfier s-

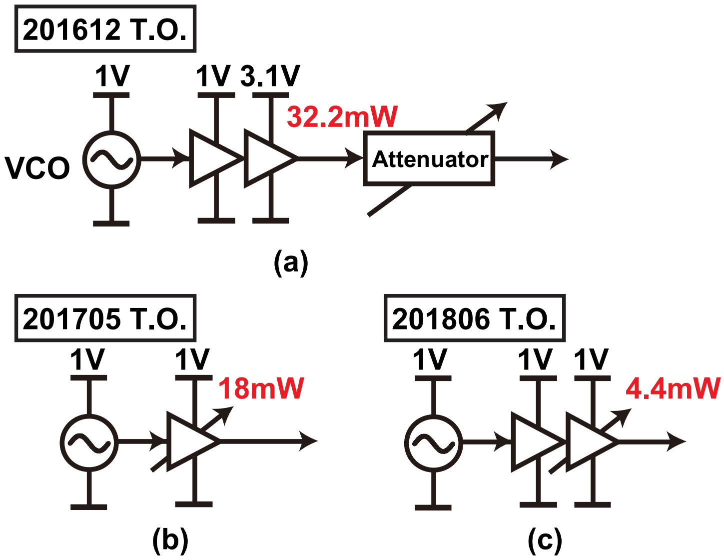

Figure 3.25: PA designed in this work: (a) class-AB two stage PA with 32.2 mW for 0 dBm output, (b) two-stage class-C PA with 18 mW for 0 dBm output and (c) class-E PA with 4.4 mW for 0 dBm output.

tate. By optimizing the match impedance, the overlapping are of V_{DS} and I_D is minimized. In an ideal case, the theoretical power efficiency can be 100%. The simulated waveforms of V_{DS} and I_D of the class-E PA are shown Fig. 3.27. When the I_D reaches the maximum point, the V_{DS} is in the minimal region, and vice versa. Thus, the transistor short timing when the I_D and V_{DS} are both high is minimized, which reduces the static power consumption and improves the output RF power efficiency. The RF power level should be carefully controlled to search for an optimum light intensity for CPT signal contrast. The amplitude of the CPT signal becomes larger as the light intensity increases until it saturates. Further increasing the light intensity results in a stronger background current of the PD, which degrades the signal contrast η_{CPT}. Also, the light intensity should be carefully controlled to minimize the line broadening. A 0.02-dB minimal step is required for the control accuracy in order to minimize the light intensity resolution. Moreover, -5 dBm to +5 dBm power range is needed in order to satisfy the typical light transfer efficiency to the first-order sideband of the VCSEL. The V_{bias} is used to bias the input stage of the pre-amplifier to make the sine input waveform from the VCO as a square waveform for the class-E operation. The V_{ctrl} is used to tune the output power by directly changing the drain voltage with an operational amplifier. This method maintains the power efficiency when the output power is low. Thus, a more consistent power efficiency is achieved when the output power is changed. Both V_{bias} and V_{ctrl} are programmable with 10-bit digital control. An on-chip match network is designed to meet both the class-E operation and

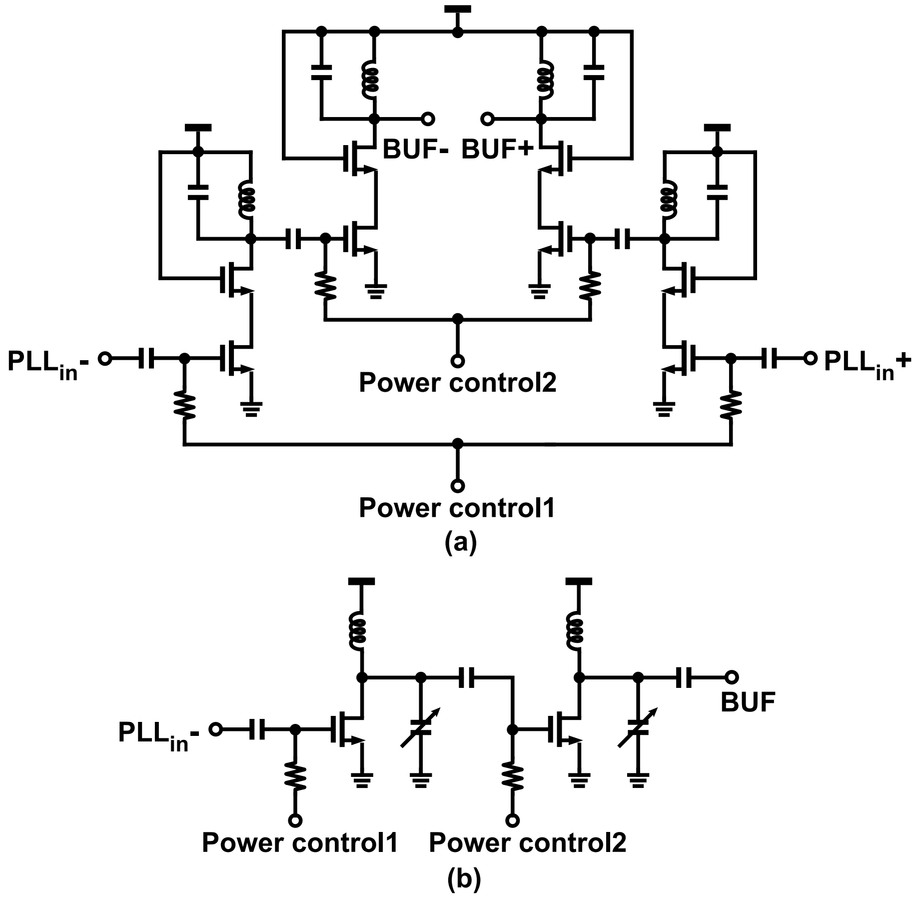

Figure 3.26: The initial two PA designs: (a) detailed circuit schematic for Class-AB, (b) detailed circuit schematic for two-stage class-C PA.

impedance matching of the VCSEL at 4.6 GHz in order to further improve the power efficiency.

The simulated clas-E PA output versus the V_{ctrl} control bit is shown in Fig. 3.28. The fundamental output is the desired one to drive the VCSEL. The power level meets the design specification with less than 0.03 dB tuning resolution to minimize the broadening effect for the CPT resonance signal. The harmonics outputs have adverse effects on the light shift. Also higher harmonics degrade the power efficiency for the fundamental output. Thus, the harmonics should be suppressed by the impedance matching network. As indicated by Fig. 3.28, the second harmonic is above 30 dB lower than the fundamentl, while the third haromic is approximately 50 dB lower.

The performance summary of the RF circuits developed in this work is shown in Table 3.6. The RF loop only consumes less than 7 mW power consumption, as shown in Fig. 3.29.

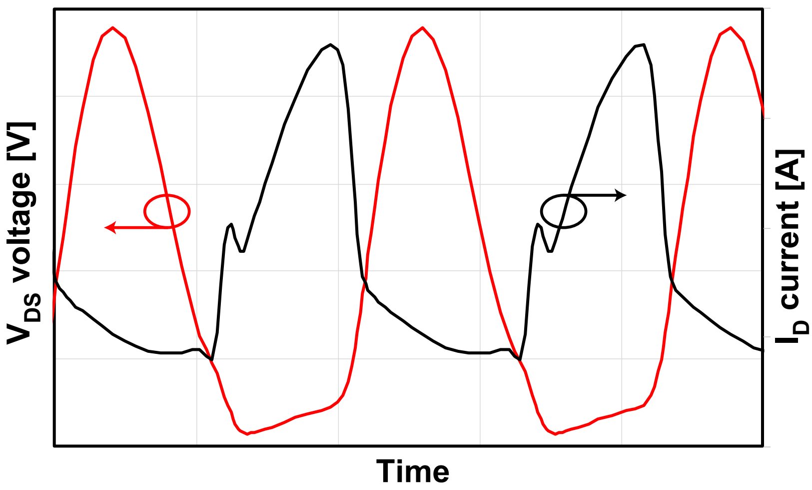

Figure 3.27: The simulated waveforms of V_{DS} and I_{D} of class-E PA.

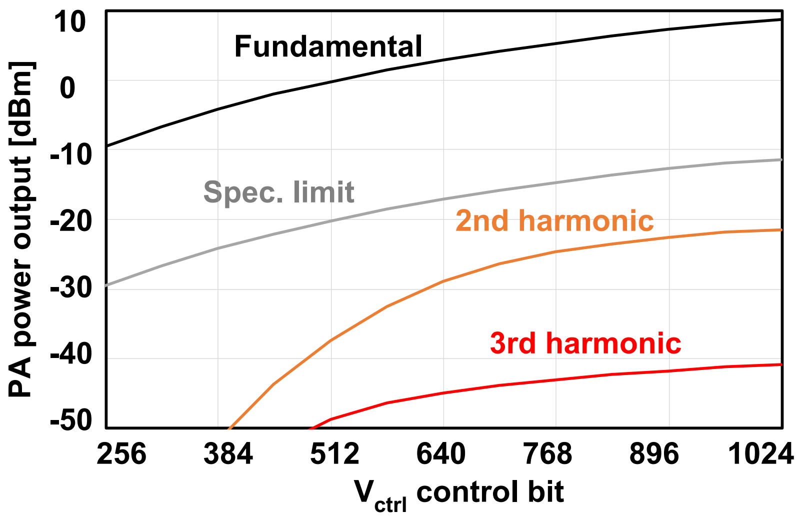

Figure 3.28: The simulated PA outputs versus the V_{ctrl} control bit.

3.3.3 Frequency output ports

Both 10-MHz and one-pulse-per-second (1-PPS) output ports are designed for general applications, as shown in Fig. 3.30. When the system is locked, both outputs will inherit the stable quantum mechanical resonance of the CPT signal.

The 10-MHz signal is both input and output from the VCXO, and the 1-PPS signal is the divided signal from the 10-MHz signal. The frequency of VCXO is used to trigger the CPT resonance in atom cell after frequency multiplication and the discriminated signal of the lock-in amplifier represents the frequency error. Such frequency error is processed in

Table 3.5: PA performance comparison.

Parameter	Class-E PA	[8]	[118]
Frequency	4.6 GHz	3.4 GHz	4.6 GHz
Topology	Class-E	Class-C	Class-E
Matching network	On-chip	Off-chip	Off-chip
Power consumption	4.4 mW@0 dBm	18.1 mW@0 dBm	15 mW@0 dBm
Tuning range	-5 to 5 dBm	0 to 10 dBm	-10 to 0 dBm
Tuning resolution	0.02 dB	N/A	N/A

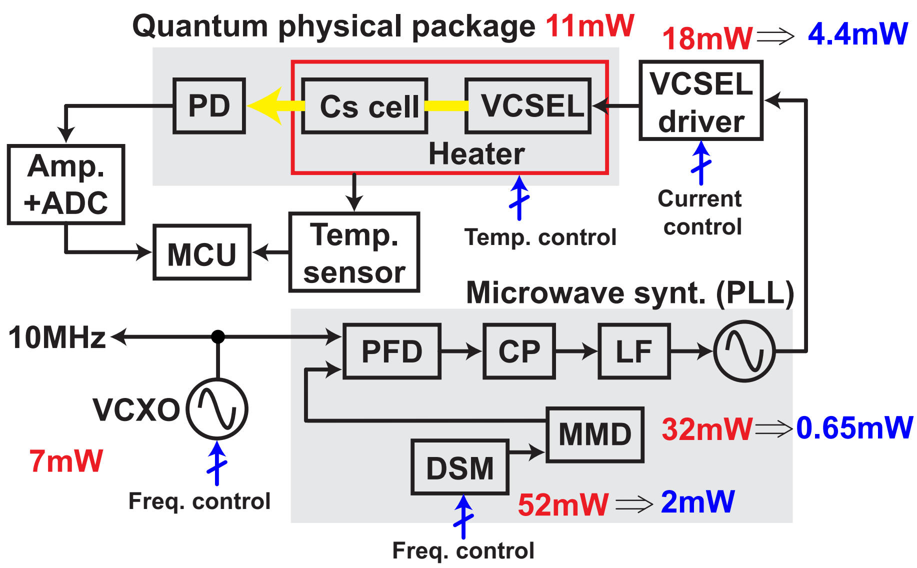

Figure 3.29: Power reduction of RF loop.

the MUC and used to control and correct VCXO frequency by a DAC. Thus, within one feedback loop, the frequency of VCXO is synchronized or referenced to the atomic CPT resonance signal. The phase of the 1-PPS signal can be synchronized with the GPS_{ref} signal, whenever the signal is available, using a time-to-digital converter (TDC). The resolution of the TDC is set by 4.6 GHz/4 from the PLL with 32 bits in order to cover a one-second dynamic range. Thus, the calibration timing accuracy is 1 ns, which is similar to the timing accuracy of the general-purpose GPS receiver. The duty cycle of the 1-PPS signal is programmable from 10% to 90% in 10% steps. All circuits except for the VCXO are digitally synthesized with a power consumption of only 2.2 mW when in full

Table 3.6: The performance summary of RF circuits.

	201705 T.O.	201712 T.O.	201806 T.O.
VCO	1.35 mW	1 mW	0.65 mW
PLL	4 mW	2.8 mW	2 mW
VCSEL buffer	33 mW@4 dBm 32.81 mW@0 dBm 32.65 mW@-5 dBm	30 mW@4 dBm 18 mW@0 dBm 12 mW@-5 dBm	6.9 mW@5 dBm 4.4 mW@0 dBm 3 mW@-5 dBm

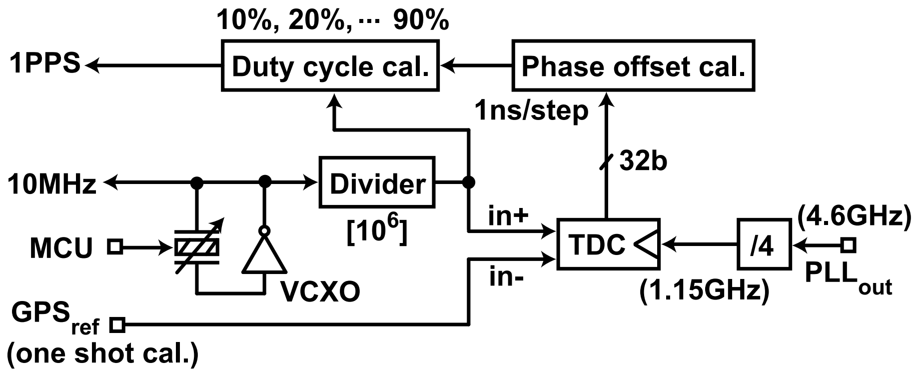

Figure 3.30: Output ports circuit block.

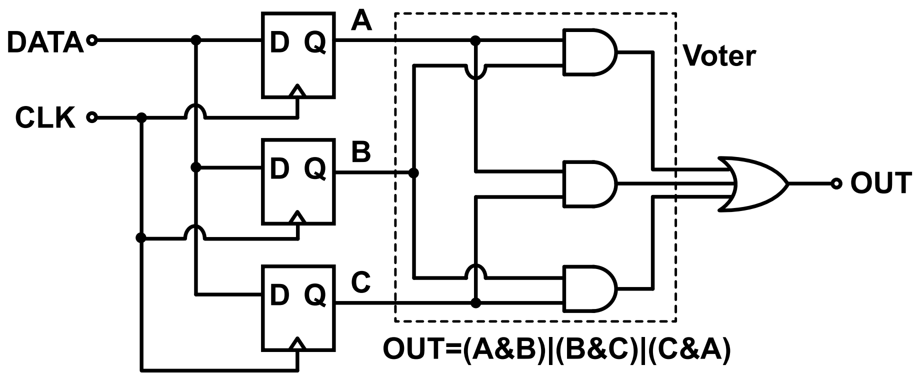

Figure 3.31: Triple-modular-redundant (TMR) DFF structure.

operation.

3.3.4 Soft-error tolerant design

The harsh environment faced by the devices deployed in the LEO requires the circuits of the ULPAC to be radiation tolerant [124–129]. The quick charge and recharge operation of RF circuit resembles a system-level reset operation of digital circuit, which effectively reduces the single-event upset (SEU). Besides, large capacitance nodes in the analog circuit typically form a low pass filter for the single-event transient (SET). However, the digital circuits are susceptible to such soft-errors [130, 131]. Redundant coding functions are designed for the fully synthesized digital circuits in the chip, which maintain functionality even one path fails to operate correctly. Manually designed triple-modular-redundant (TMR) DFFs, as shown in Fig. 3.31, are applied to the divider and the phase frequency detector (PFD) in the PLL in order to improve the robustness. If one DFF value is inverted due to radiation, the output can still obtain an accurate value from other DFFs by the voter. Moreover, if multiple-cell upset (MU) occurs, the event probability is given by [132]:

$$K_{\mathrm{MU}} \approx \frac{\Pr\{\mathrm{MU}\}}{\Pr\{\mathrm{SEU}\}} \cong 0.105 \times d^{-1.67} \tag{3.20}$$

where d is the distance between the DFFs, Pr{MU} is the probability of a MU, and Pr{SEU} is the probability of an SEU. By setting the distance between DFFs to be 60 μm, the soft error rate (SER) of the DFF is reduced to approximately 1/7000. Circuits using an silicon on insulator (SOI) technology are under development, which could further enhance the reliability against radiation [133, 134].

Chapter 4

Prototype and Evaluation

The quantum physical package is integrated with the frequency probing and locking circuits together with additional control circuits on the same printed circuit board (PCB). Figure 4.1 shows the pictures of the prototypes developed in our group. The volume of ULPAC is keeping reducing. The latest prototype of ULPAC is shown in Fig. 4.2. The size of this prototype is only 15.4 cm^3 including magnetic shield package.

4.1 Quantum Physical Package Characterization

For the power consumption, the heater only consumes 9.1 mW to heat the atom cell around 80 $^\circ C$, thanks to the small size of atom cell, highly thermal isolation and hermetic design. The measurement results for VCSEL output power and voltage versus current are shown in Fig. 4.3. The threshold current is only 0.5 mA, and the circuit consumes 3.1 mW for an output light power of 0.5 mW. The coil consumes less than 1 mW to produce a stable 10 μT unidirectional magnetic field for the $\langle 0-0\rangle$ CPT atomic resonance. Thus, the quantum package consumes less than 13.1 mW power consumption in total, as shown in Fig. 4.4.

The measured CPT resonance signal is shown in Fig. 4.5. The FWHM is only 1.5 kHz. The qualify factor of CPT resonance signal is defined as:

$$Q = \frac{f_{\mathrm{CPT}}}{\mathrm{FWHM}} = \frac{\frac{1}{2}\Delta_{\mathrm{hf}}}{\mathrm{FWHM}} \tag{4.1}$$

Thus, the calculated Q factor of this atomic clock is approximately 3.06×10^6.

The output of the lock-in amplifier of CPT signal is shown in Fig. 4.6. It is the discriminated signal of CPT resonance signal. As shown in Fig. 4.6, the signal amplitude of the discriminator is around 700, while the RMS noise power is 27. Thus the signal to

Figure 4.1: Packaged ULPAC prototypes.

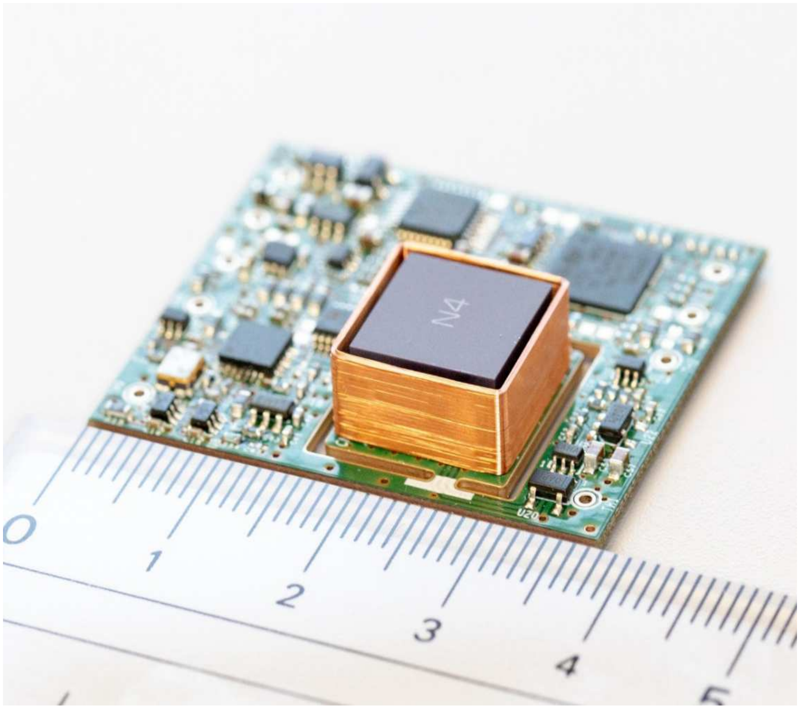

Figure 4.2: Latest ULPAC prototype.

noise ratio S/N can be calculated by:

$$S/N = \sqrt{(\frac{700^2/2}{27})} \approx 95 \tag{4.2}$$

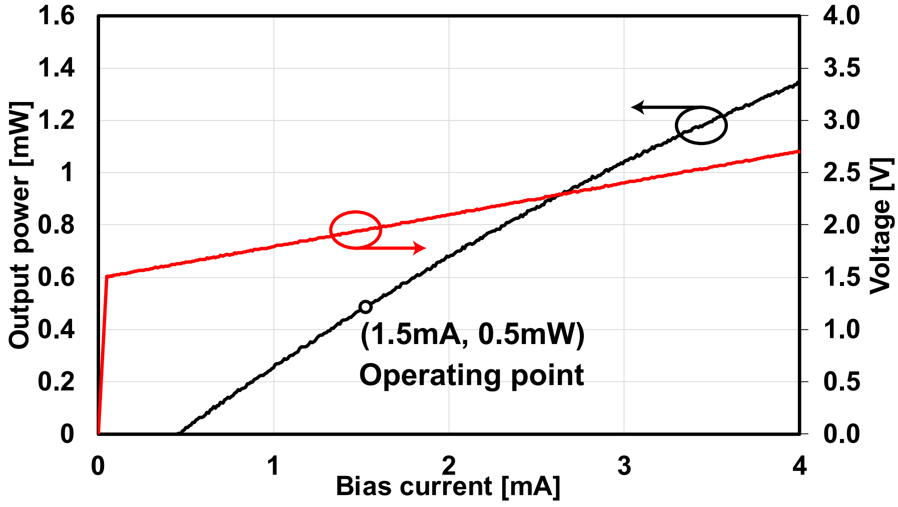

Figure 4.3: VCSEL output power and voltage versus current.

The estimated S/N ratio is approximately 95. Finally, the theoretical short-term stability can be calculated using Eq. (2.18) [53]:

$$\sigma_{\text{y\_CPT}} = \frac{0.11}{3.06 \times 10^6 \times 95} \times \frac{1}{\tau^{1/2}} \approx 3.784 \times 10^{-10} \times \tau^{-1/2} \tag{4.3}$$

where the χ in Eq. (2.18) is set to be 0.11 since the frequency of modulation and depth of modulation are much smaller than the CPT resonance linewidth in this work [87]. The spectral density of the CPT resonance signal can be calculated from the short-term Allan deviation shown in Eq. (4.3) using the relations [53]:

$$S_{\text{y\_CPT}}(f) = h_0 \tag{4.4}$$

$$\sigma^2(\tau) = \frac{1}{2}\frac{h_0}{\tau} \tag{4.5}$$

Thus, the spectral density of the CPT resonance signal is:

$$S_{\text{y\_CPT}}(f) = 2.126 \times 10^{-19} \tag{4.6}$$

where only white frequency noise is considered.

The estimated power spectral density of fractional frequency fluctuation of the quartz-crystal oscillator adopted in the ULPAC based on the measured Allan deviation is ex-

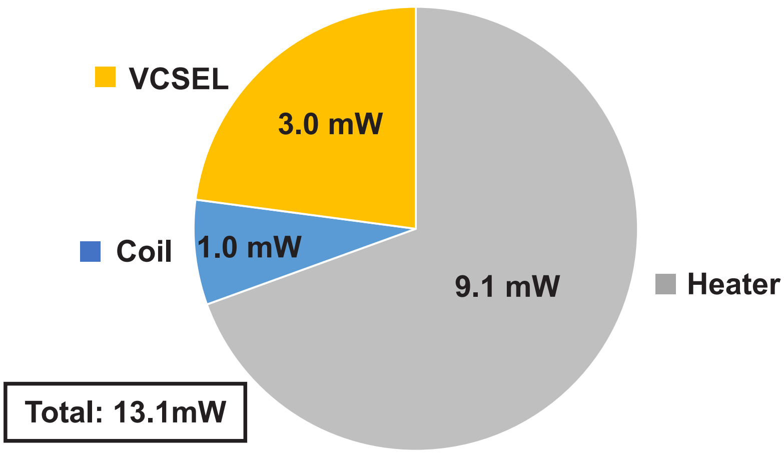

Figure 4.4: Power division of quantum package.

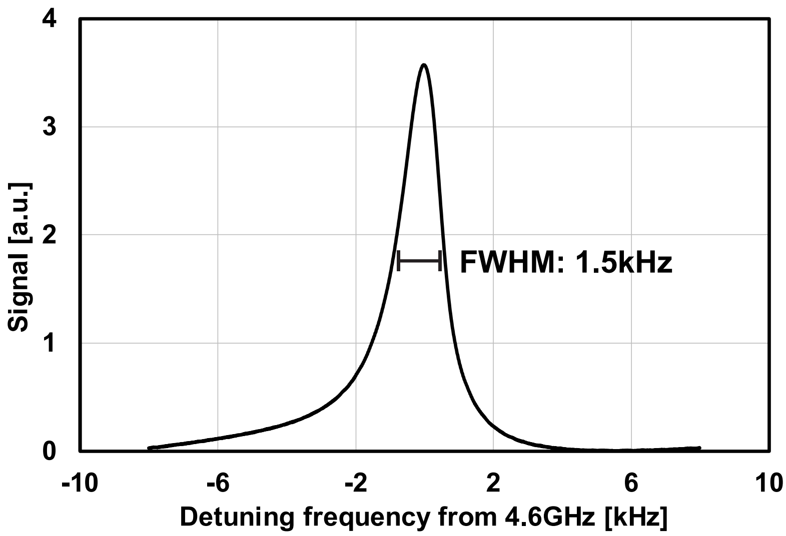

Figure 4.5: Measured CPT resonance signal.

pressed as:

$$S_{\mathrm{y\_VCXO}}(f) = 3 \times 10^{-21} \times f^{-1} + 6 \times 10^{-25} \times f^{2} \tag{4.7}$$

where the first item on the right side of Eq. (4.7) represents the flicker frequency noise, and the second item on the right side of Eq. (4.7) represents the white phase noise.

Using Eqs. (2.19), (2.21), (4.6) and (4.7), the theoretically calculated output stability $\sigma_{\mathrm{y\_out}}$ is plotted in Fig. 4.7, where the servo loop filter constants f_{n} are assumed to be 2 Hz (gray), 0.2 Hz (yellow), 0.02 Hz (blue) and 0.002 Hz (green), respectively. From E-

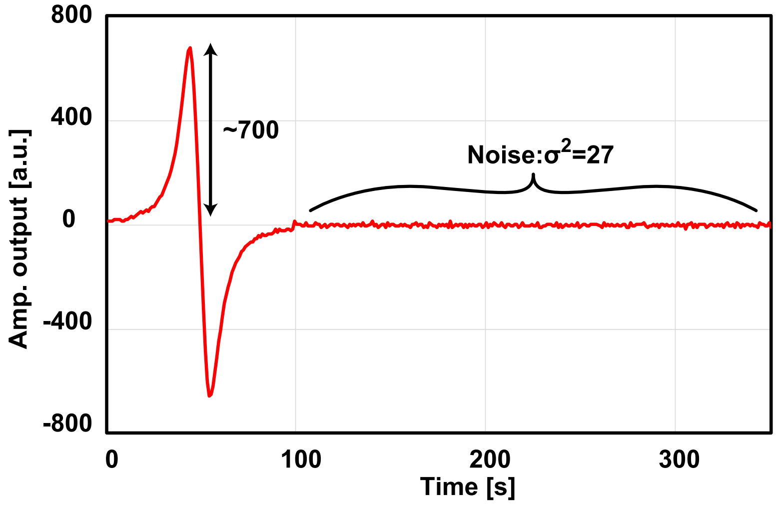

Figure 4.6: Measured output of lock-in amplifier for estimating the signal to noise ratio S/N.

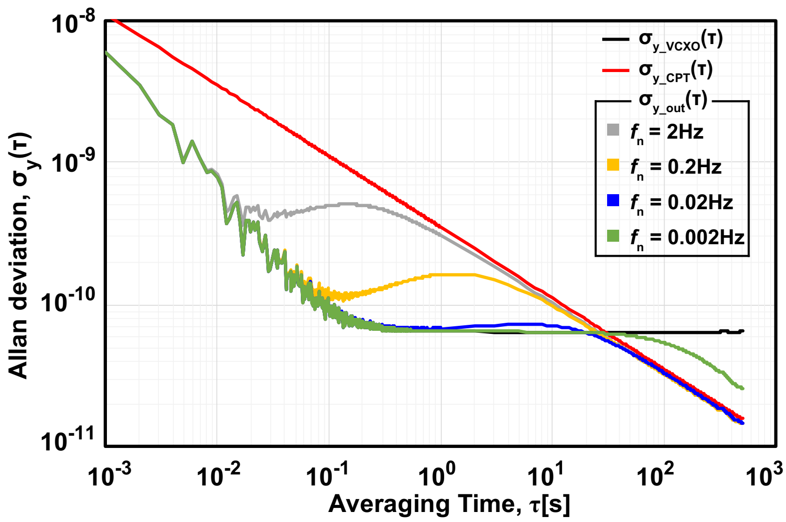

Figure 4.7: Theoretically calculated short-term stability of an atomic clock assuming f_c=1000 Hz.

qs. (2.19) and (2.21) and Fig. (4.7), it is clear that an optimal value of f_n exists, the value of which should be small enough to suppress the very short-term frequency instability contribution from the CPT resonance signal and be large enough to suppress the contribution from the crystal oscillator for the short-term averaging time. In the present study, f_n is designed to be approximately 0.02 Hz for an optimal short-term stability by adjusting the loop filter gain. The discussion on the measured Allan deviation in Section 4.4 shows that the theoretically calculated short-term stability based on the analysis in this section

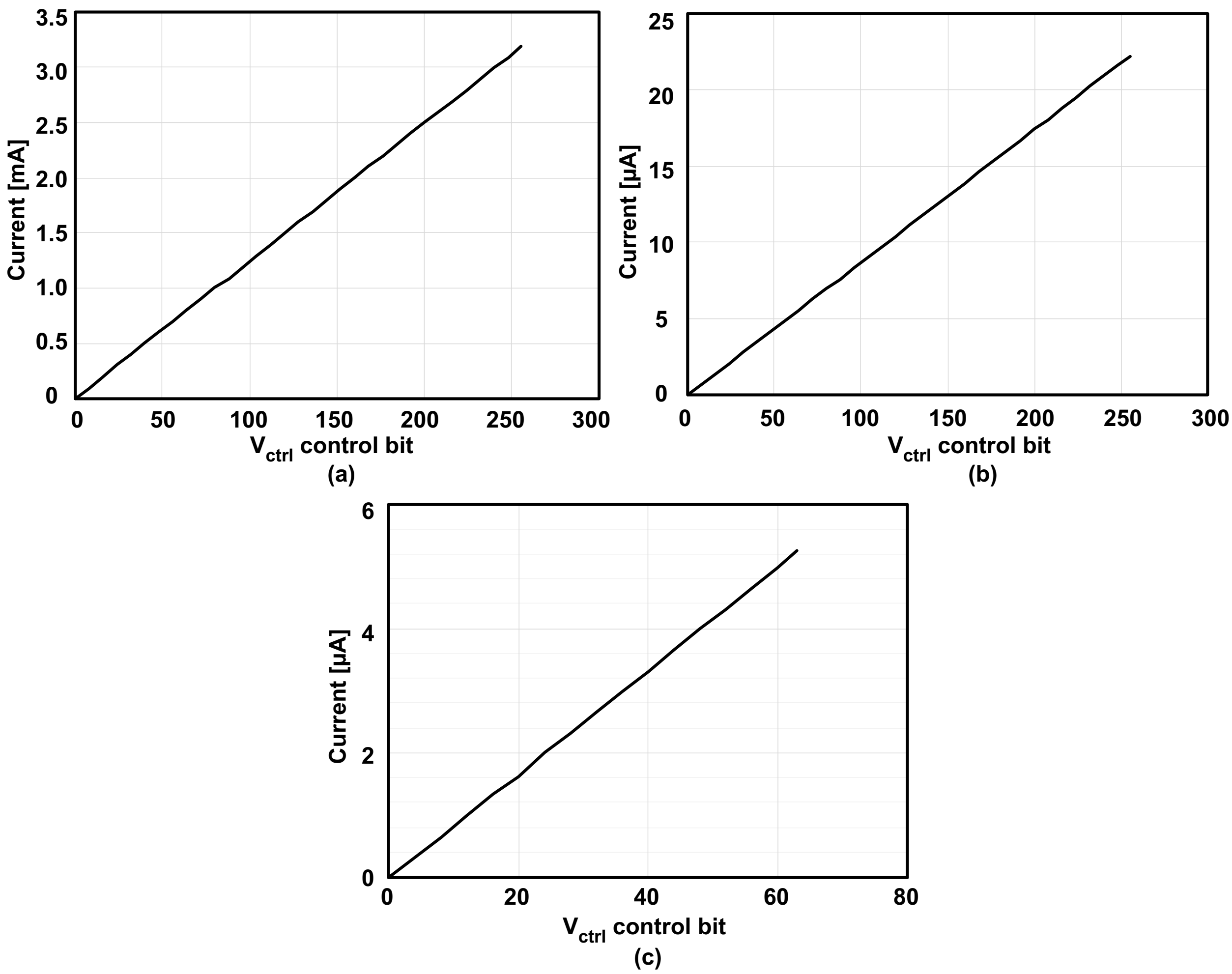

Figure 4.8: Measured output currents of (a) coarse current source, (b) fine current source bank and (c) on/off current source bank.

fits the measured data well.

4.2 Frequency Probing and Locking Circuit Performance

The measured output currents of current source banks for wavelength locking loop are shown in Fig. 4.8. It meets the design specification well. For the short-term frequency stability, the amplitude-modulated (AM) noise of the dc current source and the phase-modulated (PM) noise of frequency generator are evaluated. The dc current noise is measured using an Agilent E5270B precision IV analyzer. The sampling rate is set to be 4 Hz, and 400 samples are recorded, which corresponds to a measurement time of 100 s. The measured current noise is shown in Fig. 4.9. When the output current is maximum

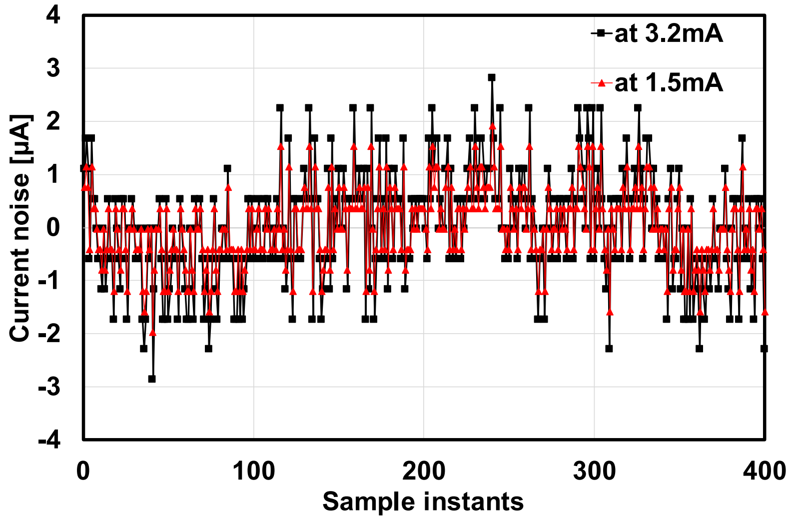

Figure 4.9: Current noise measurement result of the dc current source.

(3.2 mA), the RMS noise is 0.103 µA, which is the worst case. For the typical operating current of approximately 1.5 mA, the RMS noise is only 0.07 µA. Thus, the RMS wavelength offset caused by the dc current noise could be kept smaller than 13 MHz. Since the linewidth of VCSEL is approximately 100 MHz, this frequency offset is well hidden. Only when the wavelength offsets is greater than 100 MHz, the shape of the resonance signal will be distorted [73]. Since the minimum current step of the dc current source is 0.1 µA, the linearity of the wavelength search loop is ensured as well.

The PA output is evaluated for the PM noise of the RF signal, which includes both the noise contributors from PLL and PA. The phase noise of the RF signal is evaluated using an Agilent E5052B signal source analyzer (SSA). At a frequency of 4.596315885 GHz, the RF signal achieves a phase noise of -62 dBc/Hz at an offset frequency from the carrier of $2\times f_{\mathrm{m}}$, as shown in Fig. 4.10. This phase noise performance could ensure that the short-term stability of ULPAC is not limited by the phase noise at the frequency offset of harmonics of f_{m}. The frequency range of the PLL is from 4.4 GHz to 4.9 GHz. The 500 MHz range is achieved by one discrete 3-bit frequency selection band and one continuous-frequency tuning varactor, as shown in Fig. 4.11.

The PLL consumes only 2.0 mW from a supply voltage of 1 V and the PA output power is from -8 dBm to 5.8 dBm with a maximum power efficiency of 47.3% if the power loss of the biasing circuit is not included. The measured PA output power versus the tuning voltage control V_{bias} is shown in Fig. 4.12. In order to search the optimum light intensity for the contrast and minimize the light broadening, minimal 0.01 dB/code is achieved around 5 dBm output power.

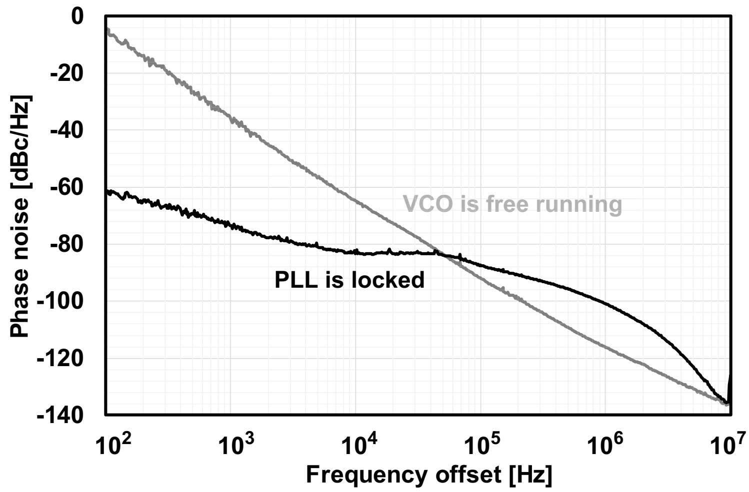

Figure 4.10: Phase noise measurement result of the RF signal when the oscillation frequency is 4.596315885 GHz.

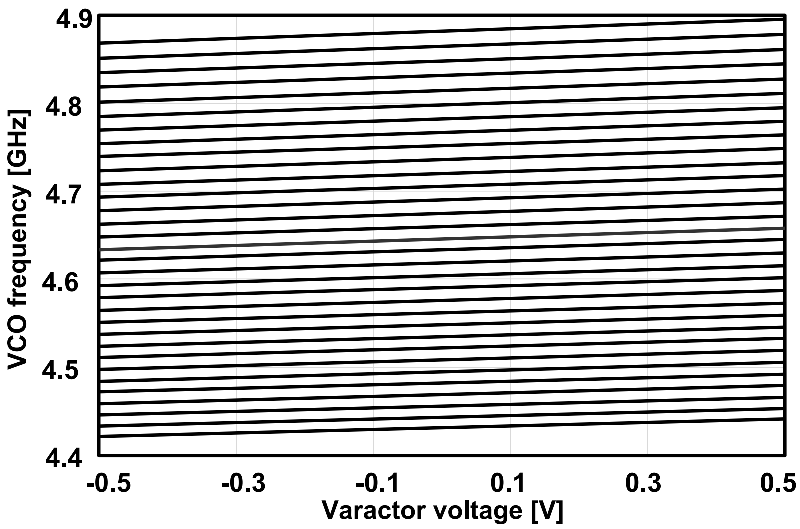

Figure 4.11: VCO output frequency when the varactor voltage and control word of frequency control bank are swept.

4.3 1-PPS Functions Verification

For general purpose applications, 1-PPS output is generated from the stabilized 10MHz output of VCXO. The 1-PPS has programmable duty cycles and GPS synchronization function with internal calibration circuits. Figure 4.13 shows the measured output of the 1-PPS signal with different duty cycle settings. The programmable duty cycle can be set from 0.1% to 99% in 0.1% step. The GPS synchronization function is also verified using

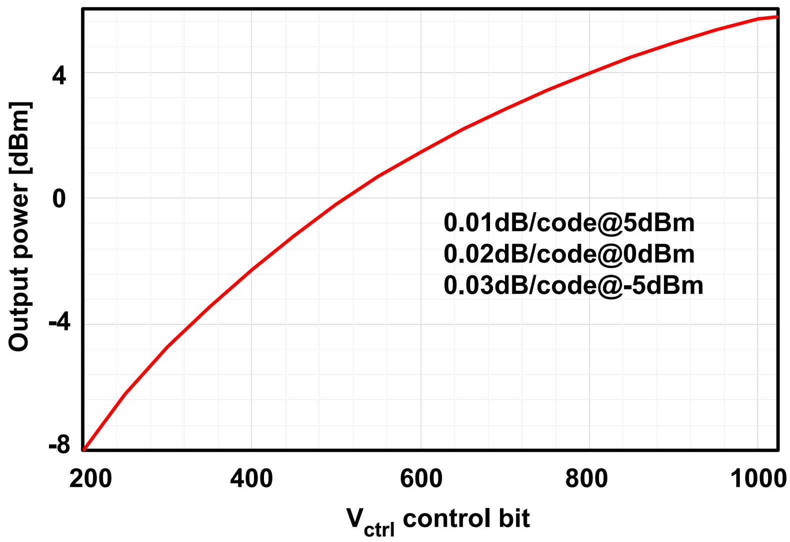

Figure 4.12: PA output power versus the tuning voltage V_{ctrl} control bit.

an external 1-PPS signal. Figure 4.14 shows the TDC reading, which indicates the phase offset between the GPS signal and the internal 1-PPS signal. The TDC circuit outputs the absolute phase difference between the internal 1-PPS signal and the external 1-PPS signal (GPS signal) with a lead & lag signal, indicating whether the GPS signal is leading or lagging the internal 1-PPS signal. From Fig. 4.14, We notice that there are some fixed offsets between the actual phase offset and the TDC output. This is caused by the timing delay and mismatch between the two signal paths, which can be manually canceled by setting an initial value of TDC.

4.4 Frequency Stability Evaluation and Discussion

As a key frequency stability indicator, the Allan deviation measurement result of ULPAC is given by Fig. 4.15. The frequency stability starts at 6.71×10^{-11} with an averaging time of one second and reaches 2.2×10^{-12} with an averaging time of 10^5 s, which is a better performance by two orders of magnitude than that of a superior TCXO. The theoretically calculated Allan deviation by Eq. (4.3) based on the white frequency noise is also shown in Fig. 4.15, using a black dash line. From $\tau = 1$ s to tens of seconds, the loop unity-gain bandwidth f_n with a value of 0.02 Hz allows the frequency stability of VCXO to be dominant for the total frequency stability. The measured Allan deviation follows the white frequency noise estimated from S/N analysis and improves when the averaging time τ is between 50 s and 5000 s. When the averaging time τ is beyond 5000 s, the measured

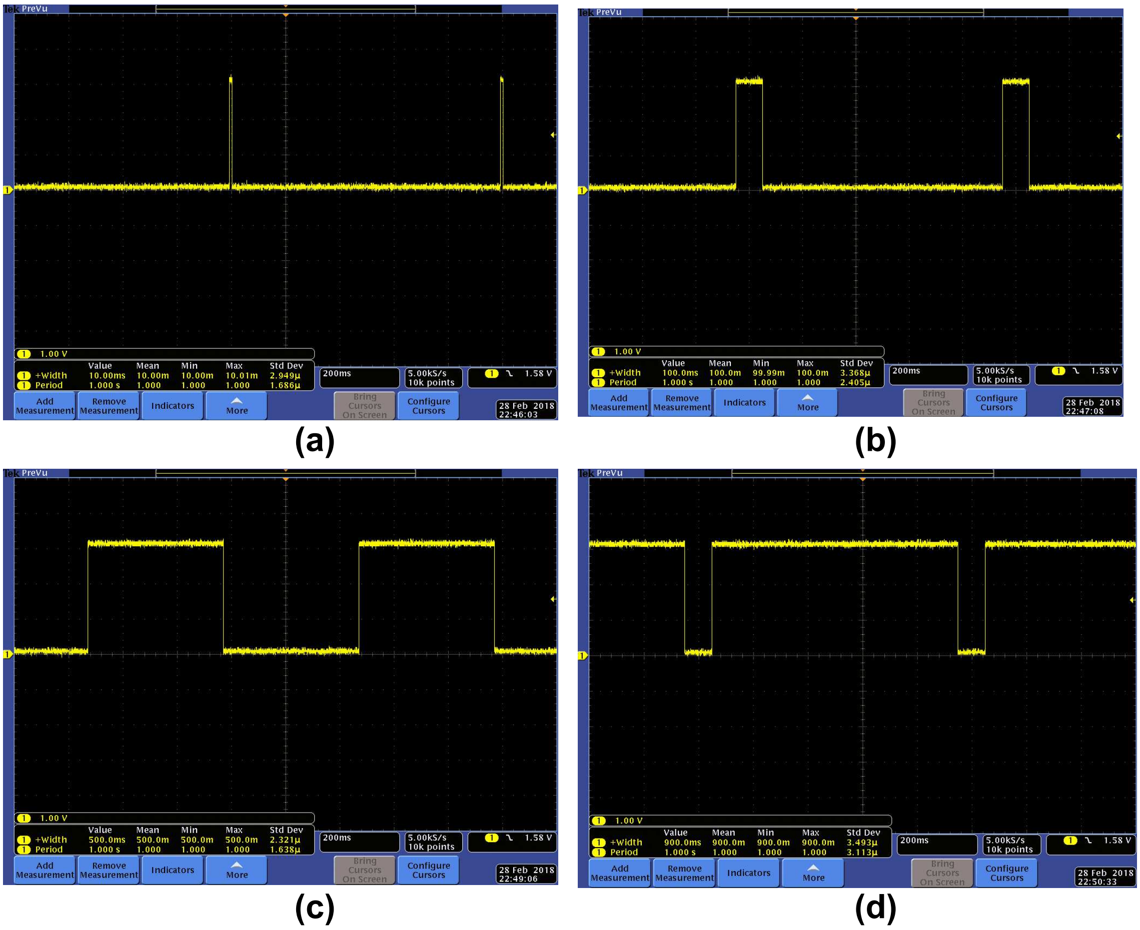

Figure 4.13: Measured 1-PPS with different duty cycles of (a) 0.1%, (b) 10%, (c) 50% and (d) 90%.

Allan deviation shifts due to the flicker noise resulting from light shift fluctuations as τ increases. Compared with the state of the art done by Microsemi [66], this work achieves a similar short-term stability below the averaging time of 10^2 s with half the power consumption. This can be attributed to the factor that the same principle, CPT, is adopted in both works. However, the CSAC of Microsemi begins to show a systematic frequency shift beyond the averaging time of 10^4 s, while the Allan deviation of this work shows an excellent performance even at averaging time in the range of 10^5 s. This is attributed to the highly accurate temperature control method (± 1 mK), optimization of the operational condition of VCSEL, and hermetic design of the physical package used in this work. In summary, for the very short-term stability (below 10 s), the stability is determined by the CPT resonance noise and loop bandwidth should be small enough to suppress the noise coming from the CPT resonance. For the short-term stability (from 10 s to 10^4 s), the stability is limited by the VCXO noise and the loop bandwidth should be large enough

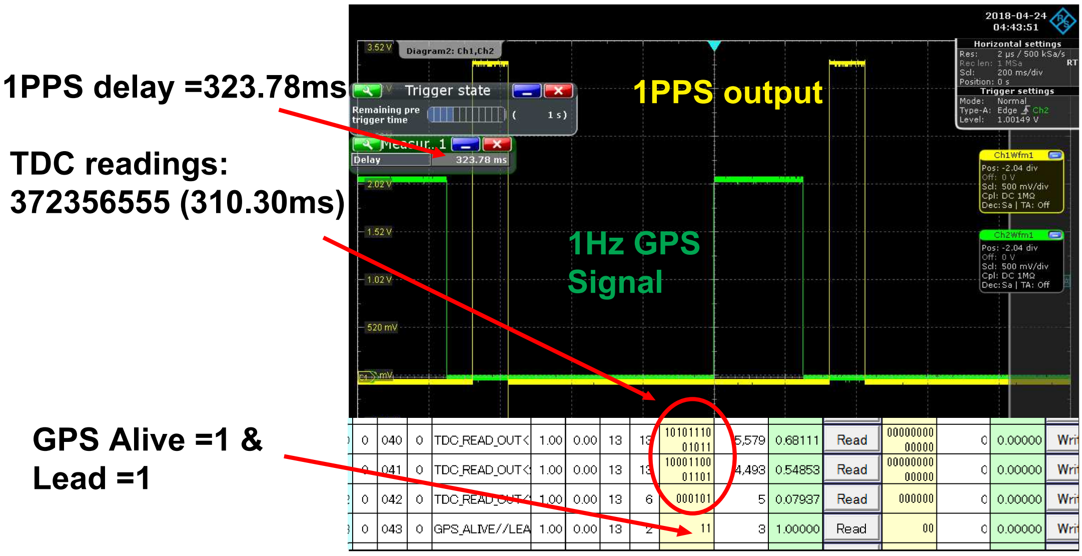

Figure 4.14: Measured TDC output of GPS synchronization function in the 1-PPS output circuit.

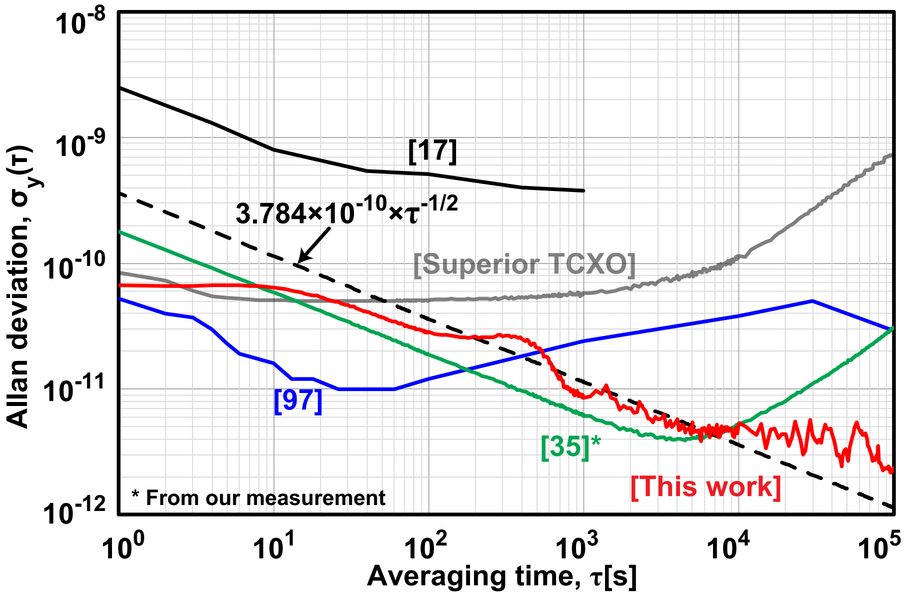

Figure 4.15: Measured Allan deviation of ULPAC and other studies.

to suppress the noise coming from the VCXO. For the long-term stability (beyond 10^5 s), the stability is mainly affected by environmental perturbations and various stable control loops should be incorporated to maintain long-term stability.

In this evaluation, the observed data during 3.2×10^5 s used for obtaining the Allan deviation plot, gives three samples of mean frequency with an averaging time of 10^5 s.

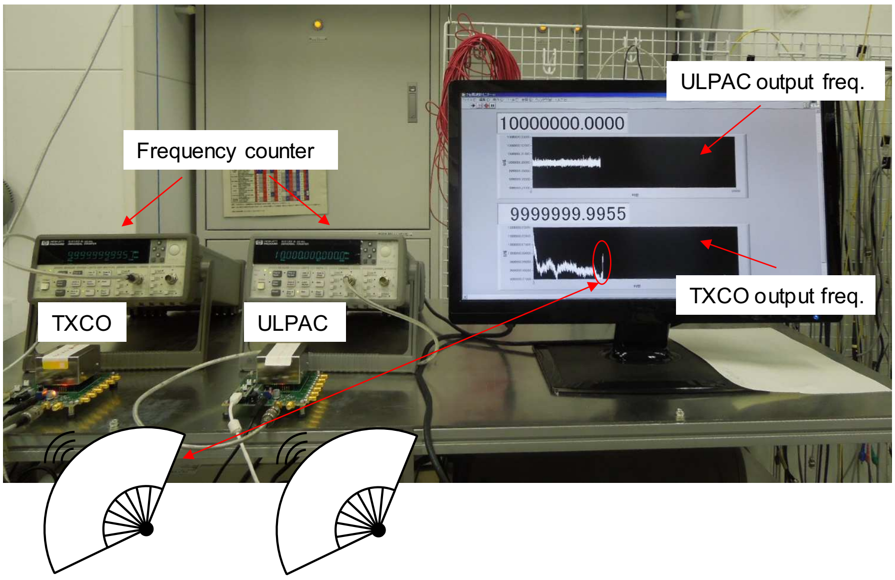

Figure 4.16: Demonstration setup of ULPAC.

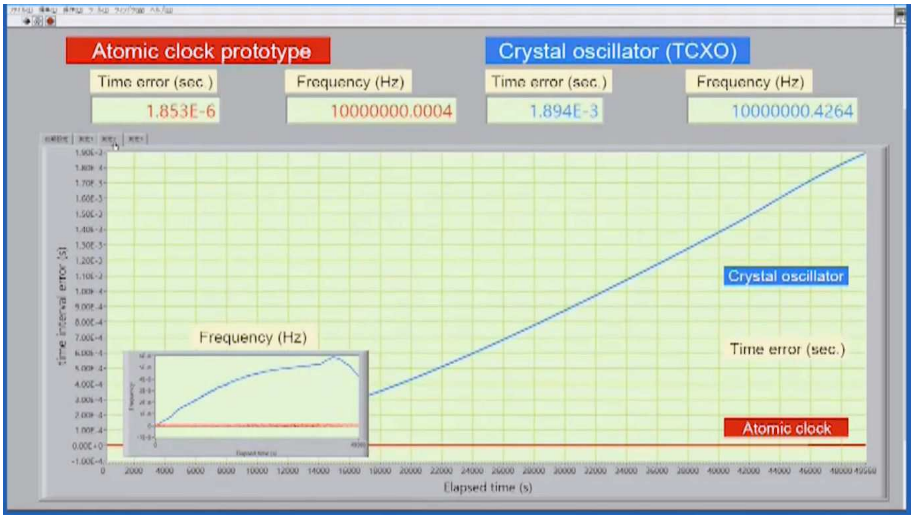

Figure 4.17: Measured time errors and frequency errors for both ULPAC and TCXO for 50000 s.

The Allan deviation plot may be scattered for $\tau > 10^5$ s, because the number of samples is relatively small. In order to ensure the statistical confidence of the calculated results, by using overlapping Allan deviation [54], $\sigma_y(\tau = 10^5\text{ s}) = 4.0 \times 10^{-12}$ is obtained redundantly.

One demonstration is also done for this ULPAC in comparison with TCXO based clock, as shown in Fig. 4.16. If we create a sudden environmental temperature change by

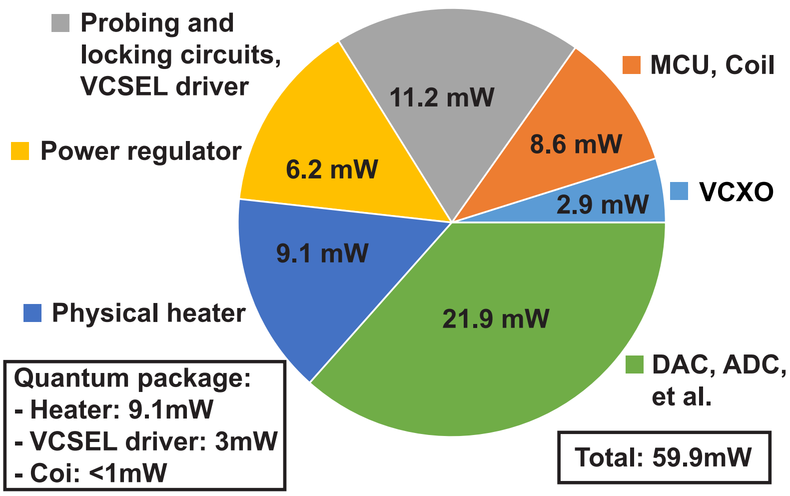

Figure 4.18: DC power consumption division of the ULPAC system.

using a fan, we could observe a sudden frequency jump for the TCXO, while no obvious frequency change is observed for the ULPAC. This indicates the effectiveness of the temperature control loop in the ULPAC and intrinsic frequency stability superiority of atomic resonance over that of the electromechanical oscillator. We also carried out a long time measurement to observe the long-term performance. The measured frequency error and time error for 50000 s are shown in Fig. 4.17. For the ULPAC, the time error could be maintained within 2 µs, the time error of TCXO based clock is around 2 ms.

4.5 System Power Consumption and Other Performance Metrics

The total power consumption of the ULPAC is 59.9 mW. The dc power consumption division is shown in Fig. 4.18. Thanks to the power-efficient probing and locking circuit and VCSEL driver, the most power-hungry part is not the RF circuit anymore but the converters. The highly thermally isolated quantum physical package consumes less than 13.1 mW. The power loss of power regulator due to voltage conversion could be removed by adopting a multi-voltage supply method for the system on chip (SoC) in the future. The power consumption could be further reduced by the custom design of the converters.

Temperature is assumed to be the major environmental variation for the atomic clock, and the stability due to temperature variation is assumed to be a key indicator of a high-performance atomic clock. The frequency deviation due to the temperature variations is also verified, as shown in Fig. 4.19. The temperature range for the LEO satellites

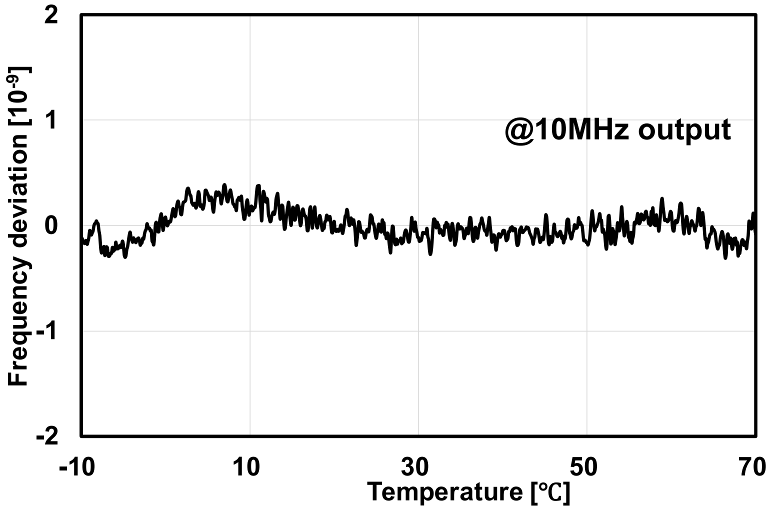

Figure 4.19: Fractional frequency variation due to temperature changes.

Table 4.1: Comparison of state-of-the-art miniaturized stable clocks.

Reference	Remarks	Volume (cm^3)	VCXO freq. (MHz)	Probing freq. (GHz)	P_{dc} (mW)	Max.[$\Delta f/f$] (10^{-10}) @ [−10°C ~ 70°C]	$\sigma_y @ \tau = 10^0$s (10^{-11})	$\sigma_y @ \tau = 10^3$s (10^{-11})	$\sigma_y @ \tau = 10^5$s (10^{-12})
[60]	Cs & D1	1	5	4.6	30	N/A	22.0	0.82	N/A
[138]	Cs	N/A	10	4.6	98	N/A	5.1	0.39	N/A
[68]	Rb & D1	1.7	10	3.4	57	N/A	15.0	1.1	N/A
[69]	Rb & D1	1	569	3.4	30	N/A	10.0	1	N/A
[139]	Rb & D1	N/A	40	3.4	N/A	N/A	5.2	2.4	30
[65]	Cs & D1	16	10	4.6	125	4	8	0.29	N/A
[61]	Molecular clock ($^{16}O^{12}C^{32}S$)	50	80	231.0	66*	22**	250.0	38	N/A
[66]	Cs & D1	16	10	4.6	120	±5	30.0	1	30***
Present study	Cs & D1	15	10	4.6	60	±2.8	6.7	0.8	2.2

* The power of the VCXO is not included, **Best case, calculated from the measurement result of frequency deviation due to pressure at 300 K temperature, ***From our measurement data under the same environment.

is from -170 $^\circ C$ to 123 $^\circ C$ in the space. However, since the ULPAC is packaged inside the satellite with an industrial thermal insulation, the temperature variation experienced by the ULPAC may be much narrower. For laboratory environmental measurements, the temperature was varied from -10 $^\circ C$ to 70 $^\circ C$. The measured frequency deviation could always be kept to less than $\pm 10^{-9}$ when the output frequency is 10 MHz. For a similar temperature range, the TCXO could only maintain a frequency deviation of $\pm 10^{-6}$, which is three-order worse [135–137]. The operating temperature range of the ULPAC can be easily extended by increasing the heater power consumption and the power budget.

Mechanical shock tests of this ULPAC for field deployment have also been carried out, and show that the proposed ULPAC could easily withstand a 500 G and 3 ms-pulse shock test, which meets most industrial deployments [140].

4.6 Conclusion

Table I shows the performance of the proposed ULPAC along with miniaturized atomic/molecular clocks and indicates that the proposed ULPAC achieves an optimum balance between the power consumption and frequency stability performance.

Chapter 5

Ultra-low-power RF Circuit Techniques

This chapter demonstrates some circuit design techniques for the low power frequency probing and locking loop for the next generation ULPAC. The RF circuits are typically the most power-hungry building blocks for an electronic system since they are operating at the highest frequency. In this section, one power-efficient CMOS oscillator and one ultra-low-power injection-locked (IL) PLL will be introduced. Similar circuit design techniques can be applied to achieve low power frequency probing and locking loop in the ULPAC system.

5.1 High Power-Efficient CMOS Oscillator

A high-performance CMOS oscillator is a key block in an RF system since it typically determines the signal purity and power consumption. Class-B VCO architecture has been widely adopted for the CMOS harmonic oscillator design. The popularity can be traced to its excellent phase noise performance and simple architecture, which comes at the expense of power consumption [141]. Class-C VCO has been proposed for improving the power efficiency without much phase noise degradation [142]. Compared with class-B VCO, the current efficiency of class-C VCO is much improved by reducing the conduction angle of the cross-coupled transistors. However, class-C VCO has an inevitable design trade-off between the robust start-up and power efficiency [143, 144], which requires additional start-up circuit and limits the phase noise performance.

In this section, a pulse VCO is proposed to avoid the trade-off in the class-C VCO but with potential higher power efficiency and lower phase noise [122, 123]. The low noise circuit design techniques such as the tail filter [119] are adopted to further mitigate the effect of noise contributors.

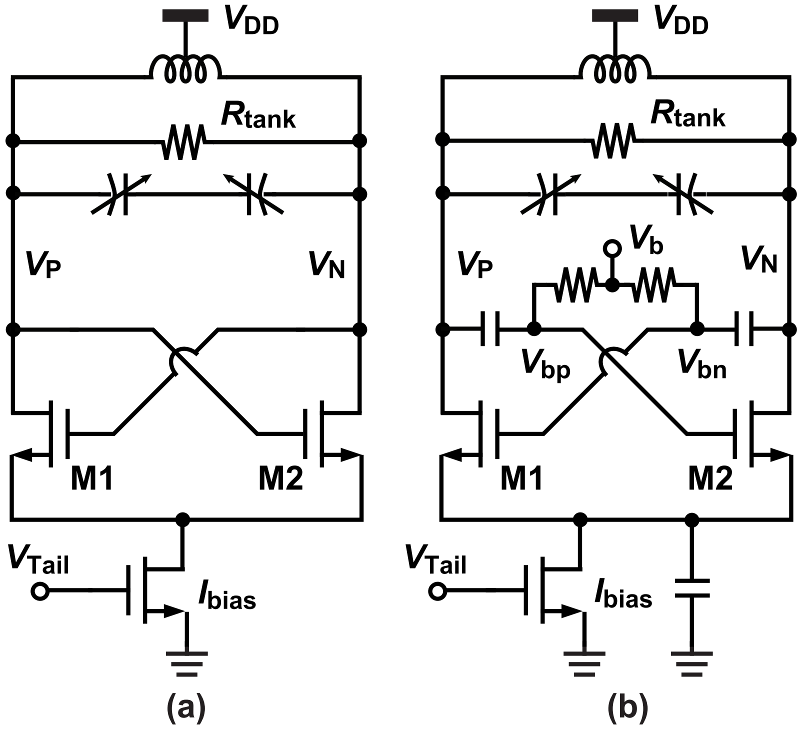

Figure 5.1: Circuit schematics for (a) class-B VCO and (b) class-C VCO.

5.1.1 Issues with class-C VCO

It has been proven that operating a VCO in the class-C mode improves its current efficiency without compromising the phase noise [142]. A simplified circuit schematic for class-C VCO is shown in Fig. 5.1 (b). It can be seen that unlike the class-B oscillator shown in Fig. 5.1 (a), the cross-coupled transistors in class-C VCO are decoupled from the supply voltage and biased with a different dc source. By keeping the bias voltage of the cross-coupled transistors sufficiently low, the transistors are forced to work in class-C mode with increased power efficiency as shown in Fig. 5.2.

The fundamental current amplitude $I_{\omega_\circ}$ in class-B VCO equals to $(2/\pi)\cdot I_{\text{bias}}$ according to the Fourier theory. While in class-C VCO, the $I_{\omega_\circ}$ can be close to I_{bias} with the help of the pulse shaping function of a large tail capacitor. In other words, the class-C VCO can achieve nearly 57% improvement in terms of the current efficiency. If assuming all the noise contributors are kept the same, this also translates into 3.9 dB FoM improvement.

However, special care must be taken to ensure that the cross-coupled transistors always stay in the saturation region for the class-C VCO. Otherwise, the amplitude of the fundamental current will reduce to approximately $0.62I_{\text{bias}}$ [142], degrading the current efficiency to class-B VCO. The saturation requirement largely limits the tank voltage

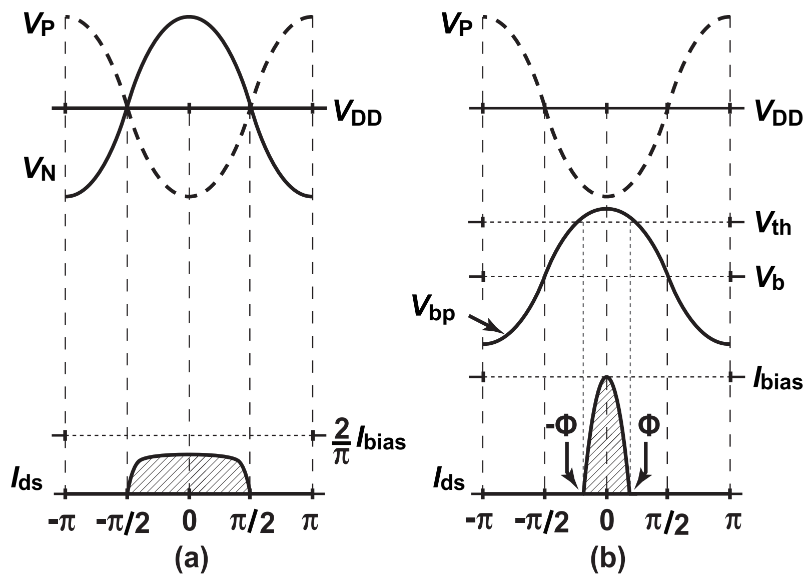

Figure 5.2: Waveforms of (a) class-B VCO and (b) class-C VCO.

amplitude A_{tank} to prevent the oscillator from entering into such a situation. Thus the maximum tank voltage amplitude A_{tank} can be expressed as follows to ensure the saturation requirement [143]:

$$A_{\text{tank}} < \frac{V_{\text{DD}} - V_{\text{od}}}{2} < V_{\text{DD}} \tag{5.1}$$

where V_{od} is defined as:

$$V_{\text{od}} = V_{\text{b}} - V_{\text{th}} \tag{5.2}$$

where V_{b} is the gate bias voltage of the cross-coupled transistors for the class-C VCO as shown in Fig. 5.2 (b). Since a larger tank voltage amplitude A_{tank} can result in a better phase noise [145], the bias voltage V_{b} should be well smaller than the threshold voltage V_{th} for better phase noise. However, biasing the transistors below their threshold voltage introduces reliability issues with VCO start-up.

The analysis done in the past literatures [142–144, 146–148] suggests that the power efficiency of a class-C VCO keeps decreasing as the conduction angle reduces. However, as discussed earlier, reducing the conduction angle in a conventional class-C VCO requires the reduction of V_{od}. The reduced V_{od} demands larger transistors to sustain the oscillations. The larger devices, in turn, result in a larger noise contribution from the active devices. The analysis carried out later reveals that any improvement in the current efficiency η_{I} achieved by reducing the conduction angle is overshadowed by the larger noise contribution from the cross-coupled transistors in the class-C VCO.

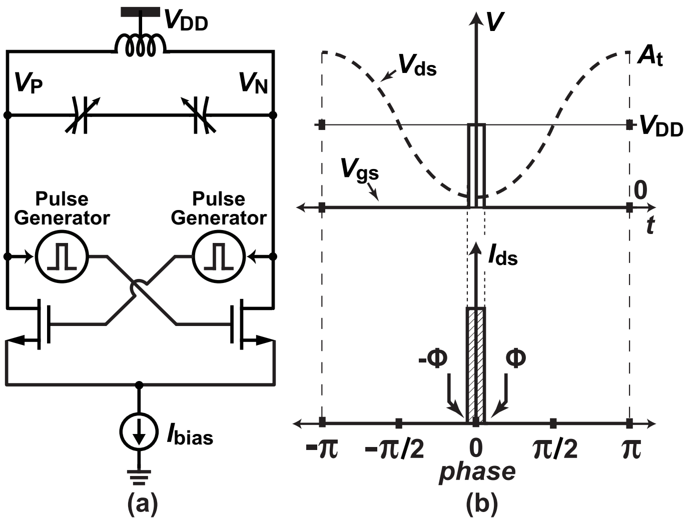

Figure 5.3: Conceptual diagram showing (a) pulse VCO schematic and (b) waveforms of interest.

5.1.2 Pulse VCO concept and architecture

Inspecting Fig. 5.3 reveals that a functionality similar to that of class-C VCO can be obtained if the cross-coupled transistors are driving by pulses that are synchronized to the oscillator, with pulse widths that are less than half cycle of oscillation period. By the laws of conservation, the total current conducted by the cross-coupled transistors pair over one oscillation cycle must remain the same as the bias current I_{bias}. As a result, the fundamental component of RF current enhances with reduction of pulse width 2Φ in order to compensate for the loss in the time $2(\pi - \Phi)$. It must be noticed that even though the proposed pulse VCO is similar to class-C VCO in functionality, they differ at a fundamental level, the proposed pulse VCO controls the conduction angle solely by changing the pulse width of the voltage signal used for driving the cross-coupled transistors.

This work presents a pulse VCO, which eliminates the interdependence between the conduction angle Φ and the overdrive voltage of the cross-coupled transistors V_{od}. Thus, the start-up issue in the conventional class-C VCO is removed in the pulse VCO. Besides the high power efficiency (similar to that of class-C VCO) is maintained without the need for increasing the size of the cross-coupled transistors by operating them in the triode region rather than in saturation region as in class-C VCO. This reduces the phase noise contribution from the cross-coupled transistors $N_{\mathrm{L,tr}}$. It also helps to reduce the parasitic capacitance of the cross-coupled transistors to the tank, which in turn improves the linearity of the tank and the frequency tuning range. A better phase noise performance due to the lower AM-PM noise conversion can be achieved in the more linear tank [149–151].

5.1.3 Analysis of pulse VCO

From here the power efficiency and phase noise of pulse VCO are analyzed in comparison with class-C VCO.

Following the extensive analysis done by A. Hajimiri and T. H. Lee [145], phase noise in an oscillator at an offset frequency $\Delta\omega$ can be represented as:

$$\mathcal{L}(\Delta\omega) = 10\log_{10}[\frac{\Sigma_i N_{\mathrm{L,i}}}{2\Delta\omega^2 C^2 A_{\mathrm{tank}}^2}] \tag{5.3}$$

where $N_{\mathrm{L,i}}$ is the effective current noise spectrum density generated by i_{th} device, $\Delta\omega$ is the offset frequency from the oscillation frequency, A_{tank} is the voltage amplitude of the tank network, C is the tank capacitance and can be defined as follows:

$$C = Q_{\mathrm{tank}}/(\omega_{\mathrm{o}} R_{\mathrm{tank}}) \tag{5.4}$$

where Q_{tank} is the loaded tank qualify factor and R_{tank} is the tank impedance, ω_{o} is the oscillation frequency.

A figure of merit (FoM) can be defined for the fair comparison of different VCOs by normalizing the VCO phase noise to the oscillation frequency ω_{o}, the offset frequency $\Delta\omega$ and dissipated power (in mW). Assuming that the major noise sources are the tank network and the cross-coupled transistors, and recognizing that the RF signal power can be represented as: $P_{\mathrm{sig}} = A_{\mathrm{tank}}^2/2R_{\mathrm{tank}}$, FoM can be represented as [152]:

$$\mathrm{FoM} = -10\log_{10}[\frac{N_{\mathrm{L,tank}} + N_{\mathrm{L,tr}}}{4Q_{\mathrm{tank}}^2} \cdot \frac{R_{\mathrm{tank}}}{\eta_{\mathrm{P}} \times 10^{-3}}] \tag{5.5}$$

where $\eta_P = \frac{P_{\mathrm{sig}}}{P_{\mathrm{dc}}} = \frac{I_{\mathrm{sig}}}{I_{\mathrm{dc}}}\frac{V_{\mathrm{sig}}}{V_{\mathrm{dc}}} = \eta_{\mathrm{I}}\eta_{\mathrm{V}}$ is the power efficiency (η_{I} and η_{V} are the current efficiency and voltage efficiency, respectively, I_{sig} is the fundamental output current, V_{sig} is the fundamental output voltage, I_{dc} is the dc current and V_{dc} is the dc voltage.), $N_{\mathrm{L,tank}}$ and $N_{\mathrm{L,tr}}$ represent the current noise spectrum densities from the tank network and the cross-coupled transistors, respectively, and they can be expressed as:

$$N_{\mathrm{L,tank}}(\phi) = \frac{1}{2\pi}\int_{-\pi}^{\pi} \Gamma_{\mathrm{out}}^2(\phi) 4\mathrm{k_B} T \frac{1}{R_{\mathrm{tank}}}\,\mathrm{d}\phi \tag{5.6}$$

$$N_{\mathrm{L,tr}}(\phi) = \frac{1}{2\pi}\int_{-\pi}^{\pi} \Gamma_{\mathrm{out}}^2(\phi) 4\mathrm{k_B} T \gamma g_{\mathrm{m}}(\phi)\,\mathrm{d}\phi \tag{5.7}$$

where $\Gamma_{\mathrm{out}}(\phi) = -h\cos(\phi)$ defines the impulse sensitivity function (ISF) at the output node of the VCO [145, 153] (h is a real constant), k_B is the Boltzmann's constant, T is the absolute temperature, γ is a device dependent constant. Using Eqs. (5.6) and (5.7) into Eq. (5.5) leads to the following expression [154]:

$$\mathrm{FoM} = -10\log_{10}\Big[\frac{k_B T(\Gamma^2_{\mathrm{tank,rms}} + \Gamma^2_{\mathrm{tr,rms}}\alpha)}{10^{-3} Q^2_{\mathrm{tank}} \eta_P}\Big] \tag{5.8}$$

where $\Gamma^2_{\mathrm{tank,rms}}$ and $\Gamma^2_{\mathrm{tr,rms}}$ are the RMS ISF of tank impedance and transistor, respectively, α is a noise factor that includes γ and attenuation between tank and MOS gates.

Eq. (5.8) reveals two approaches to improve the performance of VCO: (i) by reducing the noise from the transistors $N_{L,tr}$; (ii) by increasing power efficiency either by improving the voltage efficiency η_V or current efficiency η_I.

Assuming 100% power efficiency, $\Gamma^2_{\mathrm{tank,rms}} = 1/2$ [145], noiseless transistors and no other noise contribution, the FoM, called $\mathrm{FoM_{MAX}}$ defining the ultimate performance achievable by a harmonic oscillator can be expressed by [154]:

$$\mathrm{FoM_{MAX}} = 173.8\mathrm{dBc/Hz} + 10\log_{10}(2Q^2_{\mathrm{tank}}) \tag{5.9}$$

Then the excess noise factor (ENF) can be defined [155]:

$$\mathrm{ENF} = \mathrm{FoM_{MAX}} - \mathrm{FoM} = 10\log_{10}\Big[\frac{1 + \frac{N_{L,tr}}{N_{L,tank}}}{\eta_P}\Big] \tag{5.10}$$

In order to further improve the FoM, the ENF should be minimized. It serves as an excellent bench-marking tool for evaluating different VCO topologies.

First, the power efficiency of the proposed pulse VCO is calculated. For calculating the power efficiency of the proposed pulse VCO, let us assume a supply voltage of V_{DD} and a negligible source voltage at the cross-coupled transistors. The gate to source voltage $V_{gs}(\phi)$ and drain to source voltage $V_{ds}(\phi)$ for the proposed pulse VCO can thus be written as:

$$V_{gs}(\phi) = \begin{cases} V_{DD}, & -\Phi < \phi < \Phi \\ 0, & -\phi < -\Phi, \Phi < \phi \end{cases} \tag{5.11}$$

$$V_{ds}(\phi) = V_{DD} - A_{\mathrm{tank}} \cdot \cos(\phi) \tag{5.12}$$

Since the cross-coupled transistors turn on in the triode region in the proposed pulse VCO, the drain current I_{ds} and g_m can be represented as:

$$I_{ds}(\phi) = \begin{cases} \beta\Big(V_{DD} - V_{th} - \frac{V_{ds}(\phi)}{2}\Big), & -\Phi < \phi < \Phi \\ 0, & \phi < -\Phi, \Phi < \phi \end{cases} \tag{5.13}$$

$$g_m(\phi) = \frac{\partial I_{ds}(\phi)}{\partial V_{gs}(\phi)} = \begin{cases} \beta V_{ds}(\phi), & -\Phi < \phi < \Phi \\ 0, & \phi < -\Phi, \Phi < \phi \end{cases} \tag{5.14}$$

The dc component of the transistor current I_o can be calculated:

$$\begin{aligned} I_o &= \frac{1}{2\pi}\int_{-\Phi}^{\Phi} I_{ds}(\phi)\mathrm{d}\phi \\ &= \frac{\beta}{8\pi}\left[8V_{th}(\Phi V_{DD} - A_{tank}\sin(\Phi)) - 4\Phi V_{DD}^2 + A_{tank}^2\sin(2\Phi) + 2A_{tank}^2\Phi\right] \end{aligned} \tag{5.15}$$

Using Fourier's theory, the fundamental harmonic of the current in a pulse VCO $I_{\omega_\circ}$ can be calculated as:

$$\begin{aligned} I_{\omega_\circ} &= \frac{1}{\pi}\int_{-\Phi}^{\Phi} I_{ds}(\phi)\cos(\phi)\,\mathrm{d}\phi = \frac{\beta}{6\pi}\Big[\Big(4\sin(\Phi)V_{DD} - A_{tank}\sin(2\Phi) - 2A_{tank}\Phi\Big) \\ & 3V_{th} - 6\sin(\Phi)V_{DD}^2 - 2A_{tank}^2\sin(\Phi)^3 + 6A_{tank}^2\sin(\Phi)\Big] \end{aligned} \tag{5.16}$$

If the bias current $I_{bias} = 2I_\circ$, the dc power to RF power conversion efficiency η_I can be thus calculated from Eqs. (5.15) and (5.16) as:

$$\eta_I = \frac{1}{\sqrt{2}}\cdot\frac{I_{\omega_\circ}}{2I_\circ} = \frac{1}{\sqrt{2}}\cdot\frac{I_{\omega_\circ}}{I_{bias}} = \frac{1}{\sqrt{2}}\Big(1 - \frac{\Phi^2}{6} + \cdots\Big) \tag{5.17}$$

Assuming an ideal LC tank tuned at $\omega_\circ$, the impedance of the tank network can be defined as:

$$Z_{tank}(\omega) = \begin{cases} 0, & \omega = 0,\ 2\omega_\circ,\ 3\omega_\circ,\ \ldots \\ R_{tank}, & \omega = \omega_\circ \end{cases} \tag{5.18}$$

The voltage at one output node of the oscillator V_P is defined as:

$$V_P(t) = V_{DD} - \sum_{n=0}^{\infty}\frac{Z_{tank}(n\omega_\circ)}{2}\times I_{ds}(n\omega_\circ t)\cos(n\omega_\circ t) \tag{5.19}$$

$$V_P(\phi) \approx V_{DD} - \frac{R_{tank}}{2}I_{\omega_\circ}\cos(\phi) \tag{5.20}$$

Substituting $A_{tank} = \frac{\sqrt{2}R_{tank}I_{bias}}{2}$, the differential tank oscillation amplitude can be calculated from Eq. (5.20) as:

$$V_{out}(\phi) = V_P(\phi) - V_N(\phi) = -R_{tank}I_{\omega_\circ}\cos(\phi) = -2A_{tank}\cos(\phi) \tag{5.21}$$

If $V_{RF,rms}$ represents the RMS value of the differential tank voltage amplitude, the voltage efficiency of a differential VCO can be calculated as:

$$\eta_{\mathrm{V}} = \frac{V_{\mathrm{RF,rms}}}{V_{\mathrm{DD}}} = \frac{\sqrt{2}\,A_{\mathrm{tank}}}{V_{\mathrm{DD}}} \tag{5.22}$$

The oscillation amplitude of the proposed pulse VCO is determined only by the tank impedance in contrast with that of conventional class-C VCO, in which the oscillation amplitude is also a function of the transistor gate voltage (Eq. (5.1)). Assuming ideal conditions ($A_{\mathrm{tank}} = V_{\mathrm{DD}}$), the maximum voltage efficiency for a pulse VCO can be approximated as:

$$\eta_{\mathrm{V}} \approx \sqrt{2} \tag{5.23}$$

The power efficiency ($\eta_{\mathrm{P}} = \eta_{\mathrm{I}} \times \eta_{\mathrm{V}}$) for a pulse VCO approaches 100% as the conduction angle approaches zero.

Following the above method, the power efficiency of class-C VCO is derived as well. The gate to source voltage of class-C VCO can be represented in terms of oscillation amplitude and conduction angle as follows:

$$V_{\mathrm{gs,class-C}}(\phi) = V_{\mathrm{bias,class-C}} - V_{\mathrm{th}} + A_{\mathrm{tank}} \cos(\Phi) = A_{\mathrm{tank}} \left(\cos(\phi) - \cos(\Phi)\right) \tag{5.24}$$

The drain current I_{ds} and the transconductance g_{m} of class-C VCO can be written as

$$I_{\mathrm{ds,class-C}}(\phi) = \begin{cases} \frac{\beta}{2} V^2_{\mathrm{gs,class-C}}(\phi), & -\Phi < \phi < \Phi \\ 0 & \phi < \Phi, \Phi < \phi \end{cases} \tag{5.25}$$

$$g_{\mathrm{m,class-C}}(\phi) = \begin{cases} \beta V_{\mathrm{gs,class-C}}(\phi), & -\Phi < \phi < \Phi \\ 0 & \phi < \Phi, \Phi < \phi \end{cases} \tag{5.26}$$

Following the procedure used for deriving Eqs. (5.15) and (5.16), the integrated dc current and fundamental current in conventional class-C VCO can be calculated as:

$$I_{\circ,\mathrm{class-C}} = \frac{\beta}{2\pi} A^2_{\mathrm{tank}} \left[\frac{-3}{2} \cos(\Phi) \sin(\Phi) + \frac{\Phi}{2} + \Phi \cos^2(\Phi) \right] \tag{5.27}$$

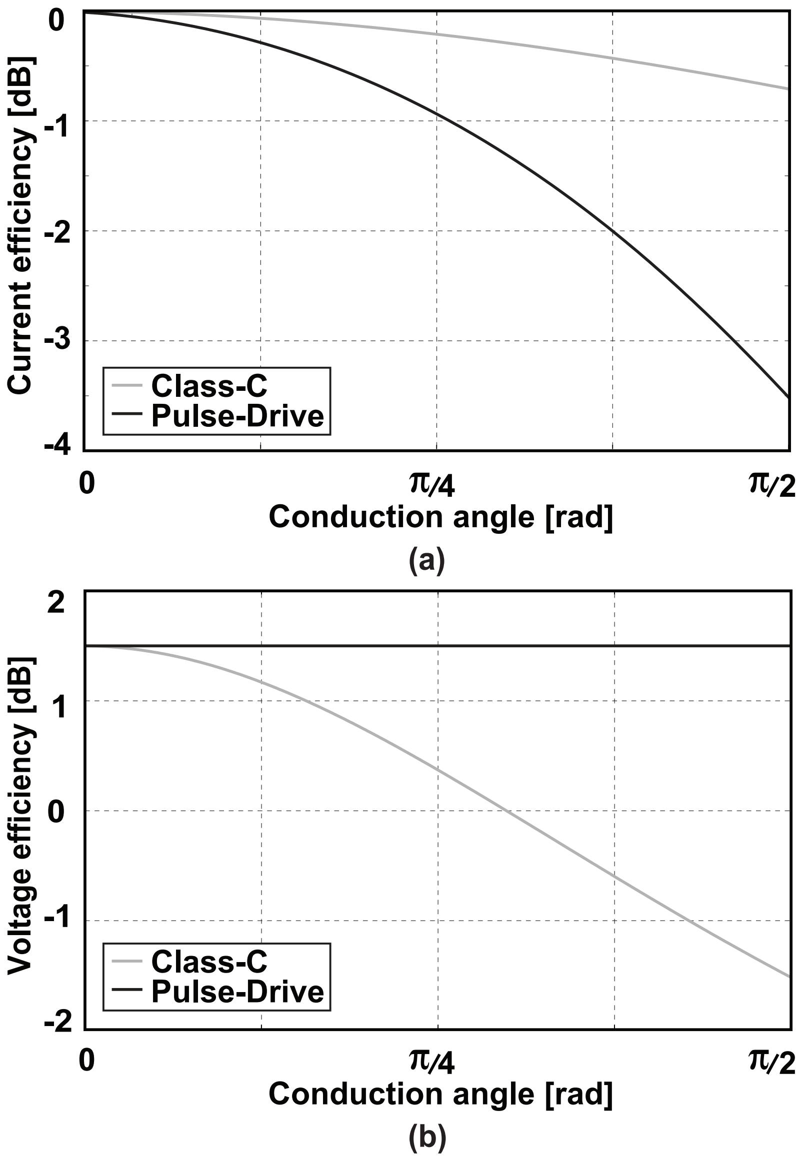

Figure 5.4: Comparison between (a) calculated current efficiency and (b) calculated voltage efficiency of pulse VCO and class-C VCO.

$$I_{\omega_\circ,\text{class-C}} = \frac{\beta}{\pi}A_{\text{tank}}^2\left[\frac{-1}{3}\cos^2(\Phi)\sin(\Phi) + \frac{2}{3}\sin(\Phi) - \Phi\cos(\Phi)\right] \tag{5.28}$$

Current efficiency of class-C VCO can thus be calculated as [142]:

$$\eta_{\text{I,class-C}} = \frac{1}{\sqrt{2}}\left(1 - \frac{\Phi^2}{14} + \dots\right) \tag{5.29}$$

From Eqs. (5.17) and (5.29), it can be seen that the class-C VCO exhibits excellent current efficiency even at moderate conduction angles. Recalling that the oscillation amplitude of class-C VCO is bounded by saturation criterion Eq. (5.1), the voltage efficiency of conventional class-C VCO can be calculated as:

$$A_{\text{tank,class-C}} \le \left[\frac{V_{DD}}{2 - \cos(\Phi)}\right] \tag{5.30}$$

$$\eta_{\text{V,class-C}} \le \left[\frac{\sqrt{2}}{2 - \cos(\Phi)}\right] \tag{5.31}$$

The current efficiency η_{I} and voltage efficiency η_{V} of proposed pulse VCO and conventional class-C VCO are compared in Fig. 5.4 (a) and (b), respectively. Unlike proposed pulse VCO, which maintains high voltage efficiency irrespective of the conduction angle (Eq. (5.23)), conventional class-C VCO achieves high voltage efficiency ($\approx \sqrt{2}$) only at very low conduction angles ($\Phi < \pi/8$) as evident from Eq. (5.31). The power efficiency of the proposed pulse VCO is comparable to that of class-C VCO at conduction angles less than $\pi/8$ as shown in Fig. 5.5 (a).

The noise performance of proposed pulse VCO is also compared with that of conventional class-C VCO. The noise generated by the cross-coupled transistors in the proposed pulse VCO and the conventional class-C VCO is calculated from Eqs. (5.14), (5.26) and (5.7), and is plotted in Fig. 5.5 (b). Using Eq.(5.6)–(5.7), Eq. (5.12)–(5.14) and Eq. (5.19)–(5.20), the expression for transistor noise normalized to the tank noise of pulse VCO can be written as:

$$\frac{N_{\text{L,tr}}}{N_{\text{L,tank}}} = \gamma\left[\left(\frac{2A_{\text{tank}}}{2V_{\text{th}} - V_{\text{DD}} - A_{\text{tank}}}\right) + \frac{A_{\text{tank}}}{3}\left(\frac{2V_{\text{th}} - V_{\text{DD}}}{4V_{\text{th}}\left(V_{\text{th}} - V_{\text{DD}} - A_{\text{tank}}\right) + V_{\text{DD}}^2 + 2A_{\text{tank}}V_{\text{DD}} + A_{\text{tank}}^2}\right)\right] + \cdots \tag{5.32}$$

The expression for transistor noise normalized to the tank noise of conventional class-C

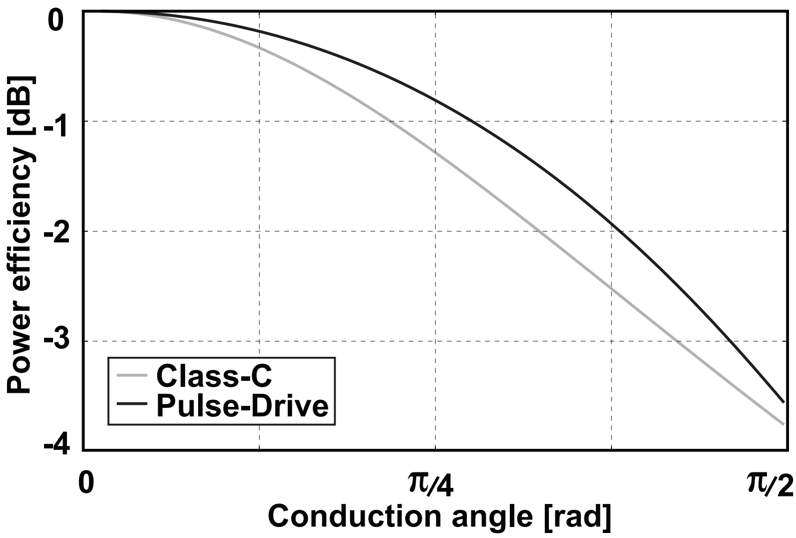

(a)

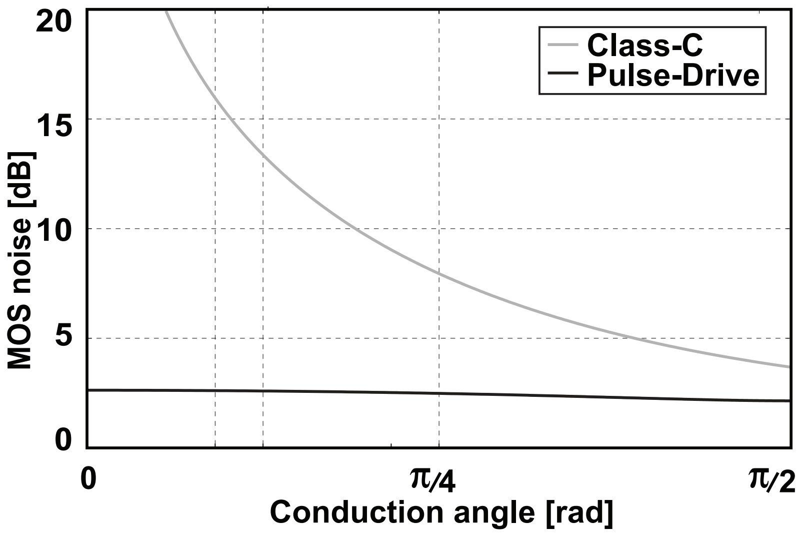

(b)

Figure 5.5: Comparison between (a) calculated power efficiency and (b) calculated transistor's noise generated in pulse VCO and class-C VCO.

VCO can be calculated from Eq.(5.24)−(5.26) and Eq. (5.19)−(5.20):

$$\frac{N_{\mathrm{L,tr,class-C}}}{N_{\mathrm{L,tank,class-C}}} = \gamma\left[\frac{3\cos(\Phi)\sin(2\Phi) + 4\sin(\Phi)^3 - 12\sin(\Phi) + 6\Phi\cos(\Phi)}{3\cos(\Phi)\sin(2\Phi) + 8\sin(\Phi)^3 - 12\sin(\Phi) + 6\Phi\cos(\Phi)}\right]$$
$$= \gamma\left[\frac{5}{\phi^2} - \frac{4}{21} + \frac{3\phi^2}{49} + \cdots\right] \quad (5.33)$$

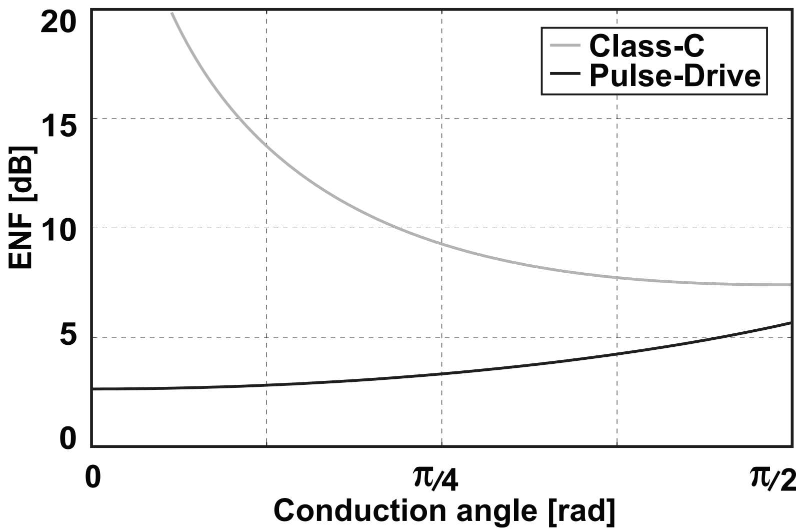

Figure 5.6: Calculated values for ENF in pulse VCO compared with ENF in class-C oscillator.

Table 5.1: Estimated ENF of class-C VCO and pulse VCO at various conduction angles of interest.

Topology		η_I	η_V	η_P	$\frac{N_{L,tr}}{N_{L,tank}}$ [dB]	ENF [dB]
Class-C	Equation	$\frac{1}{\sqrt{2}}\left(1-\frac{\Phi^2}{14}+\cdots\right)$	$\frac{\sqrt{2}}{2-\cos(\Phi)}$	$\eta_V \cdot \eta_I$	(5.33)	(5.10)
	$\Phi \to 0$	$\frac{1}{\sqrt{2}}$	$\sqrt{2}$	1	~ 25	~ 25
	$\Phi \to \pi/2$	$\frac{1}{\sqrt{2}}\left(\frac{8}{3\pi}\right)$	$\frac{1}{\sqrt{2}}$	$\frac{4}{3\pi}$	~ 7.4	~ 7.4
Pulse	Equation	$\frac{1}{\sqrt{2}}\left(1-\frac{\Phi^2}{6}+\cdots\right)$	$\sqrt{2}$	$\eta_V \cdot \eta_I$	(5.32)	(5.10)
	$\Phi \to 0$	$\frac{1}{\sqrt{2}}$	$\sqrt{2}$	1	~ 2.6	~ 2.6

The ENF of class-C VCO is calculated by substituting Eq. (5.33) in Eq. (5.10). Similarly, the ENF of pulse VCO is calculated by substituting Eq. (5.32) in Eq. (5.10). The ENF comparison result of pulse VCO and class-C VCO is plotted against the conduction angle Φ in Fig. 5.6, which reveals that pulse-drive approach is capable of achieving extremely high efficiency by reducing the conduction angle without increasing the noise from the active elements.

Table 5.1 summarizes the analysis done in this section with the ENF evaluated at the optimum conduction angles for pulse VCO and class-C VCO, which shows a theoretical improvement of approximately 5 dB in FoM for pulse VCO.

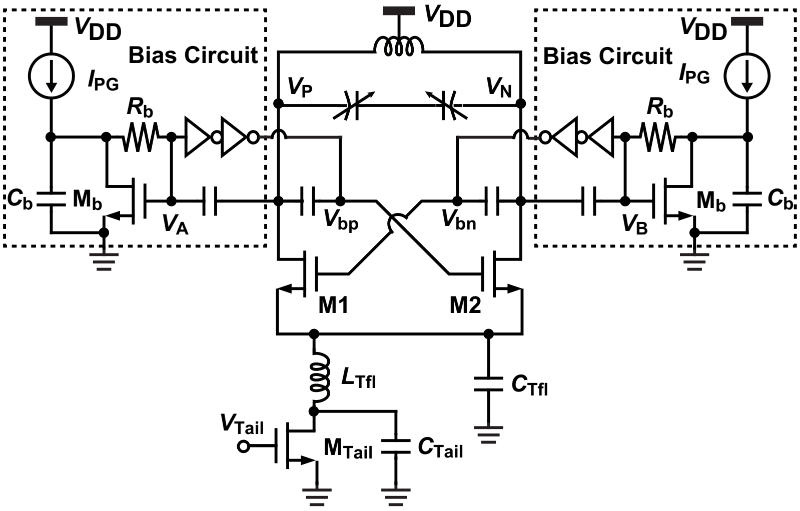

Figure 5.7: Complete pulse-VCO schematic with tail filtering.

5.1.4 Implementation and evaluation results

The most challenging aspect of practically implementing a pulse VCO is the generation of oscillation-synchronized pulses with minimum area and power overhead. With the introduction of short-channel devices, we now have the technology to generate such pulses for driving the active elements of the VCO. A VCO using the proposed pulse-VCO architecture is shown in Fig. 5.7. The capacitor bank for the frequency tuning is not shown for simplicity. The proposed method uses the time-variant nature of the VCO for the pulse generation and it does not require any modification in the tank network.

The synchronized pulse generator with automatic pulse width control has two subfunctions (i) conduction-angle control and (ii) amplitude re-generator. The detailed operation can be understood by analyzing the conceptual timing diagram shown in Fig. 5.8. When the oscillator is starting up, the bias transistor M_b in the conduction angle control module is switched off and the bias current I_{PG} flows only through the capacitor C_b. The bias current I_{PG} and bias resistor R_b are designed in such a way so as to provide a voltage V_A that is higher than the threshold voltage of the amplitude re-generator. As a result, the output of the amplitude re-generator V_{bp} is set at the supply rail V_{DD}, enhancing the transconductance for robust start-up. Once the oscillations build up in the VCO core, the bias transistor M_b switches between on and off state. This reduces the current flowing through the bias capacitor C_b, which in turn brings down the potential V_A. It can be observed from Fig. 5.8 that this process reduces the dc bias of the amplitude re-generator sub-block and as a result, the width of the pulses at the output node V_{bp} reduces. Under steady-state, this pulse-generator circuitry produces voltage pulses with a pulse width of

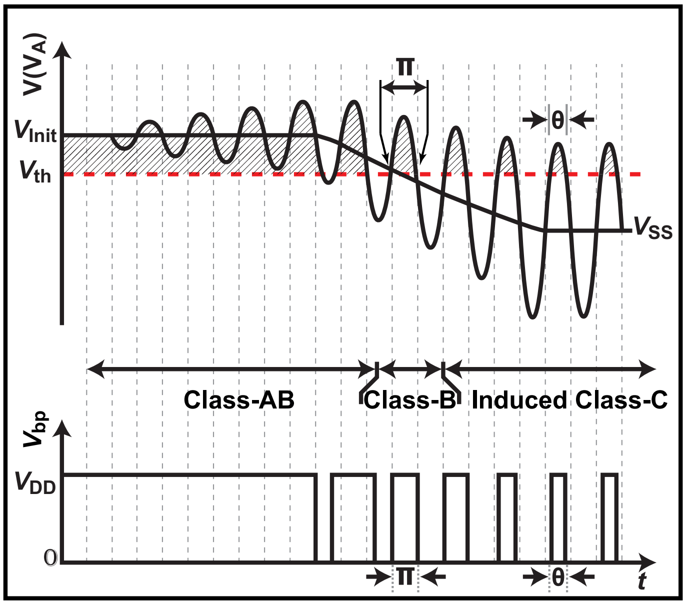

Figure 5.8: Conceptual waveform showing the robust start-up and high-efficiency steady-state operation.

less than half an oscillation cycle. This forces the transistors of the cross-coupled transistors to be in off state for the rest of the cycle, thus inducing a class-C like operation. The conduction angle Φ is mainly determined by the size of the transistor M_b and the bias current I_{PG}, which is around 10° with 50 μA bias current in the simulation. The total power consumption of the pulse generator is 0.15×2 mW.

As stated before, the pulse VCO has the loading effect as the cross-coupled transistors working in the triode region. The tank of VCO is comprised of a capacitor-bank, a varactor, and an inductor. The quality factor Q_{tank} is mainly determined by the above three components, of which the effect of parasitic impedance of the inductor is dominant. However, the switching operation of the cross-coupled transistors adds one more loading path for the tank depending on the state of the transistors. As upon starting up, the tank amplitude A_{tank} is smaller than V_{th}. Both the cross-coupled transistors are in saturation, enabling the oscillation start-up. As the oscillation grows up, the A_{tank} is larger than the V_{th}, forcing one transistor to enter into the triode region and the other into deeper saturation. For $V_{\text{ds}} < V_{\text{gs}} - V_{\text{th}}$, the drain current noise spectral density can be calculated according to Nyquist theorem [156, 157]:

$$\begin{aligned} i_{\text{d}}^2/\Delta f =& 4kT\mu C_{\text{ox}}\frac{W}{L}\frac{2}{3} \\ & [\frac{3(V_{\text{gs}}-V_{\text{th}})V_{\text{ds}}-3(V_{\text{gs}}-V_{\text{th}})^2-V_{\text{th}}^2}{2(V_{\text{gs}}-V_{\text{th}})-V_{\text{ds}}}] \end{aligned} \tag{5.34}$$

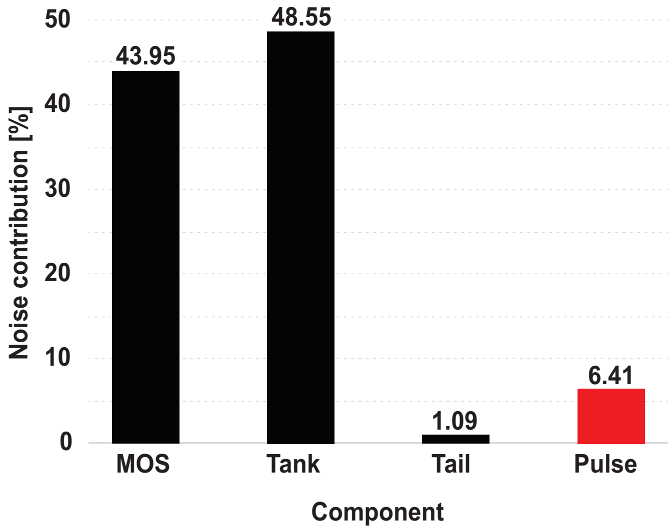

Figure 5.9: Noise contributed by various components of the VCO.

From Eq. (5.34), it's not difficult to see that as the A_{tank} grows up and under $V_{\mathrm{ds}} < V_{\mathrm{gs}} - V_{\mathrm{th}}$ situation, more loss will add to the resonant tank because the noise current is in-phase with the tank voltage. When an ideal tail current source is assumed, the open circuit stops the noise current flowing into the ground. However, for the class-C like operation, a large capacitor is inserted between the common source of the cross-coupled transistors and ground to sharp the pulse-like current, improving the current efficiency [142]. But this forms a low impedance path for the current noise of the cross-coupled transistors to the ground, which is termed as loading effect. As a result, both the tank amplitude and tank qualify factor are severely degraded. From the loading effect point, it is desirable to remove the large tail capacitor. Thus a trade-off exists between the high efficiency and the loading effect.

A high impedance is required at the second harmonic at the common point preventing the formation of the low impedance path for loading effect. Meanwhile, a large tail capacitor is wanted to filter the flicker noise and high-frequency noise in the tail transistor. The tail filter technique is adopted here as shown in Fig. 5.7, creating a high impedance path from the common source of the cross-coupled transistors to the drain of the tail transistor [119]. By doing so, the power-efficient pulse VCO removes the additional loading path, improving the phase noise performance. Also, the ENF of the pulse VCO can be simply calculated without considering the loading effect.

An on-chip inductor with a qualify factor of 20 is used in the tank, which determines the Q_{tank}. The tank amplitude A_{tank} is 0.74 V in the post-layout simulation under 1 V supply voltage, which translates into 104.65% voltage efficiency. The decreased A_{tank} from

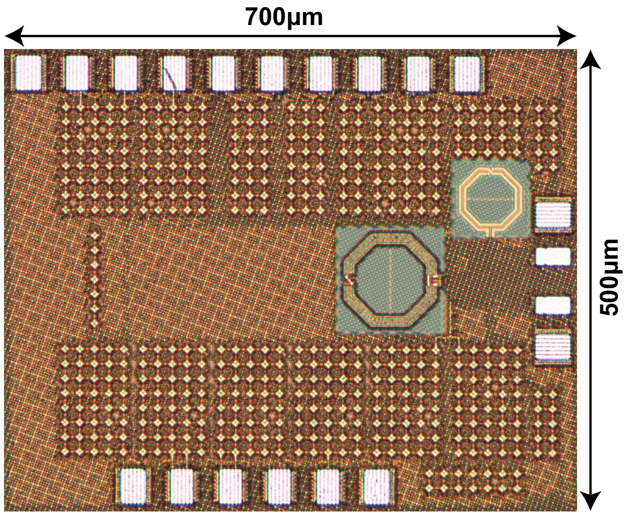

Figure 5.10: Chip die photo of pulse VCO.

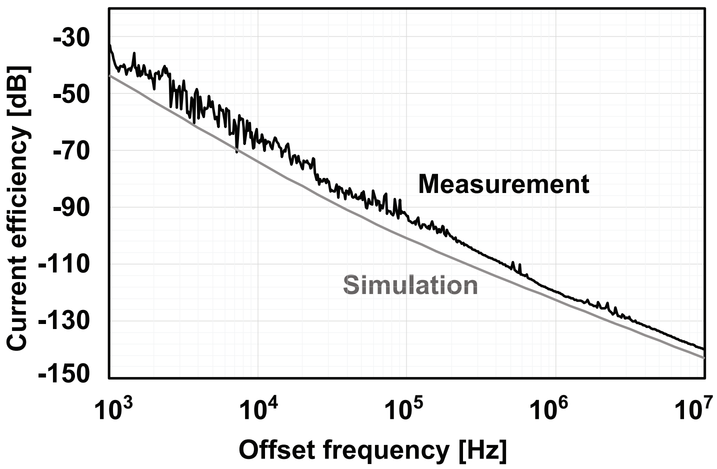

Figure 5.11: Phase noise measurement result at 5.0 GHz oscillation frequency.

the ideal V_{DD} is due to the V_{ds} of the tail transistor and parasitic components in the layout. The simulated noise contribution of the proposed pulse VCO is shown in Fig. 5.9, which reveals that the noise of the pulse generator is negligible in comparison with the transistor noise and tank noise. The proposed pulse VCO is capable of achieving high power efficiency with very little area and power overhead [122, 149].

The proposed VCO is manufactured in a standard 45 nm SOI CMOS process. The chip die photo of the fabricated pulse VCO is shown in Fig. 5.10. The area occupied by the VCO core is only 0.35 mm^2. The fabricated VCO has a measured frequency center of 4.8 GHz. A 3-bit capacitor bank is used for achieving 13.5 % tuning range. The phase

Table 5.2: Comparison of state-of-the-art highly-efficient CMOS VCOs.

Reference	Remarks	Process (nm)	Frequency (GHz)	Tuning range (%)	Phase Noise (dBc/Hz)	P_{dc} (mW)	Area (mm^2)	FoM (dBc/Hz)
[143]	Class-C (Dual)	180	4.5	nd	-109@1MHz	0.2	0.29	190.0
[144]	Class-C (Adaptive)	180	4.8	2.3	-125@1MHz	3.4	0.15	193.0
[158]	Tail Current-Shaping	250	1.8	18.9	-120@0.6MHz	2.3	N.A	186.0
[159]	Transformer Couple	180	3.8	8.4	-119@1MHz	0.6	0.76	193.0
[160]	Class-D	65	3.8	46.0	-152@10MHz	7.0	0.12	191.0
[161]	Clip & Restore	65	4.8	10.2	-142@3MHz	25.8	0.19	190.0
[162]	Class-F	65	3.9	25.0	-142@3MHz	15.0	0.12	192.2
This	Pulse + Tail-Filter	45	5.0	13.6	-120@1MHz	1.35	0.35	191.0

noise is evaluated using an Agilent E5052B signal source analyzer (SSA). At a frequency of 5.0 GHz, the proposed pulse VCO achieves phase noise of -120 dBc/Hz at 1 MHz offset frequency as shown in Fig. 5.11 , while consuming 1.35 mW from a supply voltage of 1 V. The FoM of the pulse VCO is calculated as -191 dBc/Hz. The low noise generated from the cross-coupled transistors and the high power efficiency of the proposed pulse VCO help in the improvement of the FoM. Measurements under a wide range of supply voltage V_{DD} and temperature T were carried out for validating the stability of the proposed VCO topology. With a bias current $2I_{\mathrm{PG}}$ of 100μA, robust start-up and sustained oscillations are observed under wide range of operating temperatures (-40°C to +80°C) and power supply voltage (0.6V - 1.2V). From simulation, the start-up time is always below 50 ns under different corners. Table 5.2 shows the performance comparison of the proposed pulse VCO with other state of art VCOs, which indicates that the proposed VCO has the capability to achieve high performance with negligible area and power overhead.

Compared with the highest FoM of class-C VCO, there is still 2 dB improvement for the pulse VCO. One reason could be traced back to the time delay caused by the pulse generator. According to the ISF [145], if the injection time of the pulse applied to the gates of the cross-coupled transistors is offset from the phase insensitive point, the noise from the cross-coupled transistors will increase considerably. This could be mitigated by using faster transistors in the pulse generator or some other circuit techniques to synchronize the driving pulses with tank oscillation.

5.2 0.2 mW Injection Locked Phase-locked Loop

A frequency synthesizer with ultra-low power consumption and high signal purity is one of the key building blocks for various RF system. In ULPAC, a low phase noise synthesizer lowers down the VCSEL FM noise. Also the power consumption of the frequency

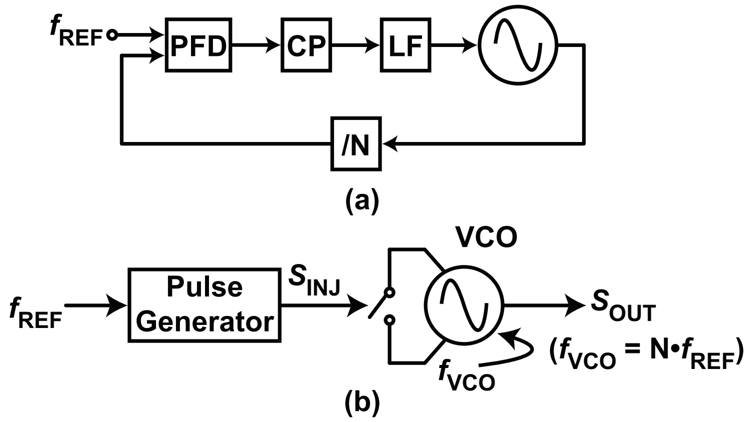

Figure 5.12: (a) Charge-pump based analog PLL. (b) Injection locked (IL) oscillator.

synthesizer is one of two most power hungry components for the frequency probing and locking circuit. The other one is the power amplifier. In this section, one ultra-low power and low jitter frequency synthesizer based on injection technique is introduced.

5.2.1 Injection locked PLL architecture

The charge-pump based analog PLL shown in Fig. 5.12 (a) has been widely used for its robustness and simple architecture. In this architecture, the noise contributors can be divided into reference referred noise and VCO noise. They have different noise transfer functions (NTF) when converting into PLL output phase noise, as shown in Fig. 5.13 (a). The reference referred noise is low pass filtered, while the VCO noise is high pass filtered, as shown in Fig. 5.13 (b). In order to achieve an optimal total output phase noise performance, the loop bandwidth is determined by the trade-off between these two types of phase noise. When the reference referred phase noise dominates, the loop-bandwidth should be narrow enough to low pass filter the reference noise. When the VCO phase noise is dominant, the loop-bandwidth should be wide enough to high pass the VCO noise. Thus, for a low power VCO design, the PLL output phase noise will be limited by the VCO phase noise, as shown in Fig. 5.13 (b). In this case, larger loop bandwidth would result in a better phase noise performance. However, in the conventional PLL, the maximum loop bandwidth is limited to be approximately $0.1 \times f_{\text{ref}}$ due to loop stability issue [163].

Since from last centruy, people realized that the injection locked oscillator (IL-VCO) could also achieve integer-N frequency synthesis, as shown in Fig. 5.12 (b). By injecting a narrow reference pulse into the oscillator, the oscillator output frequency will be locked to N $\times$ f_{REF}. The injection technique offers much wider loop bandwidth compared with

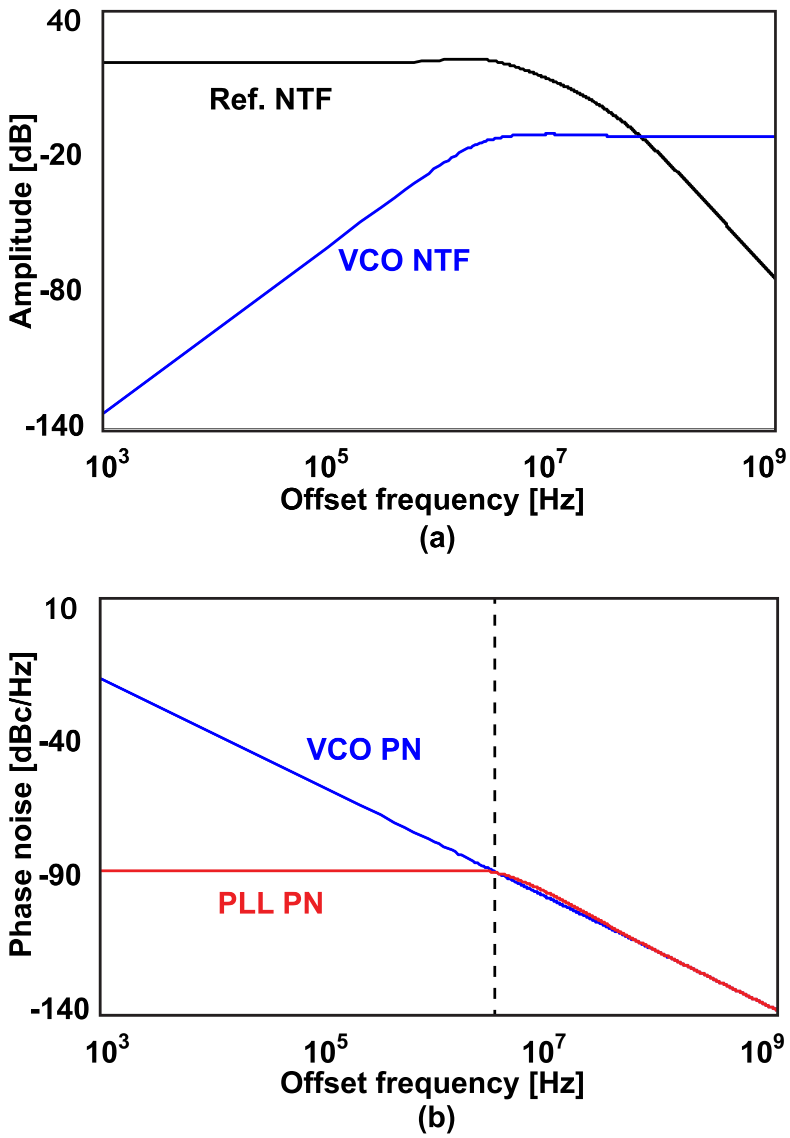

Figure 5.13: (a) Noise transfer functions of reference referred noise and VCO noise. (b) Phase noise of PLL with a low power VCO.

that of conventional PLL [164–166], as shown in Fig. 5.14. Thus, even with a low power VCO, the phase noise of output may not be limited the VCO phase noise.

However, one big issue for the IL-VCO is the large reference spur. It is caused by the phase mismatch between the injection pulse phase and the oscillation free-running phase, as shown in Fig. 5.15 (a). From the frequency domain, the reference spur is produced when the free-running frequency of VCO is not equal to the N$\times f_{\mathrm{ref}}$ (N is the desired frequency multiplication number of IL-VCO). So, whenever the injection happens, there is always a phase offset between the injection phase and the VCO free-running phase before

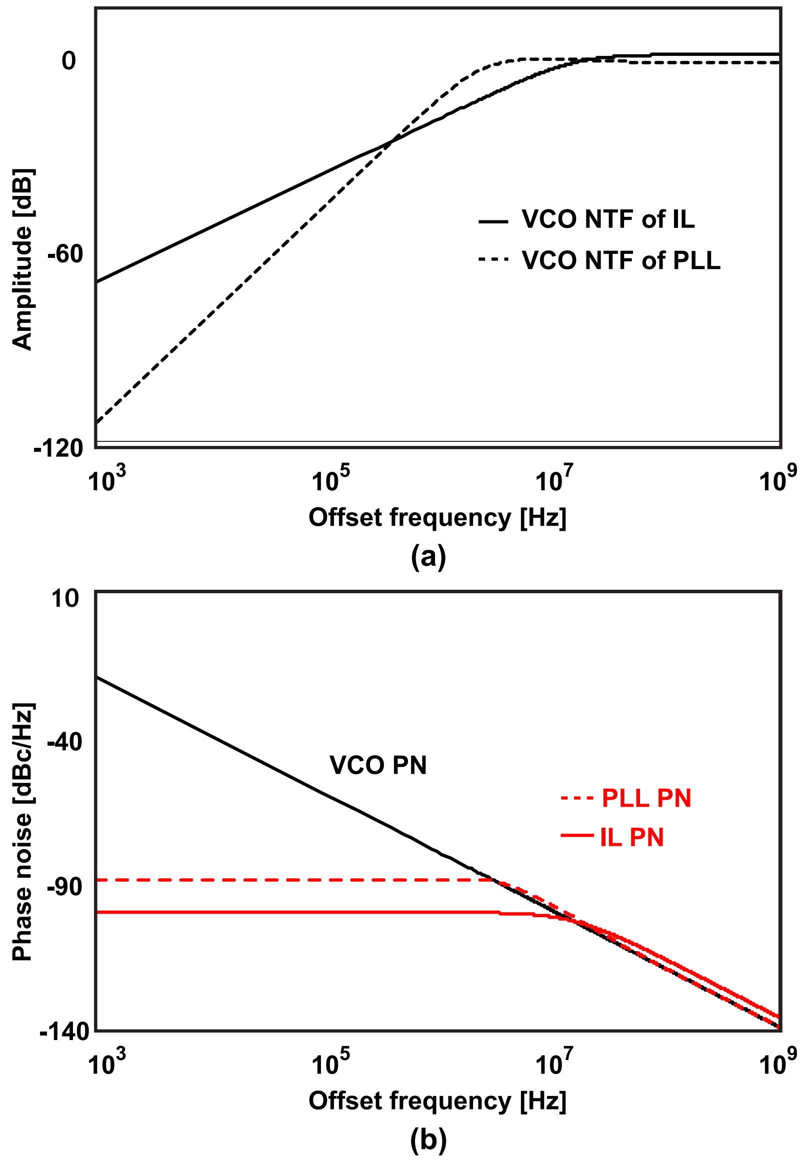

Figure 5.14: (a) VCO noise transfer functions of injection locked (IL) VCO and PLL. (b) phase noise of ILVCO and PLL.

the injection strongly aligns them. After the injection, the phase error begins to increase from zero when the injection is not active since the VCO free-running frequency is not equal to N×f_{ref}. Even 10^{-1} ppm frequency error would lead to a reference spur of -60 dBc, as shown in Fig. 5.15 (b). Thus, a very fine frequency tracking loop is required for IL-VCO. Besides, if the frequency error is too large, the output frequency of VCO will not be locked to N×f_{ref}. The locking range of IL-PLL is determined by the injection current and is usually quite narrow compared with the frequency variation due to the process, voltage

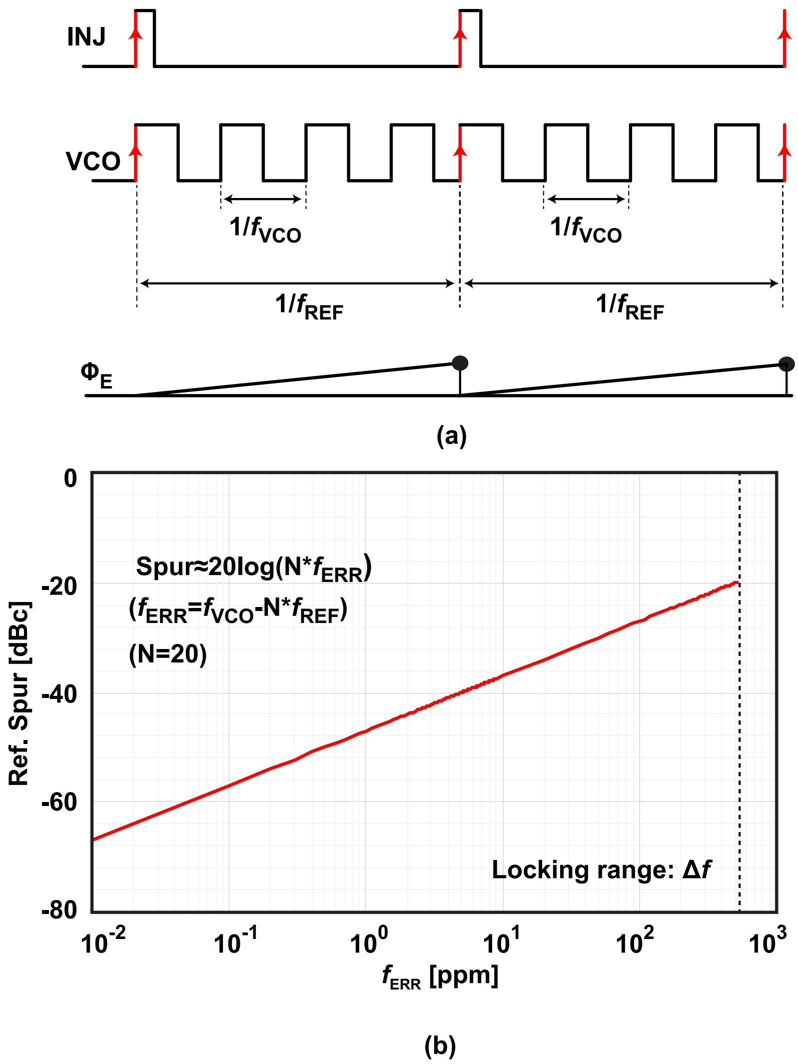

Figure 5.15: (a) The cause of reference spur in the ILPLL. (b) Reference spur versus the frequency error.

and temperature variations (PVT). Therefore, for both reference spur performance and robustness, it is necessary to have an additional loop to finely track the VCO free-running frequency. Various calibrating methods have been developed [167–172], but each of them has some limitations like the overhead of power consumption and area or the residual error.

In this work, an injection time self-alignment method is adopted, as shown in Fig. 5.16 (a). The injection pulse is used to inject both the VCO and the sub-sampling phase detector (SSPD). The VCO free-running frequency is tracked by the SSPD, while the injection phase is self-aligned with the VCO free-running phase since the same edge is used to both align the VCO and enable the sampling of SSPD, as shown in Fig. 5.16 (b).

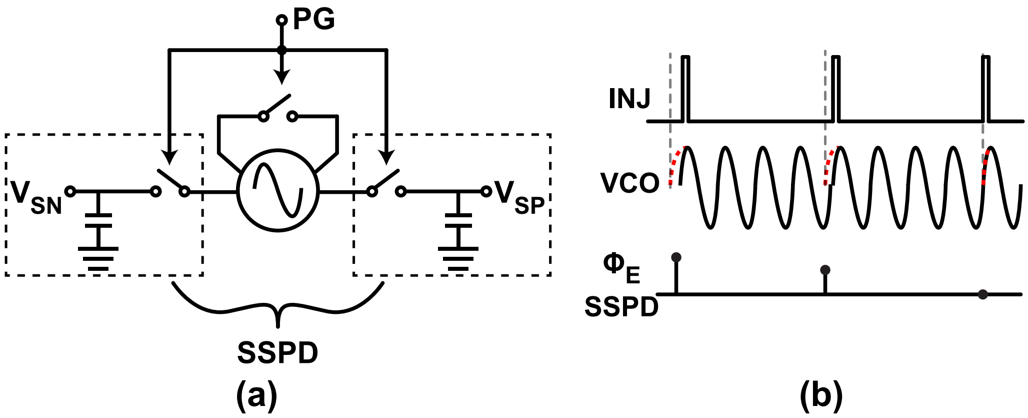

Figure 5.16: (a) Injection time self-alignment method. (b) Related waveform.

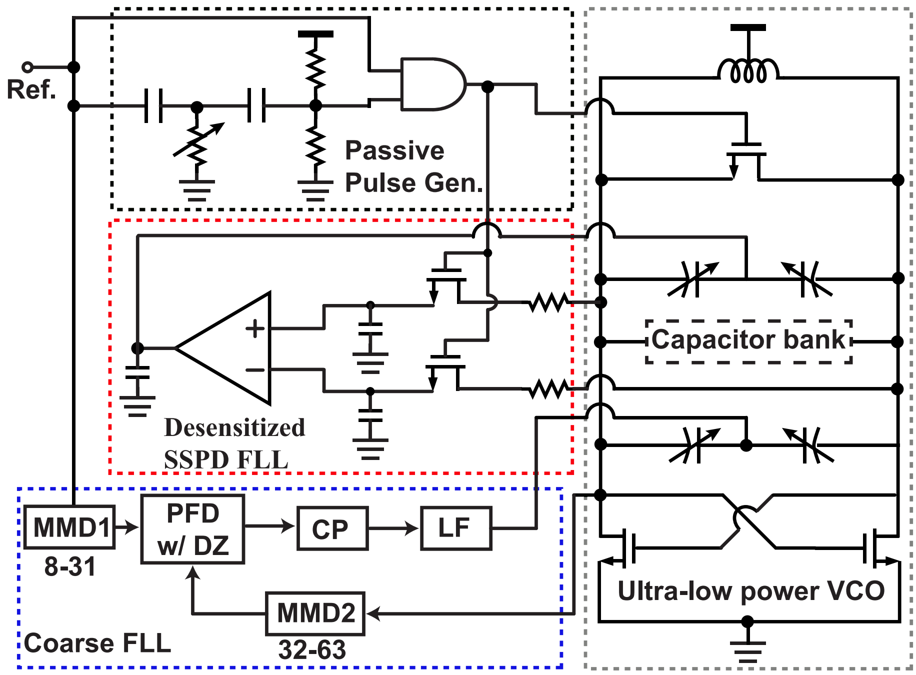

Figure 5.17: Proposed ILPLL architecture.

Figure 5.17 shows the proposed ILPLL architecture. An RC phase shifter based pulse generator is utilized to maintain the signal purity of the reference clock with low power consumption. Compared with conventional digital pulse generator, this passive pulse generator could achieve better phase noise with less power consumption, especially when the programmable delay time is required. A sampling phase detector [173] has been proposed for mitigating the mismatch between the free-running frequency and the desired harmonic of injection frequency. In this work, a desensitized sub-sampling phase detector (DSSPD)

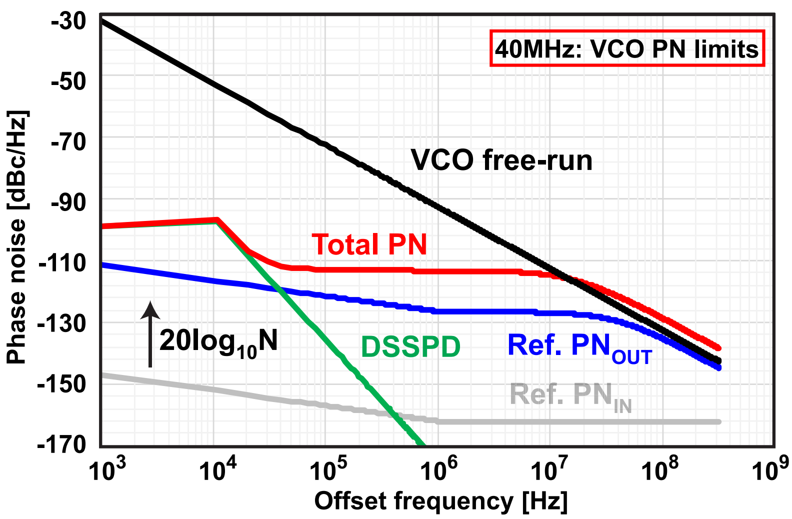

Figure 5.18: Phase noise analysis when the reference frequency is 40 MHz.

based frequency tracking loop (FLL) is introduced to minimize the reference spur by inserting an additional 5 kΩ between the VCO output and the SSPD. A subthreshold biased class-D LC-VCO is designed with 120 μW power consumption as the local oscillator, which achieves more than 20 dB better phase noise as compared with ring oscillators. As the oscillation amplitude of class-D VCO can be three times higher than the VCO supply voltage, stable operation of the standard-cell based MMD in the coarse FLL can be ensured even with 0.14 V supply for the VCO. In the ILPLL, the coarse FLL selects the coarse frequency bank and sets the VCO output frequency close to N^{th} harmonic of the reference frequency f_{ref}. The coarse FLL is then automatically disabled by the dead-zone (DZ) PFD, and the injection pulse generator achieves precise locking of the oscillator phase.

5.2.2 Phase noise analysis and fair FoM

Figures 5.18 and 5.19 show the detailed phase noise analysis of the ILPLL. The injection lock offers a very wide noise folding bandwidth for VCO phase noise, and the bandwidth f_{inj} is determined by the reference frequency f_{ref}. The bandwidth for IL-VCO is given by [174]:

$$f_{inj} = \frac{f_{ref}}{\pi}\sqrt{\frac{3N}{2(N-1)}} \tag{5.35}$$

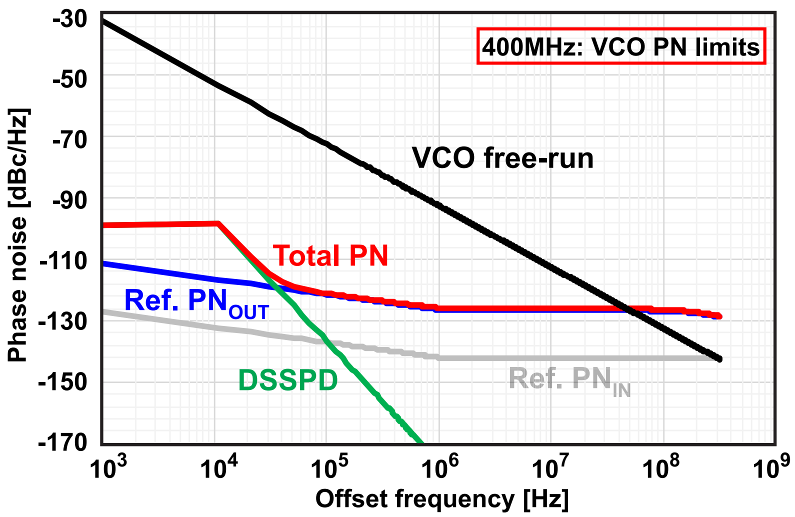

Figure 5.19: Phase noise analysis when the reference frequency is 400 MHz.

where N is the desired frequency multiplication number. Equation (5.35) assumes the ideal alignment of injection. In a practical case, the phase error θ_e between the injection reference phase and the VCO free phase is shifted by $\beta\theta_e$ after the realignment of VCO [166]. The value of β ranges from 0 to 1. Normally, we assume β is around 0.5 to 0.8. But in the following analysis, we assume the injection is ideal, where the β is equal to 1.

The VCO phase noise experiences 1st-order high pass filter (HPF) by injection, and DSSPD further cancels low offset-frequency components. From Eq. (5.35), we realize that the loop bandwidth is proportional to reference frequency. And larger bandwidth could suppress more VCO phase noise. Thus, here we give two cases for the phase noise analysis. One is the low reference case, the other one is a high reference case. Figures 5.18 shows the 40 MHz case and Fig. 5.19 shows the 400 MHz case. For both cases, the following simulation conditions are assumed: i) the VCO output frequency is 2.4 GHz; ii) the reference jitter is 15 fs; iii) the VCO jitter is 70 ps. The reference phase noise is degraded by $20\log_{10} N$ when converts to the VCO output. In the 40 MHz reference case, due to the narrow loop bandwidth of the SSPD loop, the phase noise of DSSPD is largely filtered beyond the loop bandwidth. For the large range, the total phase noise is limited by the VCO phase noise. Therefore, in the low reference case, a high-performance VCO is required to achieve a high figure of merit (FoM) for the IL-PLL. In the high reference case, the in-band phase noise is still dominated by the DSSPD phase noise. However, for the large in-band and out-band, the reference phase noise after converting becomes the limiting factor. Thus, for a high reference frequency, the reference phase noise should be maintained to achieve low jitter performance.

From the above analysis, it is obvious that the reference frequency has a large impact on the jitter performance of ILPLL. Therefore, it would be difficult to adopt the conventional jitter and power FoM to evaluate the performance of ILPLL. According to the following theoretical calculation, the integrated jitter of ILPLL is inversely proportional to the square root of f_{ref} while it also suffers from the reference noise as a lower limit.

The phase noise of VCO can be expressed in term of $\mathrm{FoM}_{\mathrm{VCO}}$ as follows:

$$\mathcal{L}_{\mathrm{VCO}} = \frac{10^{\frac{\mathrm{FoM}_{\mathrm{VCO}}}{10}}}{(\frac{f}{f_{\mathrm{OUT}}})^2 \cdot \frac{\mathrm{P}_{\mathrm{dc,VCO}}}{1\mathrm{mW}}} \tag{5.36}$$

where f_{VCO} is the VCO output frequency, $\mathrm{P}_{\mathrm{dc,VCO}}$ is the dc power consumption of VCO. The loop bandwidth of ILPLL can be expressed by Eq. 5.35. Thus, if assuming the reference phase noise is excellent, the phase noise of ILPLL can be calculated from the suppressed VCO phase noise as follows:

$$\mathcal{L}_{\mathrm{inj}}(f) = \mathcal{L}_{\mathrm{VCO}}(f) \cdot \frac{2N-1}{N} \cdot \frac{\left(\frac{f}{f_{\mathrm{inj}}}\right)^2}{1+\left(\frac{f}{f_{\mathrm{inj}}}\right)^2} \tag{5.37}$$

Then jitter is expressed as:

$$\sigma_{\mathrm{t}}^2 = \frac{\int_{-\infty}^{\infty} \mathcal{L}(f)df}{(2\pi f_{\mathrm{OUT}})^2} = 10^{\frac{\mathrm{FoM}_{\mathrm{VCO}}}{10}} \cdot \frac{1\mathrm{mW}}{P_{\mathrm{dc,VCO}}} \cdot \frac{1}{f_{\mathrm{ref}}} \cdot \frac{2N-1}{2N} \cdot \sqrt{\frac{N-1}{6N}} \tag{5.38}$$

The conventional jitter and power FoM ($\mathrm{FoM}_{\mathrm{JP}}$) of PLL is defined as:

$$\mathrm{FoM}_{\mathrm{JP}} = 10\log\left\{\frac{\sigma_{\mathrm{t}}^2}{(1\mathrm{s})^2} \cdot \frac{\mathrm{P}_{\mathrm{dc,PLL}}}{1\mathrm{mW}}\right\} \tag{5.39}$$

By replacing Eq. (5.38) into Eq. (5.39), the conventional jitter and power FoM can be expressed as:

$$\mathrm{FoM}_{\mathrm{JP,IL}} = 10\log\left\{10^{\frac{\mathrm{FoM}_{\mathrm{VCO}}}{10}} \cdot \frac{\mathrm{P}_{\mathrm{dc,IL}}}{\mathrm{P}_{\mathrm{dc,VCO}}} \cdot \frac{1}{f_{\mathrm{ref}}} \cdot \frac{2N-1}{2N} \sqrt{\frac{N-1}{6N}}\right\} \tag{5.40}$$

If we assume the power consumption of ILPLL is approximately equal to the power consumption of VCO and N is large enough, the above equation can be further simplified as

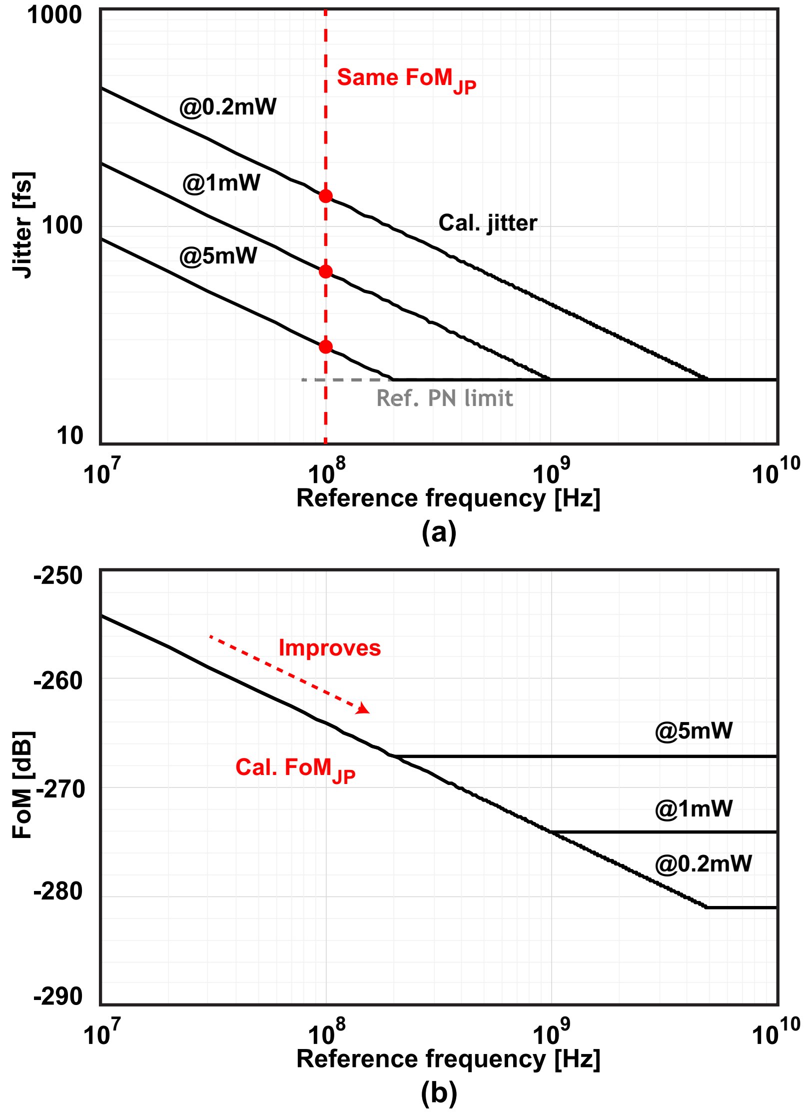

Figure 5.20: (a) ILPLL jitter performance versus the reference frequency. (b) $\mathrm{FoM_{JP}}$ performance versus the reference frequency.

follows:

$$\mathrm{FoM_{JP,IL}} \approx \mathrm{FoM_{VCO}} - 10\log f_{\mathrm{ref}} - 3.89 \tag{5.41}$$

From Eq. (5.41), it is clear that the $\mathrm{FoM_{JP,IL}}$ has a strong relationship with the reference frequency, which means that the conventional $\mathrm{FoM_{JP,IL}}$ improves if the reference frequency increases. Thus, the conventional $\mathrm{FoM_{JP,IL}}$ is not applicable to evaluate the circuit performance of the integer-N PLL, especially for the ILPLL. In order to further study the relationship between the $\mathrm{FoM_{JP,IL}}$ and reference frequency, both jitter and $\mathrm{FoM_{JP,IL}}$

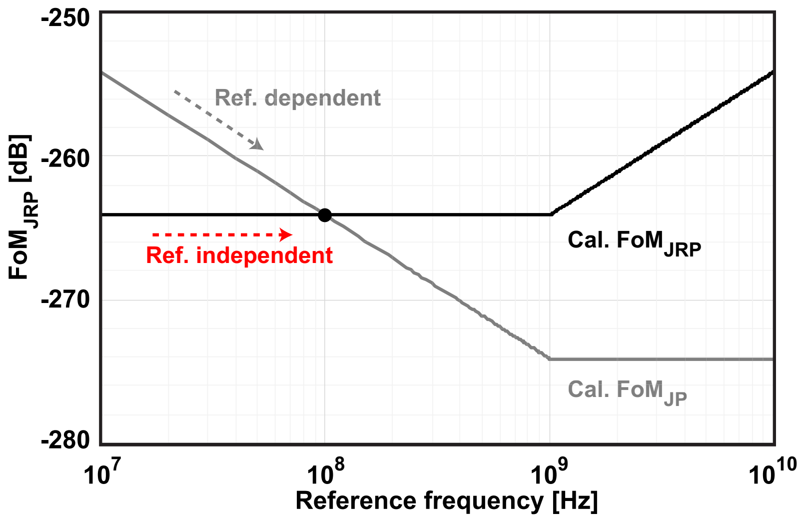

Figure 5.21: $\mathrm{FoM_{JRP}}$ performance versus the reference frequency.

performance of an ideal ILPLL are plotted versus the reference frequency. The jitter performance of ILPLL improves as the reference frequency increases until it reaches the limit of reference phase noise, as shown in Fig. 5.20 (a). Also higher power consumption could result in a better jitter performance. But the $\mathrm{FoM_{JP,IL}}$ at the same reference frequency is same. Figure 5.20 (b) shows the calculated jitter and power $\mathrm{FoM_{JP,IL}}$. The $\mathrm{FoM_{JP,IL}}$ keeps decreasing until it becomes flat, which is set by the power consumption.

From previous analysis, we could see that for the conventional fractional-N PLL, the $\mathrm{FoM_{JP}}$ works very well as a fair benchmark indicator. But when it comes to integer-N PLL, especially for the ILPLL, the $\mathrm{FoM_{JP,IL}}$ fails to serve as a fair benchmark indictor. This conventional $\mathrm{FoM_{JP,IL}}$ could be abused for performance comparison. Thus, a fairer FoM should remove the impact of reference frequency. Here we define a new FoM, and call it as jitter, reference and power FoM ($\mathrm{FoM_{JRP}}$). It is defined as follows:

$$\mathrm{FoM_{JRP}} = 10\log\left\{\frac{\sigma_t^2}{(1\mathrm{s})^2}\cdot\frac{\mathrm{P_{dc,PLL}}}{1\mathrm{mW}}\cdot\frac{f_{\mathrm{ref}}}{100\mathrm{MHz}}\right\} \tag{5.42}$$

The reason why we use 100 MHz as a normalized reference frequency is because that the typical upper frequency limit of crystal oscillator is less than 100 MHz. The calculated new $\mathrm{FoM_{JRP}}$ of an ideal ILPLL versus reference frequency is plotted in Fig. 5.21. The new $\mathrm{FoM_{JRP}}$ first stays flat as the reference frequency increases and then it goes up determined by the power consumption and reference jitter. The $\mathrm{FoM_{JRP}}$ is adopted in this work for the comparison of PLL performance. Actually the new $\mathrm{FoM_{JRP}}$ causes much severer degradation in terms of number value, but it can fairly reflect the circuit performance.

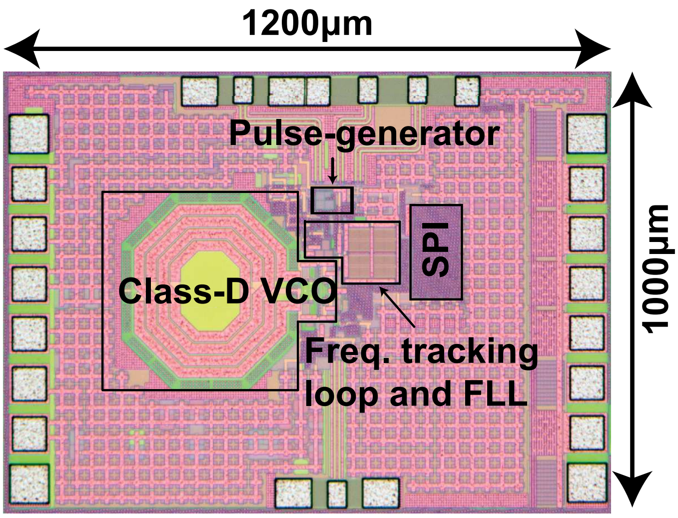

Figure 5.22: Chip micrograph.

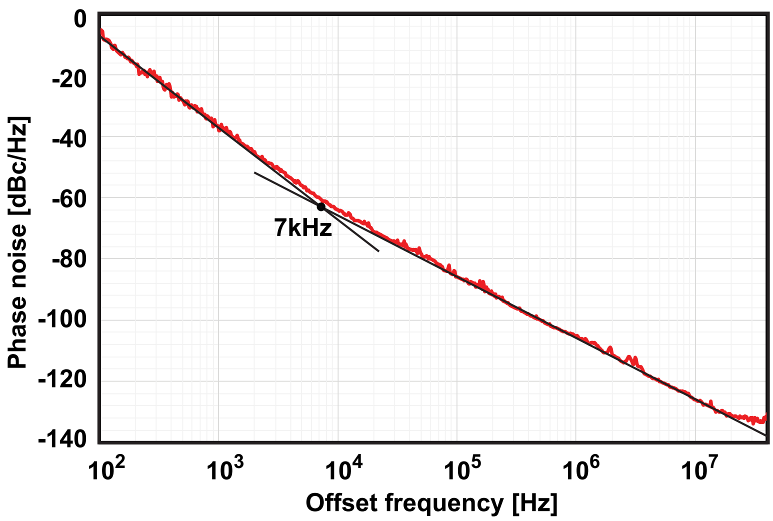

Figure 5.23: Measured phase noise of class-D VCO

5.2.3 Implementation and evaluation

The proposed ILPLL is implemented in a standard CMOS 65 nm technology. The chip micrograph is shown in Fig. 5.22. The active area of this ILPLL is only 0.25 μm^2. The ILPLL supports injection ratio ranging from 3-24, and the frequency range is from 2.2 GHz to 2.6 GHz. The power consumption is from 0.17 mW to 0.2 mW depending on the reference frequency. The measured phase noise of VCO is shown in Fig. 5.23. By optimizing the size of the cross-coupled transistors and the K_{VCO} of the LC-tank, the flicker corner of the VCO is only 7 kHz. A low flicker corner is beneficial for low in-

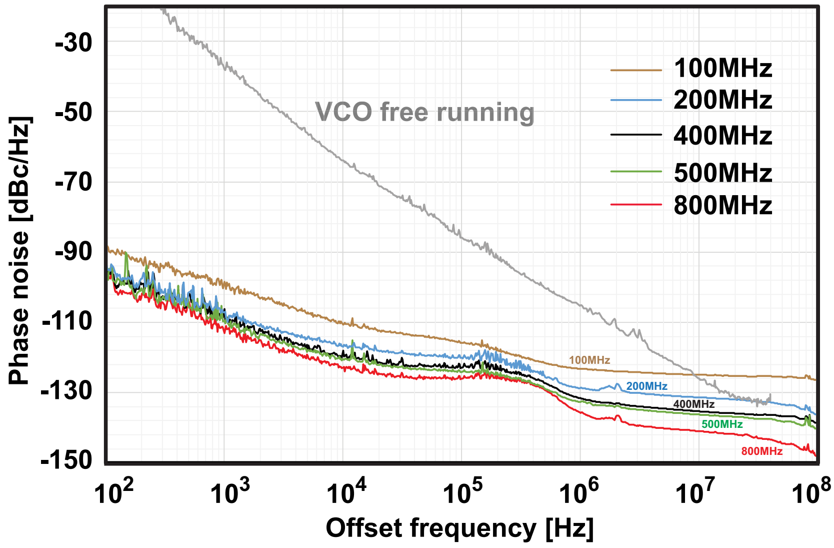

Figure 5.24: Measured phase noise of ILPLL at different reference frequencies.

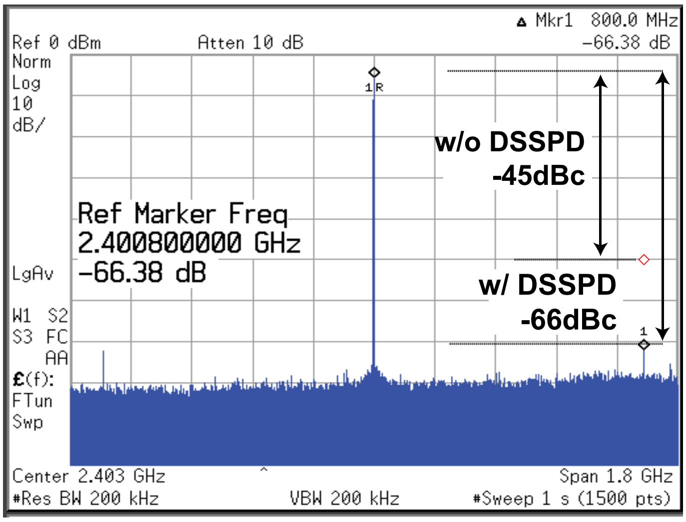

Figure 5.25: Measured reference spur of ILPLL.

band phase noise for IL-VCO since the injection only provides 1st noise filtering for the VCO, as shown in Fig. 5.14. The measured phase noise of ILPLL is shown in Fig. 5.24. We tested the ILPLL performance by using difference reference frequencies. It achieves 60 fs to 298 fs integrated jitter for the different reference frequencies. The reference spur of ILPLL is also measured to verify the effectiveness of the frequency tracking loop, as shown in Fig. 5.25. When the FTL is not enabled, the reference spur is -45 dBc. The reference spur improves to -66.5 dBc when the FTL is enabled.

In order to verify our FoM theory. The measured jitter performance of reference and

Table 5.3: Comparison of state-of-the-art PLLs.

	[175]	[176]	[177]	[178]	[179]	This work
Architecture	SSPLL	RSPLL	SSPLL	AMASS PLL	SSPLL	ILPLL
Technology [nm]	180	65	65	65	40	65
Frequency range [GHz]	2.21	2.05-2.55	5	2.4	12-16	2.2-2.6
Reference frequency [dBc]	55.25	50	100	100	200	100-800
Reference spur [MHz]	-56	-67	-64.1	-66.6	-64.6	-66.5
RMS jitter [fs]	160	110	185.3	174.2	56.4	60-298
Power consumption [mW]	2.5	3.7	1.1	0.93	7.2	0.17-0.2
FoM_{JP} [dB]	-251.9	-253.5	-254.2	-255.5	-256.4	-271.4
FoM_{JRP} [dB]	-254.5	-256.5	-254.2	-255.5	-253.4	-262.4

ILPLL is shown in Fig. 5.26 (a) with reference frequency ranging from 100 MHz-to-800 MHz. The reference jitter almost stays flat when the reference frequency increases. However, the ILPLL jitter performance keeps improving as the reference frequency increases since more VCO noise is getting filtered. Figure 5.26 (b) plots the both FoM_{JP} and FoM_{JRP} from the measurement results. From Fig. 5.26, it is clear that the FoM_{JP} of ILPLL cannot accurately reflect the circuit performance. The measured FoM_{JP} follows an almost linear relationship with the reference frequency. The measured FoM_{JRP} stays flot when the reference frequency increases. However, at high frequencies, the FoM_{JRP} improves. This is mainly caused by the limited jitter integration range of the phase noise measurement equipment.

Table 5.3 shows a performance comparison of the proposed ILPLL together with the other state-of-arts [175–179]. Thanks to the ultra-low power design of VCO and pulse generator, the total power consumption of the ILPLL is only 0.2 mW. The low phase noise passive pulse generator and narrow bandwidth of DSSPD ensure the low jitter performance. The adopted self-alignment injection method also effectively reduces the reference spur to below -66.5 dBc. The ILPLL achieves more than 15 dB improvement of FoM_{JP} with 800 MHz reference frequency. Even in FoM_{JRP}, -261 dB has been achieved.

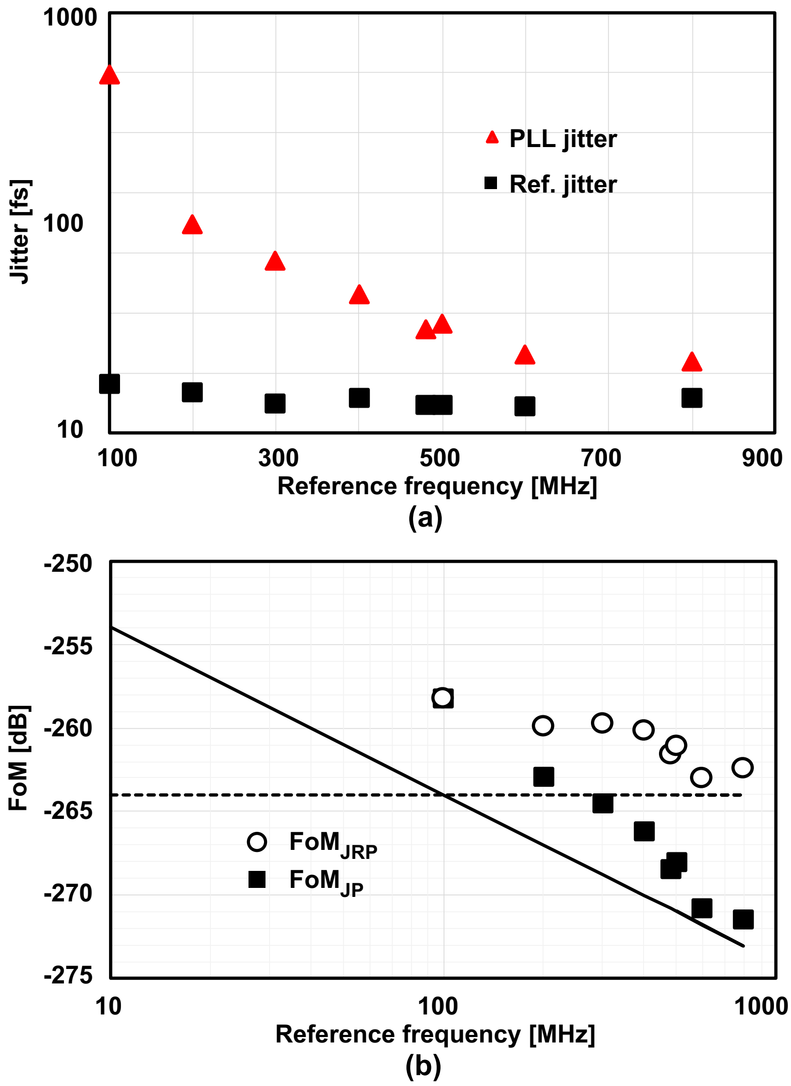

Figure 5.26: (a) Measured jitter performance versus the reference frequency. (b) Measured FoM performance versus the reference frequency.

Chapter 6

Conclusion and Future Work

The present study introduces one ultra-low-power atomic clock, which reduces power consumption below 60 mW by a newly designed suspended architecture of the quantum physical package and power-efficient RF circuits. The short-term frequency stability is maintained by low AM and PM noise probing and locking circuits, while the long-term frequency stability is ensured by additional dedicated stable control loops. Thanks to the robust VCSEL and atom cell package, stable and long-term operation has been observed. The proposed ULPAC will hopefully continue to operate while satisfying the required performance. The volume of the prototype is reduced to 15 cm^3 by using advanced package technology for the quantum physical package and SoC integration. Such a tiny and highly stable atomic clock could be used in the LEO smallsat constellation for accurate timing synchronization. The proposed ULPAC can also be adopted in GPS-denied environments to maintain navigation or improve the performance of high-speed data-links, etc.

For the next-generation ULPAC, the volume is aimed to reduce by ten times, while the power consumption is required to further reduce to below 25 mW. The MEMS technology can be applied to the quantum physical package, which can potentially minimize the size to below 1 cm^3 [68, 108, 109] and reduce the power consumption of the quantum physical package as well.

Also the duty-cycling operation can be applied to further reduce the power consumption. The principle of duty-cycling operation relies on the factor that the short-term stability of VCXO could be better or equivalent to that of compact quantum physical package, as indicated by Fig. 4.7, while the long-term frequency stability is ensured by the atomic reference.

This chapter introduces some advanced quantum technologies that can be adopted in the next generation ULPAC to further improve the frequency stability performance.

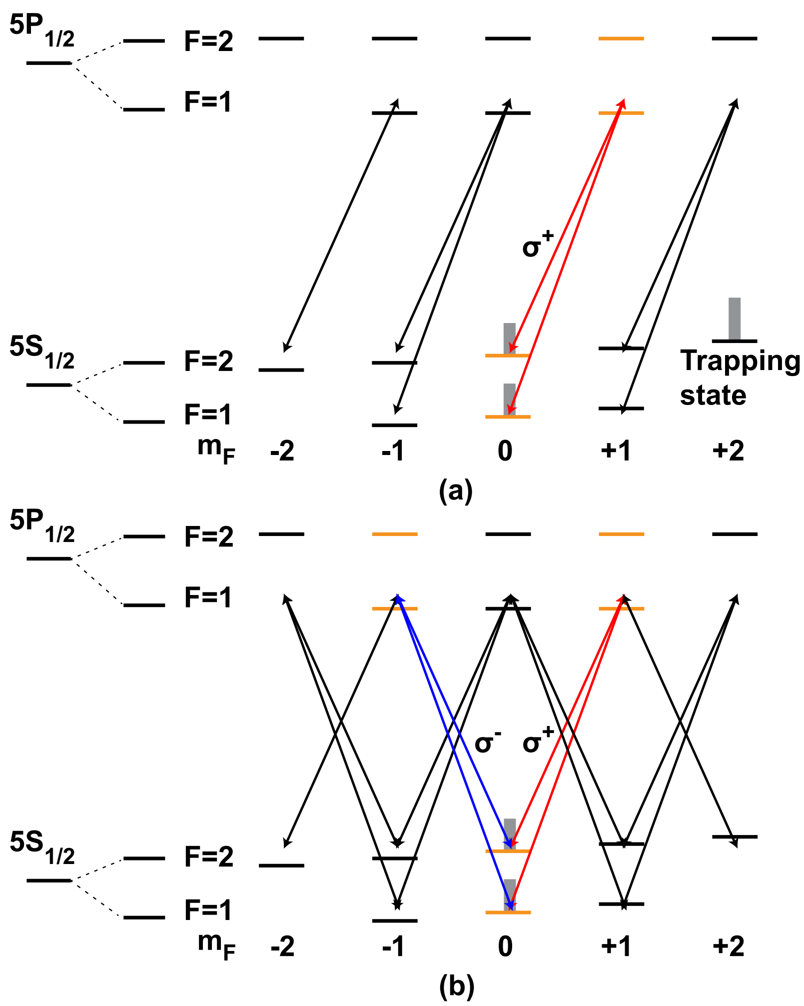

Figure 6.1: Atomic levels of Rb ^{87}D1 line (a) single Λ resonance. (b) double Λ resonance case [9].

6.1 Quantum Technologies for Better Frequency Stability

By using the above mentioned low power circuit techniques, duty-cycling operation and MEMS technologies, the power consumption of quantum physical package and frequency probing loop can be much reduced for mobile and portable applications. However, so far there is still considerable frequency stability degradation for the compact atomic clock compared with the conventional high-performance atomic clock. In this section, several quantum principles previously only adopted in the bulky atomic clock are introduced and are considered to be employed in the next-generation high-performance compact atomic clock.

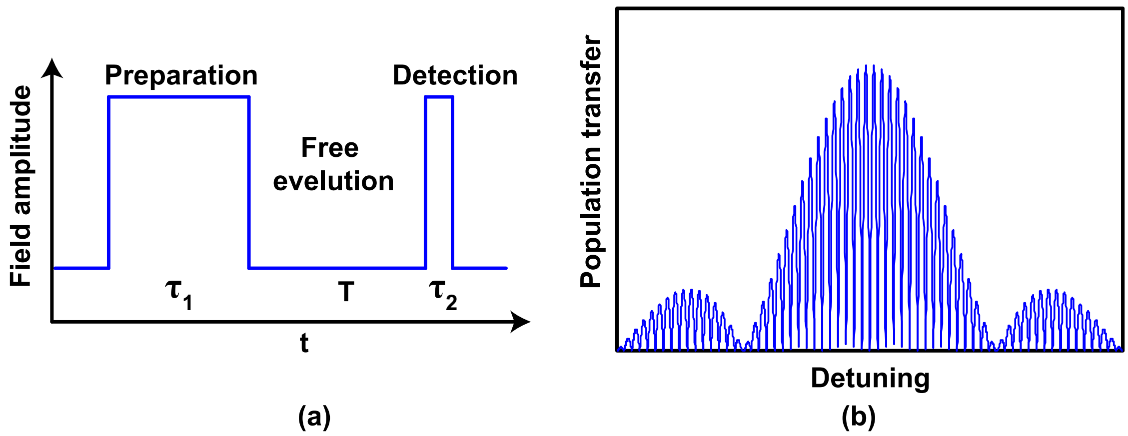

Figure 6.2: (a) Raman-Ramsey pulse sequence with duration τ_1 for the first pulse and τ_2 for the second pulse. T is the free evolution time of the Raman coherence between the two pulses [10]. (b) Detected population and linewidth.

6.1.1 Improving CPT contrast

As mentioned in Chapter 2, the Zeeman sub-levels open the Λ scheme for CPT resonance and provide trapping states for the population, which degrades the resonance contrast, as shown in Fig. 6.1 (a).

Several approaches have been suggested to avoid the effect of trapping levels including push-pull optical pumping [180], counter-propagating waves [181], or co-linear, so-called line-per-lin polarization, laser beams [10]. Figure 6.1 (b) shows the push-pull method. Instead of using only left or right circularly polarized light, the double-Λ scheme using both left and right transitions simultaneously can be adopted to increase the contrast of the CPT resonance by removing the trapping state [9]. However, as indicated by Fig. 6.1 (b), four light fields are required for the push-pull method. If adopting the RF modulation techniques, two lasers with coherent phases are needed, which complicates the system design and adds more power consumption. But if the frequency stability performance is improved more than 10 times, the additional cost would make sense for the compact atomic clock.

Also the Ramsey spectroscopy has advantages over continuous excitation in reducing light-shift and power broadening effects [10, 182, 183]. The time-separated Ramsey method splits the continuous excitation into periodical excitations, as shown in Fig. 6.2 (a). The first pulse excites the ground-state coherence in the atoms, which is followed by a precession in the dark. The coherence is then measured during a second pulse. The light pulse durations are controlled by an acousto-optic modulation. The detection technique allows a real-time measurement of the optical coherence during the two pulses, without perturbing the coherence process. Unlike the continuous CPT resonances, where the linewidth broadens linearly with the light power, in the pulse CPT resonance, the width of the Ramsey fringes is determined by the inverse time between pulses [184], as shown in Fig. 6.2 (b).

6.1.2 Laser cooling techniques

As introduced in Chapter 2, the motion of atoms causes frequency shifts and linewidth broadening through the Doppler effect. Some techniques can be adopted to reduce the Doppler broadening and the first-order Doppler shift. The insertion of additional buffer gas can effectively reduce the first-order Doppler shift and narrow the linewidth [101]. However, the second-order Doppler shift still exists. Even though the averaged velocity is zero, the absolute velocity is not altered. And the collision between the inserted buffer gas and atoms introduces additional frequency shift contributors. In ion traps, it was shown that some cooling could be done by means of a light buffer gas of low density. However, the minimum temperature that can be achieved in this case is determined by the environmental temperature, which still results in a relatively large second-order Doppler shift [6].

Historically, the Doppler shift was one of the motivations for cooling techniques are used in high-performance atomic clocks. Figure 6.3 explains the cooling process by means of laser radiation. The atoms are moving toward the light source with a velocity of υ_z. The cooling laser outputs a monochromatic light with a frequency of ν_L, which is slightly lower than the resonance frequency of the atoms. If the condition of $\nu_L(1 + \upsilon_z/c) = \nu_0$ is met, the absorption happens with a momentum transfer of $\Delta P_z = h/\lambda$ from the absorbed photon. Then the atom re-emits a photon by spontaneous emission with equal probability in all directions with a change of momentum by the quantity of $M\Delta\upsilon_z = h/\lambda$. This results in a reduction of the atomic kinetic energy, which means a lower temperature [6, 11].

However, the velocity of the atoms is a continuously varying parameter, which means the Doppler shift as seen by the atoms also changes. One solution is to change the frequency (chirping) of the cooling laser so as to interact with all the atoms in a wide distribution and to stay in resonance with the atoms as they are cooled [185–189]. The chirp-cooling technique is now one of the two standard methods for decelerating beams. The other is "Zeeman cooling", in which a magnetic field gradient is used.

Previous experiments already validated the laser cooling method and successfully reduced the temperature to approximately in the mK range. The atomic clock using the laser cooling technique like the fountain clock achieves the frequency stability in the range of 10^{-17}.

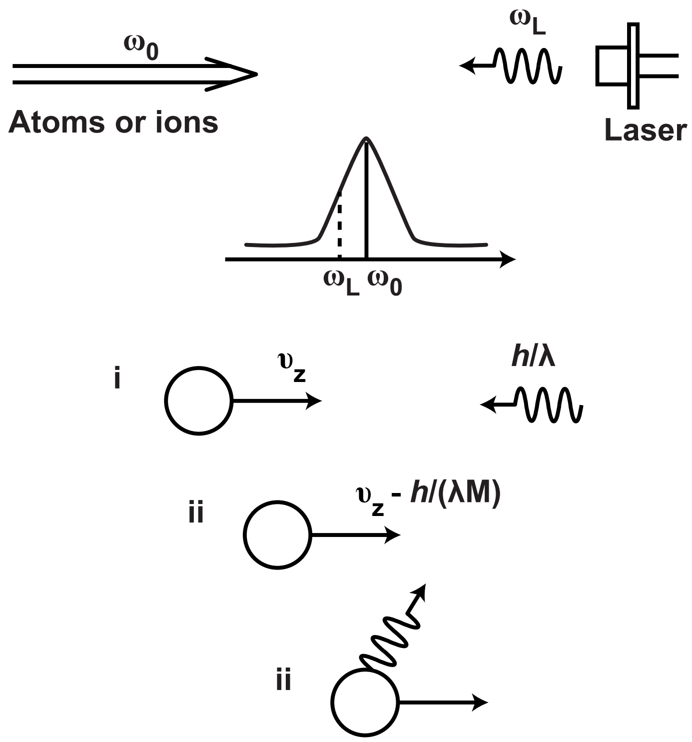

Figure 6.3: Colling process by means of laser radiation [11].

The architecture of the compact atomic clock using the laser cooling technique is similar to the ULPAC system, as shown in Fig. 6.4 (a). However, an additional laser cooling control loop is required to minimize the Doppler shift and linewidth broadening, as shown in Fig. 6.4 (b). The core of the laser cooling loop is the magnetic optical trap (MOT). Same as the vapor cell for ULPAC, the size of MOT determines the volume of the clock. However, simplifying atomic cooling and trapping using microfabrication technology are very challenging [190, 191]. One recent work demonstrated a micro-fabricated grating MOT using atom chip, which enables the integration of laser cooling and trapping into a compact apparatus [192].

By the cooling techniques, the short-term and medium-term frequency stability can be improved by more than one order, to the promising frequency stability of 10^{-13} with a sub-liter package. However, the light fluctuations induced frequency shift will still limit the long-term frequency stability for the compact atomic clock. High-performance coherent laser technology will be the next design challenge for such a system.

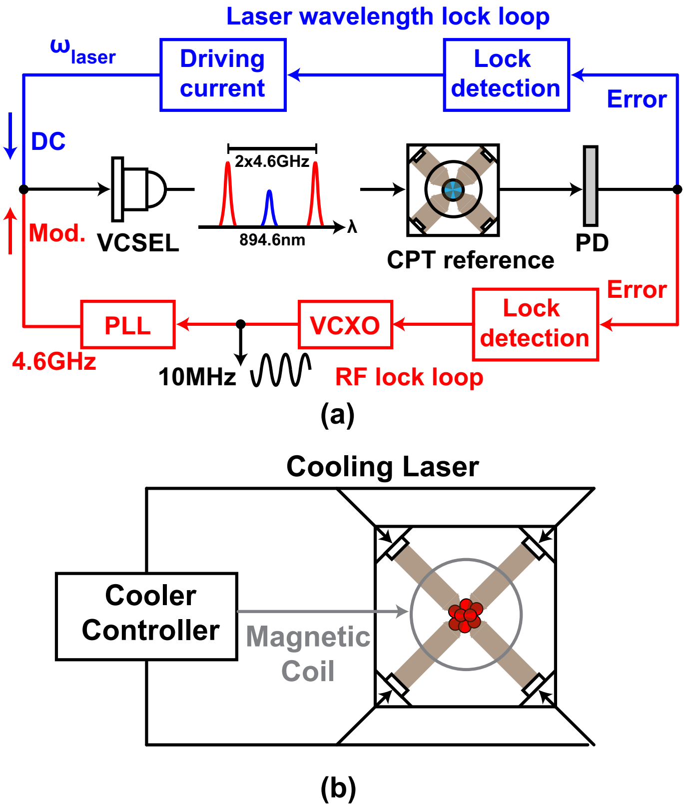

Figure 6.4: (a) Laser cooling based atomic clock architecture. (b) Magnetic optical trap (MOT) based atomic cell.

6.1.3 Optical transitions

As indicated by Fig. 1.11, the optical atomic clocks outperform the microwave atomic clock recently. Laboratory optical atomic clocks already achieved remarkable accuracy (now counted to 18 digits or more) [193]. And it is expected that the optical atomic will eventually replace microwave clocks in global timekeeping, navigation and the definition of the SI second [194]. Different from the microwave atomic clock, the optical atomic clock relies on high-frequency, narrow-linewidth optical transitions to stabilize a clock laser [63]. Following the Eq. (2.15) for the fractional frequency error of CPT based atomic clock, the fractional frequency error of optical atomic clock can be written as:

$$\delta y_{\mathrm{e}} = \left(\frac{\delta f}{f_0}\right)_{\mathrm{e}} = \frac{\delta S}{f_0(dS/df)} \tag{6.1}$$

where f_0 is the resonance frequency of optical atomic clock. Since the f_0 for optical atomic clock is in the range of terahertz, the qualify factor of optical atomic clock outperform their microwave counterparts by several orders of magnitude, which results a better sta-

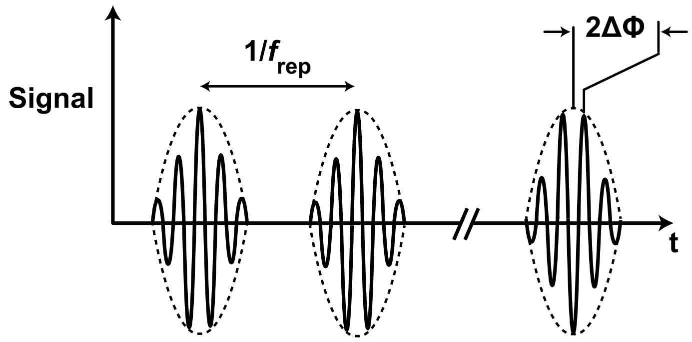

Figure 6.5: Optical combs output [12].

bility frequency.

However, the terahertz frequency transition is typically higher than the maximum operating frequency of electronic detectors, which was one of initial obstacles for implementation of the optical atomic clocks. Within the past two decades, the optical frequency comb technology has made it quite straighforward to probe optical frequency [195–200].

In the time domain, the optical combs generate femtosecond pulse-width envelopes separated in time by $1/f_{\text{rep}}$, as shown in Fig. 6.5. By Fourier transformation, for each tooth in the comb, a particular single-frequency mode, is separated from it neighbor by f_{rep}. The relative carrier-envelop phase in the time domain is related to the offset frequency f_{CEO} in the frequency domain. f_{CEO} is given by the frequency of one mode of the comb modulo f_{rep}. Measurement of one unknown atomic reference frequency can be done by measuring the heterodyne beat between the frequency source and the frequency comb [28]:

$$\nu_{\text{opt}} = \mathrm{M}f_{\text{rep}} + f_{\text{CEO}} + f_{\text{beat}} \tag{6.2}$$

where M is the mode number of optical frequency combs. By stabilizing the f_{CEO} and f_{rep} to a known frequency, the mode frequency can be obtained as well.

One additional implementation challenge for the compact atomic clock is the on-chip stable laser that coupling the ground-excited state of atom. One recent pioneering work undergoing by NIST demonstrates the feasibility of using a distributed Bragg reflector (DBR) laser and a micro-resonator frequency comb system for optical frequency division [13, 63]. As shown in Fig. 6.6, this architecture employs two interlocked micro combs: a high repetition rate used for self-referencing and a narrow-band comb used to produce an electronically detectable microwave output. A DBR laser is adopted that is referenced to the two-photo transition in ^{8}7Rb in a micro-fabricated vapor cell. The 1 THz repetition rate, dissipative Kerr-soliton (DKS) frequency comb is generated by coupling

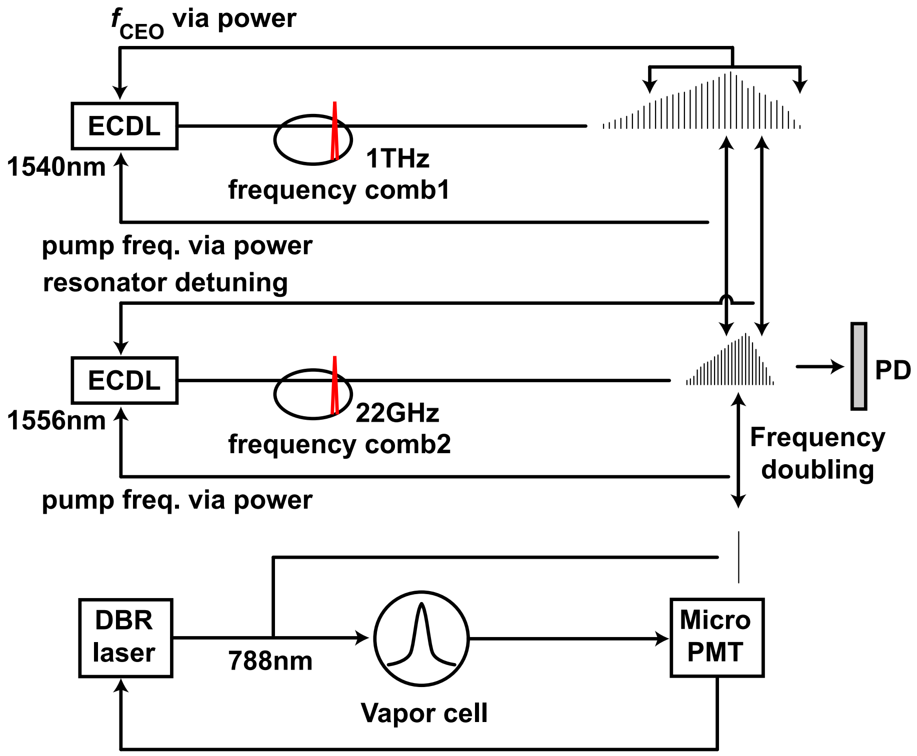

Figure 6.6: Schematic of photonic optical atomic clock by NIST [13].

the power of pump light from an external cavity diode laser (ECDL) into a Si_3N_4 microresonator. And it is used for coarse optical division. The independently 22 GHz repetition rate, DSK comb is generated by coupling power of light pump from a 1.556 µm ECDL. The two combs are interlocked, and the silica comb is used as a finely spaced ruler to measure the repetition rate of the coarse comb. The output of the clock is a 22 GHz optical pulse train that is phase stabilized to the Rb two-photon transition. This work achieves an Allan deviation of 1.7×10^{-13} at the averaging time of 4000 s, which is approximately 10 times better than the stability performance of ULPAC. The total power consumption of this compact optical atomic is 275 mW. In the future, the stability of chip-scaled optical atomic clocks may be improved with low-noise lasers and its size can be reduced with more compact optical and electronic integration.

6.2 Conclusion

The power consumption of converter, quantum physical package, and RF circuits are the major power-hungry components in the ULPAC prototype, as shown in Fig. 4.18. The power consumption of converter can be largely reduced by a customed design using advanced CMOS technology, while the power of quantum physical package can be well reduced to below 10 mW by silicon-based MEMS technology. The circuit design techniques demonstrated in Chapter 5 enable the ultra-low-power design of the frequency probing and locking loop. Thus, below 25 mW power consumption of next-generation ULPAC is feasible in the near future.

The CPT principle enables an atomic resonance in the microwave region, which relaxes the requirement on the laser technology and lends a convenient implementation for frequency probing and locking circuits as well. However, the buffer gas shift degrades the long-term frequency stability considerably. The laser cooling technique adopted in high-performance atomic clocks like the fountain clock could reduce the Doppler shift without inducing the buffer gas shift. One more promising direction will be the optical transition, which has been becoming more and more popular in building a highly stable atomic clock since the beginning of this century. This can be attributed to the factor that the optical transition has a higher quality factor and narrower linewidth. With these advanced quantum technologies, the long-term frequency stability can be improved to below 10^{-13}.

These quantum technologies could be combined with the CMOS technology to build the next ultra-low-power and highly stable atomic clock for portable and mobile applications, which could benefit both the secular and scientific purposes of humankind. From the aspects of devices, the micro-fabricated MoT, optical combs and highly coherent lasers will be the key technologies. In terms of the CMOS circuits, ultra-low power and low electrical noise frequency probing and locking loop is required.

Bibliography

[1] S. A. Diddams, J. C. Bergquist, S. R. Jefferts, and C. W. Oates, "Standards of time and frequency at the outset of the 21st century," *Science*, vol. 306, no. 5700, pp. 1318–1324, Nov. 2004.

[2] A. Takamizawa, S. Yanagimachi, T. Tanabe, K. Hagimoto, I. Hirano, K. Watabe, T. Ikegami, and J. G. Hartnett, "Preliminary evaluation of the cesium fountain primary frequency standard NMIJ-F2," *IEEE Transactions on Instrumentation and Measurement*, vol. 64, no. 9, pp. 2504–2512, Sept. 2015.

[3] R. Lutwak, D. Emmons, W. Riley, and R. Garvey, "The chip-scale atomic clock-coherent population trapping vs. conventional interrogation," SYMMETRICOM-TECHNOLOGY REALIZATION CENTER BEVERLY MA, Tech. Rep., 2003.

[4] R. Wynands and A. Nagel, "Precision spectroscopy with coherent dark states," *Applied Physics B: Lasers and Optics*, vol. 68, no. 1, pp. 1–25, Jan. 1999.

[5] F. Levi, A. Godone, and J. Vanier, "The light shift effect in the coherent population trapping cesium maser," *IEEE Transactions on Ultrasonics, Ferroelectrics, and Frequency Control*, vol. 47, no. 2, pp. 466–470, Mar. 2000.

[6] J. Vanier and C. Audoin, *The quantum physics of atomic frequency standards*. Boca Raton, FL: CRC Press, 1989.

[7] B. Fitzgibbon, M. P. Kennedy, and F. Maloberti, "Hardware reduction in digital delta-sigma modulators via bus-splitting and error masking-part I: Constant input," *IEEE Transactions on Circuits and Systems I: Regular Papers*, vol. 58, no. 9, pp. 2137–2148, Sep. 2011.

[8] D. Ruffieux, M. Contaldo, J. Haesler, and S. Lecomte, "A low-power fully integrated RF locked loop for miniature atomic clock," in *IEEE International Solid-State Circuits Conference*, San Francisco, CA, USA, Feb. 2011, pp. 48–50.

[9] S. A. Knappe, “Emerging topics: MEMS atomic clocks,” in *Comprehensive Microsystems*, Y. Gianchandani, Ed. Maryland Heights, MO: Elsevier, Nov. 2007, vol. 3, pp. 571–612.

[10] T. Zanon, S. Tremine, S. Guerandel, Emeric de Clercq, D. Holleville, N. Dimarcq, and A. Clairon, “Observation of Raman-Ramsey fringes with optical CPT pulses,” *IEEE Transactions on Instrumentation and Measurement*, vol. 54, no. 2, pp. 776–779, Apr. 2005.

[11] W. D. Phillips, “Nobel lecture: Laser cooling and trapping of neutral atoms,” *Reviews of Modern Physics*, vol. 70, no. 3, pp. 721–741, July 1998.

[12] J. Ye and S. T. Cundiff, *Femtosecond optical frequency comb: principle, operation and applications*. Springer Science & Business Media, 2005.

[13] Z. L. Newman, V. Maurice, T. Drake, J. R. Stone, T. C. Briles, D. T. Spencer, C. Fredrick, Q. Li, D. Westly, B. Ilic, *et al.*, “Architecture for the photonic integration of an optical atomic clock,” *Optica*, vol. 6, no. 5, pp. 680–685, May 2019.

[14] R. Rudgley, *The lost civilizations of the stone age*. New York: Simon and Schuster, 2000.

[15] C. Huygens and H. Oscillatorium, *The pendulum clock*. Ames: Iowa State Univesity Press, 1986.

[16] D. Sobel, *Longitude: The true story of a lone genius who solved the greatest scientific problem of his time*. London, UK: Macmillan, 2005.

[17] W. I. Milham, *Time & timekeepers: including the history, construction, care, and accuracy of clocks and watches*. London, UK: Macmillan, 1923.

[18] J. R. Vig, “Quartz crystal resonators and oscillators for frequency control and timing applications - A tutorial,” R&D Technical Report SLCETTR-88-1 (Rev 7.0) (AD-A284995), Aug. 1994.

[19] W. McGrew, X. Zhang, R. Fasano, S. Schäffer, K. Beloy, D. Nicolodi, R. Brown, N. Hinkley, G. Milani, M. Schioppo, T. Yoon, and A. Ludlow, “Atomic clock performance enabling geodesy below the centimetre level,” *Nature*, vol. 564, no. 7734, pp. 87–90, Nov. 2018.

[20] R. G. ITU-T, “Series G: Transmission systems and media digital systems and networks,” *Ginebra, Suiza: ITU*, 1997.

[21] J. Allnutt, D. Anand, D. Arnold, A. Goldstein, Y.-S. Li-Baboud, A. Martin, C. Nguyen, R. Noseworthy, R. Subramaniam, and M. Weiss, “Timing challenges in the smart grid,” Special Publication (NIST SP) - 1500-08, 2017.

[22] M. Martin, M. Bishof, M. Swallows, X. Zhang, C. Benko, J. Von-Stecher, A. Gorshkov, A. Rey, and J. Ye, “A quantum many-body spin system in an optical lattice clock,” *Science*, vol. 341, no. 6146, pp. 632–636, Aug. 2013.

[23] A. Rey, A. Gorshkov, C. Kraus, M. Martin, M. Bishof, M. Swallows, X. Zhang, C. Benko, J. Ye, N. Lemke, and A. Ludlow, “Probing many-body interactions in an optical lattice clock,” *Annals of Physics*, vol. 340, no. 1, pp. 311–351, Jan. 2014.

[24] S. Bize, P. Laurent, M. Abgrall, H. Marion, I. Maksimovic, L. Cacciapuoti, J. Grünert, C. Vian, F. P. Dos Santos, P. Rosenbusch, P. Lemonde, G. Santarelli, P. Wolf, A. Clairon, A. Luiten, M. Tobar, and C. Salomon, “Advances in atomic fountains,” *Comptes rendus physique*, vol. 5, no. 8, pp. 829–843, Oct. 2004.

[25] M. Fischer, N. Kolachevsky, M. Zimmermann, R. Holzwarth, T. Udem, T. W. Hänsch, M. Abgrall, J. Grünert, I. Maksimovic, S. Bize, H. Marion, D. Pereira, P. Lemonde, G. Santarelli, P. Laurent, A. Clairon, C. Salomon, M. Haas, U. Jentschura, and C. Keitel, “New limits on the drift of fundamental constants from laboratory measurements,” *Physical Review Letters*, vol. 92, no. 23, p. 230802, June 2004.

[26] S. Blatt, A. Ludlow, G. Campbell, J. W. Thomsen, T. Zelevinsky, M. Boyd, J. Ye, X. Baillard, M. Fouché, R. Le Targat, A. Brusch, P. Lemonde, M. Takamoto, F. Hong, H. Katori, and V. Flambaum, “New limits on coupling of fundamental constants to gravity using ^{87}Sr optical lattice clocks,” *Physical Review Letters*, vol. 100, no. 14, p. 140801, Apr. 2008.

[27] T. Rosenband, D. Hume, P. Schmidt, C.-W. Chou, A. Brusch, L. Lorini, W. Oskay, R. E. Drullinger, T. M. Fortier, J. E. Stalnaker, S. Diddams, W. Swann, N. Newbury, W. Itano, D. Wineland, and J. Bergquist, “Frequency ratio of Al+ and Hg+ single-ion optical clocks; metrology at the 17th decimal place,” *Science*, vol. 319, no. 5871, pp. 1808–1812, Mar. 2008.

[28] A. D. Ludlow, M. M. Boyd, J. Ye, E. Peik, and P. O. Schmidt, “Optical atomic clocks,” *Reviews of Modern Physics*, vol. 87, no. 2, p. 637, June 2015.

[29] D. J. Wineland, *Single-Atom Optical Clocks*. Technical Report, Georgia Institute of Technology, 2013.

[30] S. Goldberg, "Miniaturized atomic frequency standard having both filter cell and absorption cell in resonator cavity," Jan. 15 1985, U.S. Patent 4,494,085.

[31] C. Affolderbach, F. Droz, and G. Mileti, "Experimental demonstration of a compact and high-performance laser-pumped rubidium gas cell atomic frequency standard," *IEEE Transactions on Instrumentation and Measurement*, vol. 55, no. 2, pp. 429–435, Apr. 2006.

[32] J. Kitching, S. Knappe, and E. A. Donley, "Atomic sensors - A review," *IEEE Sensors Journal*, vol. 11, no. 9, pp. 1749–1758, Sept. 2011.

[33] "IEEE standard for a precision clock synchronization protocol for networked measurement and control systems - redline," *IEEE Std 1588-2008 (Revision of IEEE Std 1588-2002) - Redline*, pp. 1–300, July 2008.

[34] D. W. Allan, N. Ashby, and C. C. Hodge, *The science of timekeeping*. Hewlett-Packard, 1997.

[35] H. Li, L. Han, R. Duan, and G. M. Garner, "Analysis of the synchronization requirements of 5G and corresponding solutions," *IEEE Communications Standards Magazine*, vol. 1, no. 1, pp. 52–58, Mar. 2017.

[36] A. T. Gardner and J. A. Collins, "Advancements in high-performance timing for long term underwater experiments: A comparison of chip scale atomic clocks to traditional microprocessor-compensated crystal oscillators," in *Oceans*, Hampton Roads, VA, USA, Oct. 2012, pp. 1–8.

[37] H. Fruehauf, "Fast direct-P (Y) GPS signal acquisition using a special portable clock," Zyfer Inc. and Odetics Inc. Anaheim, CA, Tech. Rep., 2002.

[38] J. Kitching, "Chip-scale atomic devices," *Applied Physics Reviews*, vol. 5, no. 3, p. 031302, Aug. 2018.

[39] A. Ucar, Y. Adane, B. Bardak, C. Paparo, R. Berry, and I. Kale, "A chip scale atomic clock driven receiver for multi-constellation GNSS," *The Journal of Navigation*, vol. 66, no. 3, pp. 449–464, Mar. 2013.

[40] M. A. Sturza, "GPS navigation using three satellites and a precise clock," *Navigation*, vol. 30, no. 2, pp. 146–156, Aug. 1983.

[41] R. Ramlall, J. Streter, and J. F. Schnecker, "Three satellite navigation in an urban canyon using a chip-scale atomic clock," in *Proceedings of the 24th International*

Technical Meeting of The Satellite Division of the Institute of Navigation (ION GNSS 2011), Portland, OR, Sept. 2001, p. 2937.

[42] J. R. Vig, "Military applications of high accuracy frequency standards and clocks," *IEEE Transactions on Ultrasonics, Ferroelectrics, and Frequency Control*, vol. 40, no. 5, pp. 522–527, Sept. 1993.

[43] R. Filler and J. Vig, "Low-power oscillator/clock for direct P-code acquisition," in *Institute of Navigation, Annual Meeting, 51 st, Colorado Springs, CO*, 1995, pp. 405–411.

[44] P. Horowitz and W. Hill, *The art of electronics*. Cambridge Univ. Press, 1989.

[45] C. T. . Nguyen, "MEMS technology for timing and frequency control," *IEEE Transactions on Ultrasonics, Ferroelectrics, and Frequency Control*, vol. 54, no. 2, pp. 251–270, Feb. 2007.

[46] C.-W. Chou, D. Hume, T. Rosenband, and D. Wineland, "Optical clocks and relativity," *Science*, vol. 329, no. 5999, pp. 1630–1633, Sept. 2010.

[47] W. F. Snyder, "Lord Kelvin on atoms as fundamental natural standards (for base units)," *IEEE Transactions on Instrumentation and Measurement*, vol. 22, no. 1, pp. 99–99, Mar. 1973.

[48] P. H. Dana and B. M. Penrod, "The role of GPS in precise time and frequency dissemination," *GPS World*, vol. 1, no. 4, pp. 38–43, July 1990.

[49] W. Lewandowski, J. Azoubib, and W. J. Klepczynski, "GPS: primary tool for time transfer," *Proceedings of the IEEE*, vol. 87, no. 1, pp. 163–172, Jan. 1999.

[50] D. D. McCarthy and P. K. Seidelmann, *Time: from Earth rotation to atomic physics*. Cambridge University Press, 2018.

[51] D. Ruffieux, J. Haesler, L. Balet, T. Overstolz, J. Pierer, R. J. James, and S. Lecomte, "Statistics of time and frequency data analysis," in *Time and Frequency: Theory and Fundamentals*, B. E. Blair, Ed. National Bureau of Standards Monograph 140, U.S. Department of Commerce, 1974, ch. 8, pp. 151–204.

[52] D. W. Allan, "Statistics of atomic frequency standards," *Proceedings of the IEEE*, vol. 54, no. 2, pp. 221–230, Feb. 1966.

[53] F. Riehle, *Frequency standards: basics and applications*. John Wiley & Sons, 2006.

[54] W. J. Riley, "Handbook of frequency stability analysis," NIST Special Publication 1065, NIST, Boulder, CO, USA, 2008.

[55] S. R. Jefferts, J. Shirley, T. Parker, T. Heavner, D. Meekhof, C. Nelson, F. Levi, G. Costanzo, A. De Marchi, R. Drullinger, *et al.*, "Accuracy evaluation of NIST-F1," *Metrologia*, vol. 39, no. 4, p. 321, 2002.

[56] T. Heavner, S. Jefferts, E. Donley, J. Shirley, and T. Parker, "NIST-F1: recent improvements and accuracy evaluations," *Metrologia*, vol. 42, no. 5, p. 411, 2005.

[57] W. J. Riley, "A history of the rubidium frequency standard," IEEE UFFC-S History, http://ieee-uffc.org/aboutus/history/a-history-of-the-rubidium-frequency-standard.pdf, July 2019.

[58] N. Hinkley, J. Sherman, N. Phillips, M. Schioppo, N. Lemke, K. Beloy, M. Pizzocaro, C. W. Oates, and A. Ludlow, "An atomic clock with 10^{-18} instability," *Science*, vol. 341, no. 6151, pp. 1215–1218, Sept. 2013.

[59] B. Bloom, T. Nicholson, J. Williams, S. Campbell, M. Bishof, X. Zhang, W. Zhang, S. Bromley, and J. Ye, "An optical lattice clock with accuracy and stability at the 10^{-18} level," *Nature*, vol. 506, no. 7486, p. 71, Feb. 2014.

[60] R. Lutwak, D. Emmons, T. English, and W. Riley, "The chip-scale atomic clock-recent development progress," Symmetricom-Technology Realization Center Beverly, MA, Tech. Rep., 2004.

[61] C. Wang, X. Yi, J. Mawdsley, M. Kim, Z. Hu, Y. Zhang, B. Perkins, and R. Han, "Chip-scale molecular clock," *IEEE Journal of Solid-State Circuits*, vol. 54, no. 4, pp. 914–926, Apr. 2019.

[62] C. Wang, X. Yi, J. Mawdsley, M. Kim, Z. Wang, and R. Han, "An on-chip fully electronic molecular clock based on sub-terahertz rotational spectroscopy," *Nature Electronics*, vol. 1, no. 7, p. 421, July 2018.

[63] Z. Newman, V. Maurice, T. Drake, J. Stone, T. Briles, D. Spencer, C. Fredrick, Q. Li, D. Westly, B. Ilic, *et al.*, "Photonic integration of an optical atomic clock," *arXiv:1811.00616, physics.optics*, 2018.

[64] H. Zhang, H. Herdian, A. T. Narayanan, A. Shirane, M. Suzuki, K. Harasaka, K. Adachi, S. Yanagimachi, and K. Okada, "Ultra-low-power atomic clock for

satellite constellation with 2.2×10^{-12} long-term allan deviation using cesium coherent population trapping," in *IEEE International Solid- State Circuits Conference - (ISSCC)*, San Francisco, CA, USA, Feb. 2019, pp. 462–464.

[65] R. Lutwak, "The SA. 45s chip-scale atomic clock early production statistics," in *Proc. 43rd Annu. Precise Time Time Interval Syst. Appl. Meeting*, Long Beach, CA, USA, Nov. 2011, pp. 201–220.

[66] Microchip Technology, "SA.45s CSAC and RoHS CSAC options 001 and 003 chip-scale atomic clock," *DS00002985A datasheet*, 2019.

[67] R. Lutwak, A. Rashed, M. Varghese, G. Tepolt, J. Leblanc, M. Mescher, D. K. Serkland, and G. M. Peake, "The miniature atomic clock - pre-production results," in *IEEE International Frequency Control Symposium Joint with the 21st European Frequency and Time Forum*, Geneva, Switzerland, May 2007, pp. 1327–1333.

[68] D. W. Youngner, L. M. Lust, D. R. Carlson, S. T. Lu, L. J. Forner, H. M. Chanhvongsak, and T. D. Stark, "A manufacturable chip-scale atomic clock," in *International Solid-State Sensors, Actuators and Microsystems Conference*, Lyon, France, June 2007, pp. 39–44.

[69] J. F. DeNatale, R. L. Borwick, C. Tsai, P. A. Stupar, Y. Lin, R. A. Newgard, R. W. Berquist, and M. Zhu, "Compact, low-power chip-scale atomic clock," in *IEEE/ION Position, Location and Navigation Symposium*, Monterey, CA, USA, May 2008, pp. 67–70.

[70] M. Bloch, I. Pascaru, C. Stone, and T. McClelland, "Subminiature rubidium frequency standard for commercial applications," in *IEEE International Frequency Control Symposium*, Salt Lake City, UT, USA, June 1993, pp. 164–177.

[71] P. J. Chantry, I. Liberman, W. R. Verbanets, C. F. Petronio, R. L. Cather, and W. D. Partlow, "Miniature laser-pumped cesium cell atomic clock oscillator," in *IEEE International Frequency Control Symposium*, Honolulu, HI, USA, June 1996, pp. 1002–1010.

[72] A. Taichenachev, V. I. Yudin, V. L. Velichansky, and S. A. Zibrov, "On the unique possibility of significantly increasing the contrast of dark resonances on the D1 line of ^{87}Rb," *Journal of Experimental and Theoretical Physics Letters*, vol. 82, no. 7, pp. 398–403, Oct. 2005.

[73] F. Levi, A. Godone, J. Vanier, S. Micalizio, and G. Modugno, "Line-shape of dark line and maser emission profile in CPT," *The European Physical Journal D-Atomic, Molecular, Optical and Plasma Physics*, vol. 12, no. 1, pp. 53–59, Sept.

[74] M. Stähler, R. Wynands, S. Knappe, J. Kitching, L. Hollberg, A. Taichenachev, and V. Yudin, "Coherent population trapping resonances in thermal ^{85}Rb vapor: D_1 versus D_2 line excitation," *Optics letters*, vol. 27, no. 16, pp. 1472–1474, Aug. 2002.

[75] G. Alzetta, S. Cartaleva, Y. Dancheva, C. Andreeva, S. Gozzini, L. Botti, and A. Rossi, "Coherent effects on the Zeeman sublevels of hyperfine states at the D_1 and D_2 lines of Rb," *Journal of Optics B: Quantum and Semiclassical Optics*, vol. 3, no. 3, pp. 181–188, Apr.

[76] E. Kroemer, J. Rutkowski, V. Maurice, R. Vicarini, M. A. Hafiz, C. Gorecki, and R. Boudot, "Characterization of commercially available vertical-cavity surface-emitting lasers tuned on Cs D_1 line at 894.6 nm for miniature atomic clocks," *Applied optics*, vol. 55, no. 31, pp. 8839–8847, Nov. 2016.

[77] D. K. Serkland, K. M. Geib, G. M. Peake, R. Lutwak, A. Rashed, M. Varghese, G. Tepolt, and M. Prouty, "VCSELs for atomic sensors," in *Vertical-Cavity Surface-Emitting Lasers XI*, vol. 6484, San Jose, CA, USA, Feb., p. 648406.

[78] G. K. Woodgate, *ELEMENTARY ATOMIC STRUCTURE.* Clarendon Press, 1970.

[79] W. Happer, "Optical pumping," *Reviews of Modern Physics*, vol. 44, no. 2, pp. 169–250, Apr. 1972.

[80] G. Alzetta, A. Gozzini, L. Moi, and G. Orriols, "An experimental method for the observation of RF transitions and laser beat resonances in oriented Na vapour," *Il Nuovo Cimento B (1971-1996)*, vol. 36, no. 1, pp. 5–20, Nov. 1976.

[81] R. M. Whitley and C. Stroud Jr, "Double optical resonance," *Physical Review A*, vol. 14, no. 4, p. 1498, Oct. 1976.

[82] E. Arimondo and G. Orriols, "Nonabsorbing atomic coherences by coherent two-photon transitions in a three-level optical pumping," *Lettere Al Nuovo Cimento (1971–1985)*, vol. 17, no. 10, pp. 333–338, Nov. 1976.

[83] H. Gray, R. Whitley, and C. Stroud, "Coherent trapping of atomic populations," *Optics letters*, vol. 3, no. 6, pp. 218–220, 1978.

[84] J. Vanier, M. Levine, D. Janssen, and M. Delaney, "Contrast and linewidth of the coherent population trapping transmission hyperfine resonance line in ^{87}Rb: effect of optical pumping," *Physical Review A*, vol. 67, no. 6, p. 065801, June 2003.

[85] J. Vanier, M. Tetu, and L. . Bernier, "Transfer of frequency stability from an atomic frequency reference to a quartz crystal oscillator," in *32nd Annual Symposium on Frequency Control*, Atlantic City, NJ, USA, May 1978, pp. 520–526.

[86] R. F. Lacey, A. L. Helgesson, and J. H. Holloway, "Short-term stability of passive atomic frequency standards," *Proceedings of the IEEE*, vol. 54, no. 2, pp. 170–176, Feb. 1966.

[87] J. Vanier and L. Bernier, "On the signal-to-noise ratio and short-term stability of passive rubidium frequency standards," *IEEE Transactions on Instrumentation and Measurement*, vol. IM-30, no. 4, pp. 277–282, Dec. 1981.

[88] J. Vanier, "Coherent population trapping for the realization of a small, stable, atomic clock," in *IEEE International Frequency Control Symposium and PDA Exhibition (Cat. No.02CH37234)*, New Orleans, LA, USA, May 2002, pp. 424–434.

[89] J. Vanier, M. W. Levine, D. Janssen, and M. J. Delaney, "The coherent population trapping passive frequency standard [Rb example]," *IEEE Transactions on Instrumentation and Measurement*, vol. 52, no. 2, pp. 258–262, Apr. 2003.

[90] J. Vanier, "Atomic frequency standard," Nov. 20 2001, US Patent 6,320,472.

[91] L. S. Cutler and C. L. Searle, "Some aspects of the theory and measurement of frequency fluctuations in frequency standards," *Proceedings of the IEEE*, vol. 54, no. 2, pp. 136–154, Feb. 1966.

[92] C. Audoin and J. Vanier, "Atomic frequency standards and clocks," *Journal of Physics E: Scientific Instruments*, vol. 9, no. 9, pp. 697–720, 1976.

[93] J. A. Barnes, A. R. Chi, L. S. Cutler, D. J. Healey, D. B. Leeson, T. E. McGunigal, J. A. Mullen, W. L. Smith, R. L. Sydnor, R. F. C. Vessot, and G. M. R. Winkler, "Characterization of frequency stability," *IEEE Transactions on Instrumentation and Measurement*, vol. IM-20, no. 2, pp. 105–120, May 1971.

[94] K. Lei, H. Heidari, P. Mak, M. Law, F. Maloberti, and R. P. Martins, "A handheld high-sensitivity micro-NMR CMOS platform with B-field stabilization for multi-type biological/chemical assays," *IEEE Journal of Solid-State Circuits*, vol. 52, no. 1, pp. 284–297, Jan. 2017.

[95] J. Vanier, “Atomic clocks based on coherent population trapping: A review,” *Applied Physics B*, vol. 81, no. 4, pp. 421–442, Apr. 2005.

[96] D. Miletic, C. Affolderbach, M. Hasegawa, R. Boudot, C. Gorecki, and G. Mileti, “AC Stark-shift in CPT-based Cs miniature atomic clocks,” *Applied Physics B*, vol. 109, no. 1, pp. 89–97, Oct. 2012.

[97] J. Vanier, A. Godone, and F. Levi, “Coherent population trapping in cesium: Dark lines and coherent microwave emission,” *Physical review A*, vol. 58, no. 3, pp. 2345–2358, Sept. 1998.

[98] E. Arimondo, “V coherent population trapping in laser spectroscopy,” *Progress in optics*, vol. 35, pp. 257–354, Jan. 1996.

[99] J. R. P. Angel and P. Sandars, “The hyperfine structure stark effect I. theory,” *Proceedings of the Royal Society of London. Series A. Mathematical and Physical Sciences*, vol. 305, no. 1480, pp. 125–138, May 1968.

[100] P. Cash, W. Krzewick, P. Machado, K. R. Overstreet, M. Silveira, M. Stanczyk, D. Taylor, and X. Zhang, “Microsemi chip scale atomic clock (CSAC) technical status, applications, and future plans,” in *European Frequency and Time Forum (EFTF)*, Turin, Italy, Apr. 2018, pp. 65–71.

[101] R. Dicke, “The effect of collisions upon the Doppler width of spectral lines,” *Physical Review*, vol. 89, no. 2, pp. 472–473, Jan. 1953.

[102] N. Allard and J. Kielkopf, “The effect of neutral nonresonant collisions on atomic spectral lines,” *Reviews of modern physics*, vol. 54, no. 4, pp. 1103–1182, Oct. 1982.

[103] D. E. Nikonov, U. W. Rathe, M. O. Scully, S.-Y. Zhu, E. S. Fry, X. Li, G. Padmabandu, and M. Fleischhauer, “Atomic coherence effects within the sodium D_1 manifold. II. coherent optical pumping,” *Quantum Optics: Journal of the European Optical Society Part B*, vol. 6, no. 4, pp. 245–260, 1994.

[104] A. Post, Y.-Y. Jau, N. Kuzma, and W. Happer, “Amplitude-versus frequency-modulated pumping light for coherent population trapping resonances at high buffer-gas pressure,” *Physical Review A*, vol. 72, no. 3, p. 033417, Sept. 2005.

[105] N. Vitanov, B. Shore, L. Yatsenko, K. Böhmer, T. Halfmann, T. Rickes, and K. Bergmann, “Power broadening revisited: theory and experiment,” *Optics communications*, vol. 199, no. 1-4, pp. 117–126, Nov. 2001.

[106] T. Mukaihara, N. Ohnoki, Y. Hayashi, N. Hatori, F. Koyama, and K. Iga, "Excess intensity noise originated from polarization fluctuation in vertical-cavity surface-emitting lasers," *IEEE Photonics Technology Letters*, vol. 7, no. 10, pp. 1113–1115, Oct. 1995.

[107] J. Kaiser, C. Degen, and W. Elsässer, "Polarization-switching influence on the intensity noise of vertical-cavity surface-emitting lasers," *JOSA B*, vol. 19, no. 4, pp. 672–677, Apr. 2002.

[108] F. Gong, Y.-Y. Jau, K. Jensen, and W. Happer, "Electrolytic fabrication of atomic clock cells," *Review of scientific instruments*, vol. 77, no. 7, p. 076101, July 2006.

[109] L.-A. Liew, J. Moreland, and V. Gerginov, "Wafer-level filling of microfabricated atomic vapor cells based on thin-film deposition and photolysis of cesium azide," *Applied physics letters*, vol. 90, no. 11, p. 114106, Mar. 2007.

[110] C. J. Erickson, M. Van Zijll, G. Doermann, and D. S. Durfee, "An ultrahigh stability, low-noise laser current driver with digital control," *Review of Scientific Instruments*, vol. 79, no. 7, p. 073107, 2008.

[111] C. Audoin, V. Candelier, and N. Diamarcq, "A limit to the frequency stability of passive frequency standards due to an intermodulation effect," *IEEE Transactions on Instrumentation and Measurement*, vol. 40, no. 2, pp. 121–125, Apr. 1991.

[112] C. Szekely, F. L. Walls, J. P. Lowe, R. E. Drullinger, and A. Novick, "Reducing local oscillator phase noise limitations on the frequency stability of passive frequency standards: tests of a new concept," *IEEE Transactions on Ultrasonics, Ferroelectrics, and Frequency Control*, vol. 41, no. 4, pp. 518–521, July 1994.

[113] J. Q. Deng, G. Mileti, D. A. Jennings, R. E. Drullinger, and F. L. Walls, "Improving the short-term stability of laser pumped Rb clocks by reducing the effects of the interrogation oscillator," in *International Frequency Control Symposium*, Orlando, FL, USA, May 1997, pp. 438–445.

[114] J. Q. Deng, G. Mileti, R. Drullinger, D. Jennings, and F. L. Walls, "Noise considerations for locking to the center of a Lorentzian line," *Physical Review A*, vol. 59, no. 1, pp. 773–777, Jan. 1999.

[115] S. Romisch and R. Lutwak, "Low-power, 4.6-GHz, stable oscillator for CSAC," in *IEEE International Frequency Control Symposium and Exposition*, Miami, FL, USA, June 2006, pp. 448–451.

[116] A. Brannon, J. Breitbarth, and Z. Popovic, "A low-power, low phase noise local oscillator for chip-scale atomic clocks," in *IEEE MTT-S International Microwave Symposium Digest*, Long Beach, CA, USA, June 2005, pp. 1535–1538.

[117] B. Razavi and R. Behzad, *RF microelectronics*. Prentice hall New Jersey, 1998, vol. 1.

[118] Y. Zhao, S. Tanner, A. Casagrande, C. Affolderbach, L. Schneller, G. Mileti, and P. Farine, "CPT cesium-cell atomic clock operation with a 12-mW frequency synthesizer ASIC," *IEEE Transactions on Instrumentation and Measurement*, vol. 64, no. 1, pp. 263–270, Jan 2015.

[119] E. Hegazi, H. Sjoland, and A. A. Abidi, "A filtering technique to lower LC oscillator phase noise," *IEEE Journal of Solid-State Circuits*, vol. 36, no. 12, pp. 1921–1930, Dec. 2001.

[120] W. Robins, *Phase noise in signal sources: theory and applications*. IET, 1984, vol. 9.

[121] H. Zhang, H. Herdian, A. T. Narayanan, B. Liu, R. Wu, A. Shirane, and K. Okada, "A -194 dBc/Hz FoM VCO with low-supply sensitivity for ultra-low-power atomic clock," in *Asia-Pacific Microwave Conference (APMC)*, Kyoto, Japan, Nov. 2018, pp. 788–790.

[122] H. Zhang, A. T. Narayanan, B. Liu, K. Okada, and A. Matsuzawa, "A pulse V-CO with tail filter," in *IEEE Asia Pacific Microwave Conference (APMC)*, Kuala Lumpar, Malaysia, Nov. 2017, pp. 942–945.

[123] H. Zhang, A. T. Narayanan, H. Herdian, B. Liu, R. Wu, A. Shirane, and K. Okada, "A power-efficient pulse-VCO for chip-scale atomic clock," *IEICE Transactions on Electronics*, vol. 102, no. 4, pp. 276–286, Apr. 2019.

[124] G. Srinivasan, "Modeling the cosmic-ray-induced soft-error rate in integrated circuits: An overview," *IBM Journal of Research and Development*, vol. 40, no. 1, pp. 77–89, Jan. 1996.

[125] G. C. Messenger and M. S. Ash, *Single Event Phenomena*. New York, Chapman & Hall, 1997.

[126] J. Canaris and S. Whitaker, "Circuit techniques for the radiation environment of space," in *Proceedings of the IEEE 1995 Custom Integrated Circuits Conference*, Santa Clara, CA, USA, May 1995, pp. 77–80.

[127] D. Matsuura, K. Hirose, D. Kobayashi, S. Ishii, M. Kusano, Y. Kuroda, and H. Saito, "Radiation-hardened phase-locked loop fabricated in 200 nm SOI-CMOS," in *12th European Conference on Radiation and Its Effects on Components and Systems*, Sevilla, Spain, Sept. 2011, pp. 150–155.

[128] T. D. Loveless, L. W. Massengill, B. L. Bhuva, W. T. Holman, M. C. Casey, R. A. Reed, S. A. Nation, D. McMorrow, and J. S. Melinger, "A probabilistic analysis technique applied to a radiation-hardened-by-design voltage-controlled oscillator for mixed-signal phase-locked loops," *IEEE Transactions on Nuclear Science*, vol. 55, no. 6, pp. 3447–3455, Dec. 2008.

[129] S. Kim, A. Tsuchiya, and H. Onodera, "Radiation-hardened PLL with a switchable dual modular redundancy structure," *IEICE Transactions on Electronics*, vol. 97, no. 4, pp. 325–331, Apr. 2014.

[130] P. Shivakumar, M. Kistler, S. W. Keckler, D. Burger, and L. Alvisi, "Modeling the effect of technology trends on the soft error rate of combinational logic," in *Proceedings International Conference on Dependable Systems and Networks*, Washington, DC, USA, June 2002, pp. 389–398.

[131] R. Harada, S. Abe, H. Fuketa, T. Uemura, M. Hashimoto, and Y. Watanabe, "Angular dependency of neutron-induced multiple cell upsets in 65-nm 10T subthreshold SRAM," *IEEE Transactions on Nuclear Science*, vol. 59, no. 6, pp. 2791–2795, Dec. 2012.

[132] J. Furuta, K. Kobayashi, and H. Onodera, "Impact of cell distance and well-contact density on neutron-induced multiple cell upsets," *IEICE Transactions on Electronics*, vol. 98, no. 4, pp. 298–303, Apr. 2015.

[133] H. Maruoka, M. Hifumi, J. Furuta, and K. Kobayashi, "A low-power radiation-hardened flip-flop with stacked transistors in a 65 nm FDSOI process," *IEICE Transactions on Electronics*, vol. 101, no. 4, pp. 273–280, Apr. 2018.

[134] S. Hirokawa, R. Harada, M. Hashimoto, and T. Onoye, "Characterizing alpha- and neutron-induced SEU and MCU on SOTB and bulk 0.4-V SRAMs," *IEEE Transactions on Nuclear Science*, vol. 62, no. 2, pp. 420–427, Apr. 2015.

[135] T. Shioda, Y. Sekine, and H. Otsuka, "High precision TCXO for rapid environmental temperature change," in *IEEE International Frequency Control Symposium and PDA Exhibition Jointly with the 17th European Frequency and Time Forum*, Tampa, FL, USA, May 2003, pp. 444–449.

[136] K. Kobayashi, Y. Mori, T. Kobata, M. Ito, S. Watanabe, S. Sato, and K. Akaike, "High-performance DSP-TCXO using twin-crystal oscillator," in *IEEE International Frequency Control Symposium (FCS)*, Taipei, Taiwan, May 2014, pp. 1–4.

[137] D. V. Bogomolov and R. Boroditsky, "Low phase noise UHF TCXO," in *Proceedings of the 2005 IEEE International Frequency Control Symposium and Exposition*, Vancouver, BC, Canada, Aug. 2005, pp. 509–511.

[138] R. Lutwak, "The chip-scale atomic clock - recent developments," in *IEEE International Frequency Control Symposium Joint with the 22nd European Frequency and Time forum*, Besancon, France, Apr. 2009, pp. 573–577.

[139] D. Ruffieux, J. Haesler, L. Balet, T. Overstolz, J. Pierer, R. J. James, and S. Lecomte, "Towards portable miniature atomic clocks," in *Frequency references, power management for SoC, and smart wireless interfaces*, A. Baschirotto, K. A. A. Makinwa, and P. Harpe, Eds. Springer International Publishing, 2014, ch. 6, pp. 83–99.

[140] D. M. Tanner, J. A. Walraven, K. Helgesen, L. W. Irwin, F. Brown, N. F. Smith, and N. Masters, "MEMS reliability in shock environments," in *IEEE International Reliability Physics Symposium Proceedings. 38th Annual (Cat. No.00CH37059)*, San Jose, CA, USA, Apr. 2000, pp. 129–138.

[141] M. Garampazzi, P. M. Mendes, N. Codega, D. Manstretta, and R. Castello, "Analysis and design of a 195.6 dBc/Hz peak FoM P-N class-B oscillator with transformer-based tail filtering," *IEEE Journal of Solid-State Circuits*, vol. 50, no. 7, pp. 1657–1668, July 2015.

[142] A. Mazzanti and P. Andreani, "Class-C harmonic CMOS VCOs, with a general result on phase noise," *IEEE Journal of Solid-State Circuits*, vol. 43, no. 12, pp. 2716–2729, Dec. 2008.

[143] K. Okada, Y. Nomiyama, R. Murakami, and A. Matsuzawa, "A 0.114-mW dual-conduction class-C CMOS VCO with 0.2-V power supply," in *Symposium on VLSI Circuits*, Kyoto, Japan, June 2009, pp. 228–229.

[144] W. Deng, K. Okada, and A. Matsuzawa, "Class-C VCO with amplitude feedback loop for robust start-up and enhanced oscillation swing," *IEEE Journal of Solid-State Circuits*, vol. 48, no. 2, pp. 429–440, Feb. 2013.

[145] A. Hajimiri and T. H. Lee, "A general theory of phase noise in electrical oscillators," *IEEE Journal of Solid-State Circuits*, vol. 33, no. 2, pp. 179–194, Feb. 1998.

[146] L. Fanori and P. Andreani, “Highly efficient class-C CMOS VCOs, including a comparison with class-B VCOs,” *IEEE Journal of Solid-State Circuits*, vol. 48, no. 7, pp. 1730–1740, July 2013.

[147] Y. Takeuchi, K. Okada, and A. Matsuzawa, “An improved dual-conduction class-C VCO using a tail resistor,” in *6th European Microwave Integrated Circuit Conference*, Manchester, UK, Oct. 2011, pp. 204–207.

[148] M. Tohidian, A. Fotowat-Ahmadi, M. Kamarei, and F. Ndagijimana, “High-swing class-C VCO,” in *European Microwave Integrated Circuit Conference (ESSCIRC)*, Helsinki, Finland, Sept. 2011, pp. 495–498.

[149] A. T. Narayanan, K. Kimura, W. Deng, K. Okada, and A. Matsuzawa, “A pulse-driven LC-VCO with a figure-of-merit of -192dBc/Hz,” in *40th European Solid State Circuits Conference (ESSCIRC)*, Venice Lido, Italy, Sept. 2014, pp. 343–346.

[150] K. Kimura, A. T. Narayanan, K. Okada, and A. Matsuzawa, “An AM-PM noise mitigation technique in class-C VCO,” *IEICE Transactions on Electronics*, vol. 98, no. 12, pp. 1161–1170, Dec. 2015.

[151] A. T. Narayanan, N. Li, K. Okada, and A. Matsuzawa, “A pulse-tail-feedback VCO achieving FoM of 195dBc/Hz with flicker noise corner of 700Hz,” in *Symposium on VLSI Circuits*, Kyoto, Japan, June 2017, pp. C124–C125.

[152] P. Kinget, “Integrated GHz voltage controlled oscillators,” in *Analog circuit design*. Springer, 1999, pp. 353–381.

[153] P. Andreani, Xiaoyan Wang, L. Vandi, and A. Fard, “A study of phase noise in colpitts and LC-tank CMOS oscillators,” *IEEE Journal of Solid-State Circuits*, vol. 40, no. 5, pp. 1107–1118, May 2005.

[154] M. Garampazzi, S. Dal Toso, A. Liscidini, D. Manstretta, P. Mendez, L. Romano, and R. Castello, “An intuitive analysis of phase noise fundamental limits suitable for benchmarking LC oscillators,” *IEEE Journal of Solid-State Circuits*, vol. 49, no. 3, pp. 635–645, Mar. 2014.

[155] J. van der Tang and D. Kasperkovitz, “Oscillator design efficiency: a new figure of merit for oscillator benchmarking,” in *IEEE International Symposium on Circuits and Systems (ISCAS)*, vol. 2, Geneva, Switzerland, May 2000, pp. 533–536 vol.2.

[156] A. G. Jordan and N. A. Jordan, "Theory of noise in metal oxide semiconductor devices," *IEEE Transactions on Electron Devices*, vol. 12, no. 3, pp. 148–156, March 1965.

[157] C. T. Sah, S. Y. Wu, and F. H. Hielscher, "The effects of fixed bulk charge on the thermal noise in metal-oxide-semiconductor transistors," *IEEE Transactions on Electron Devices*, vol. ED-13, no. 4, pp. 410–414, Apr. 1966.

[158] B. Soltanian and P. R. Kinget, "Tail current-shaping to improve phase noise in LC voltage-controlled oscillators," *IEEE Journal of Solid-State Circuits*, vol. 41, no. 8, pp. 1792–1802, Aug. 2006.

[159] K. Kwok and H. C. Luong, "Ultra-low-voltage high-performance CMOS VCOs using transformer feedback," *IEEE Journal of Solid-State Circuits*, vol. 40, no. 3, pp. 652–660, Mar. 2005.

[160] L. Fanori and P. Andreani, "Class-D CMOS oscillators," *IEEE Journal of Solid-State Circuits*, vol. 48, no. 12, pp. 3105–3119, Dec. 2013.

[161] A. Visweswaran, R. B. Staszewski, and J. R. Long, "A clip-and-restore technique for phase desensitization in a 1.2V 65nm CMOS oscillator for cellular mobile and base stations," in *IEEE International Solid-State Circuits Conference*, San Francisco, CA, USA, Feb. 2012, pp. 350–352.

[162] M. Babaie and R. B. Staszewski, "A class-F CMOS oscillator," *IEEE Journal of Solid-State Circuits*, vol. 48, no. 12, pp. 3120–3133, Dec. 2013.

[163] W. F. Egan, *Frequency synthesis by phase lock.* New York, Wiley-Interscience, 1981.

[164] R. Adler, "A study of locking phenomena in oscillators," *Proceedings of the IEEE*, vol. 61, no. 10, pp. 1380–1385, Oct. 1973.

[165] K. Kurokawa, "Injection locking of microwave solid-state oscillators," *Proceedings of the IEEE*, vol. 61, no. 10, pp. 1386–1410, Oct. 1973.

[166] Sheng Ye, L. Jansson, and I. Galton, "A multiple-crystal interface PLL with VCO realignment to reduce phase noise," *IEEE Journal of Solid-State Circuits*, vol. 37, no. 12, pp. 1795–1803, Dec. 2002.

[167] A. Elshazly, R. Inti, B. Young, and P. K. Hanumolu, "Clock multiplication techniques using digital multiplying delay-locked loops," *IEEE Journal of Solid-State Circuits*, vol. 48, no. 6, pp. 1416–1428, June 2013.

[168] S. Levantino, G. Marucci, G. Marzin, A. Fenaroli, C. Samori, and A. L. Lacaita, “A 1.7 GHz fractional-N frequency synthesizer based on a multiplying delay-locked loop,” *IEEE Journal of Solid-State Circuits*, vol. 50, no. 11, pp. 2678–2691, Nov. 2015.

[169] S. Kundu, B. Kim, and C. H. Kim, “A 0.2-to-1.45GHz subsampling fractional-N all-digital MDLL with zero-offset aperture PD-based spur cancellation and in-situ timing mismatch detection,” in *IEEE International Solid-State Circuits Conference (ISSCC)*, San Francisco, CA, USA, Jan. 2016, pp. 326–327.

[170] B. M. Helal, M. Z. Straayer, G. Wei, and M. H. Perrott, “A highly digital MDLL-based clock multiplier that leverages a self-scrambling time-to-digital converter to achieve subpicosecond jitter performance,” *IEEE Journal of Solid-State Circuits*, vol. 43, no. 4, pp. 855–863, Apr. 2008.

[171] H. Kim, Y. Kim, T. Kim, H. Park, and S. Cho, “A 2.4GHz 1.5mW digital MDLL using pulse-width comparator and double injection technique in 28nm CMOS,” in *IEEE International Solid-State Circuits Conference (ISSCC)*, San Francisco, CA, USA, Jan. 2016, pp. 328–329.

[172] S. Yang, J. Yin, P. Mak, and R. P. Martins, “A 0.0056-mm^2 -249-dB-FoM all-digital MDLL using a block-sharing offset-free frequency-tracking loop and dual multiplexed-ring VCOs,” *IEEE Journal of Solid-State Circuits*, vol. 54, no. 1, pp. 88–98, Jan. 2019.

[173] S. Choi, S. Yoo, and J. Choi, “A 185fs$_{rms}$-integrated-jitter and -245dB FOM PVT-robust ring-VCO-based injection-locked clock multiplier with a continuous frequency-tracking loop using a replica-delay cell and a dual-edge phase detector,” in *IEEE International Solid-State Circuits Conference (ISSCC)*, San Francisco, CA, USA, Jan. 2016, pp. 194–195.

[174] N. Da Dalt, “An analysis of phase noise in realigned VCOs,” *IEEE Transactions on Circuits and Systems II: Express Briefs*, vol. 61, no. 3, pp. 143–147, Mar. 2014.

[175] X. Gao, E. Klumperink, G. Socci, M. Bohsali, and B. Nauta, “A 2.2GHz sub-sampling PLL with 0.16ps$_{rms}$ jitter and -125dBc/Hz in-band phase noise at 700W loop-components power,” in *Symposium on VLSI Circuits*, Honolulu, HI, USA, June 2010, pp. 139–140.

[176] J. Sharma and H. Krishnaswamy, “A dividerless reference-sampling RF PLL with -253.5dB jitter FOM and <-67dBc reference spurs,” in *IEEE International Solid*

- *State Circuits Conference - (ISSCC)*, San Francisco, CA, USA, Feb. 2018, pp. 258–260.

[177] A. Sharkia, S. Mirabbasi, and S. Shekhar, “A 0.01mm^2 4.6-to-5.6GHz sub-sampling type-I frequency synthesizer with -254dB FOM,” in *IEEE International Solid - State Circuits Conference - (ISSCC)*, San Francisco, CA, USA, Feb. 2018, pp. 256–258.

[178] D. Lee and P. P. Mercier, “AMASS PLL: An active-mixer-adopted sub-sampling PLL achieving an FOM of -255.5dB and a reference spur of -66.6dBc,” in *IEEE Symposium on VLSI Circuits*, Honolulu, HI, USA, June 2018, pp. 181–182.

[179] Z. Zhang, G. Zhu, and C. P. Yue, “A 0.65V 12-to-16GHz sub-sampling PLL with 56.4fs$_{\mathrm{rms}}$ integrated jitter and -256.4dB FoM,” in *IEEE International Solid- State Circuits Conference - (ISSCC)*, San Francisco, CA, USA, Feb. 2019, pp. 488–490.

[180] Y.-Y. Jau, E. Miron, A. Post, N. Kuzma, and W. Happer, “Push-pull optical pumping of pure superposition states,” *Physical review letters*, vol. 93, no. 16, p. 160802, Oct. 2004.

[181] S. Kargapoltsev, J. Kitching, L. Hollberg, A. Taichenachev, V. Velichansky, and V. Yudin, “High-contrast dark resonance in σ+-σ-optical field,” *Laser Physics Letters*, vol. 1, no. 10, p. 495, Oct. 2004.

[182] P. Hemmer, S. Ezekiel, and C. Leiby, “Stabilization of a microwave oscillator using a resonance Raman transition in a sodium beam,” *Optics letters*, vol. 8, no. 8, pp. 440–442, Aug. 1983.

[183] N. Castagna, R. Boudot, S. Guerandel, E. De Clercq, N. Dimarcq, and A. Clairon, “Investigations on continuous and pulsed interrogation for a CPT atomic clock,” *IEEE Transactions on Ultrasonics, Ferroelectrics, and Frequency Control*, vol. 56, no. 2, pp. 246–253, Feb. 2009.

[184] J. Thomas, P. Hemmer, S. Ezekiel, C. Leiby Jr, R. Picard, and C. Willis, “Observation of Ramsey fringes using a stimulated, resonance Raman transition in a sodium atomic beam,” *Physical Review Letters*, vol. 48, no. 13, pp. 867–870, Mar. 1982.

[185] V. Letokhov, V. Minogin, and B. Pavlik, “Cooling and trapping of atoms and molecules by a resonant laser field,” *Optics Communications*, vol. 19, no. 1, pp. 72–75, Oct. 1976.

[186] V. Balykin, V. Letokhov, and V. Mushin, "Observation of the cooling of free sodium atoms in a resonance laser field with a scanning frequency," *JETP lett*, vol. 29, no. 10, pp. 560–564, May 1979.

[187] V. Balykin, "Cyclic interaction of Na atoms with circularly polarized laser radiation," *Optics Communications*, vol. 33, no. 1, pp. 31–36, Apr. 1980.

[188] J. V. Prodan and W. D. Phillips, "Chirping the light-fantastic? recent NBS atom cooling experiments," *Progress in Quantum Electronics*, vol. 8, no. 3-4, pp. 231–235, 1984.

[189] W. Ertmer, R. Blatt, J. Hall, and M. Zhu, "Laser manipulation of atomic beam velocities: demonstration of stopped atoms and velocity reversal," *Physical review letters*, vol. 54, no. 10, pp. 996–999, Mar. 1985.

[190] S. Pollock, J. Cotter, A. Laliotis, and E. Hinds, "Integrated magneto-optical traps on a chip using silicon pyramid structures," *Optics Express*, vol. 17, no. 16, pp. 14 109–14 114, Aug. 2009.

[191] S. Pollock, J. Cotter, A. Laliotis, F. Ramirez-Martinez, and E. Hinds, "Characteristics of integrated magneto-optical traps for atom chips," *New Journal of Physics*, vol. 13, no. 4, p. 043029, Apr. 2011.

[192] C. Nshii, M. Vangeleyn, J. Cotter, P. Griffin, E. Hinds, C. Ironside, P. See, A. Sinclair, E. Riis, and A. Arnold, "A surface-patterned chip as a strong source of ultracold atoms for quantum technologies," *Nature nanotechnology*, vol. 8, no. 5, pp. 321–324, Apr. 2013.

[193] M. Schioppo, R. C. Brown, W. F. McGrew, N. Hinkley, R. J. Fasano, K. Beloy, T. H. Yoon, G. Milani, D. Nicolodi, J. Sherman, *et al.*, "Ultrastable optical clock with two cold-atom ensembles," *Nature Photonics*, vol. 11, no. 1, pp. 48–53, Nov. 2017.

[194] F. Riehle, "Towards a redefinition of the second based on optical atomic clocks," *Comptes Rendus Physique*, vol. 16, no. 5, pp. 506–515, June 2015.

[195] J. Reichert, R. Holzwarth, T. Udem, and T. W. Haensch, "Measuring the frequency of light with mode-locked lasers," *Optics communications*, vol. 172, no. 1-6, pp. 59–68, Dec. 1999.

[196] S. A. Diddams, D. J. Jones, J. Ye, S. T. Cundiff, J. L. Hall, J. K. Ranka, R. S. Windeler, R. Holzwarth, T. Udem, and T. Hänsch, "Direct link between microwave

and optical frequencies with a 300 THz femtosecond laser comb," *Physical Review Letters*, vol. 84, no. 22, pp. 5102–5105, May 2000.

[197] D. J. Jones, S. A. Diddams, J. K. Ranka, A. Stentz, R. S. Windeler, J. L. Hall, and S. T. Cundiff, "Carrier-envelope phase control of femtosecond mode-locked lasers and direct optical frequency synthesis," *Science*, vol. 288, no. 5466, pp. 635–639, Apr. 2000.

[198] T. Udem, R. Holzwarth, and T. W. Hänsch, "Optical frequency metrology," *Nature*, vol. 416, no. 6877, pp. 233–237, Mar. 2002.

[199] S. T. Cundiff and J. Ye, "Colloquium: femtosecond optical frequency combs," *Reviews of Modern Physics*, vol. 75, no. 1, pp. 325–342, Jan. 2003.

[200] T. Fortier, D. J. Jones, and S. T. Cundiff, "Phase stabilization of an octave-spanning Ti: sapphire laser," *Optics letters*, vol. 28, no. 22, pp. 2198–2200, Nov. 2003.

Appendix A

Publication List

A.1 Journal Papers

- **Haosheng Zhang**, Hans Herdian, Aravind Tharayil Narayanan, Atsushi Shirane, Mitsuru Suzuki, Kazuhiro Harasaka, Kazuhiko Adachi, Shinya Yanagimachi, Kenichi Okada, "ULPAC: A Miniaturized Ultra-low-power Atomic Clock," *IEEE Journal of Solid-State Circuits (JSSC)*, vol. 54, no. 11, pp. 3135-3148, Nov. 2019 .

- **Haosheng Zhang**, Aravind Tharayil Narayanan, Hans Herdian, Bangan Liu, Rui Wu, Atsushi Shirane, Kenichi Okada, "A Power-Efficient Pulse-VCO for Chip-Scale Atomic Clock," *IEICE Transactions on Electronics*, vol. E102-C, no. 4, pp. 276-286, April 2019.

A.2 International Conferences and Workshops

- **Haosheng Zhang**, Aravind Tharayil Narayanan, Hans Herdian, Bangan Liu, Yun Wang, Atsushi Shirane, Kenichi Okada, "0.2mW 70fs_{rms}-Jitter Injection-Locked PLL Using De-Sensitized SSPD-Based Injecting-Time Self-Alignment Achieving -270dB FoM and -66dBc Reference Spur," *IEEE Symposium on VLSI Circuits (VLSI)*, Kyoto, Japan, pp. C38-C39, June 2019.

- **Haosheng Zhang**, Hans Herdian, Aravind Tharayil Narayanan, Atsushi Shirane, Mitsuru Suzuki, Kazuhiro Harasaka, Kazuhiko Adachi, Shinya Yanagimachi, Kenichi Okada, "Ultra-Low-Power Atomic Clock for Satellite Constellation with 2.2×10^{-12} Long-Term Allan Deviation Using Cesium Coherent Population Trapping," *IEEE International Solid- State Circuits Conference (ISSCC)*, San Francisco, CA, USA, pp. 462-464, Feb. 2019.

- **Haosheng Zhang**, Hans Herdian, Aravind Tharayil Narayanan, Bangan Liu, Rui Wu, Atsushi Shirane, Kenichi Okada, Kenichi Okada, "A -194dBc/Hz FoM VCO with Low-Supply Sensitivity for Ultra-Low-Power Atomic Clock," *IEEE Asia Pacific Microwave Conference (APMC)*, Kyoto, Japan, pp. 788-790, Nov. 2018.

- **Haosheng Zhang**, Aravind Tharayil Narayanan, Bangan Liu, Atsushi Shirane, Kenichi Okada, Akira Matsuzawa, "A pulse VCO with tail filter," *IEEE Asia Pacific Microwave Conference (APMC)*, Kuala Lumpar, Malaysia, pp. 942-945, Nov. 2017.

A.3 Domestic Conferences and Workshops

- **Haosheng Zhang**, Kenichi Okada, "CMOS probing and locking loop for ultra-low-power atomic clock," *VDEC Designers Forum*, Tendo, Sep. 2019.

- **Haosheng Zhang**, Hans Herdian, Atsushi Shirane, Kenichi Okada, "0.2mW 70fs jitter injection locked PLL," *IEICE Society Conference*, Osaka, C-12-20, Sep. 2019.

- **Haosheng Zhang**, Aravind Tharayil Narayanan, Hans Herdian, Bangan Liu, Yun Wang, Atsushi Shirane, Kenichi Okada, "0.2mW 70fs_{rms}-Jitter Injection-Locked PLL Using De-Sensitized SSPD-Based Injecting-Time Self-Alignment Achieving -270dB FoM and -66dBc Reference Spur," *VLSI Domestic Report*, Tokyo, Japan, June 2019.

- **Haosheng Zhang**, Hans Herdian, Aravind Tharayil Narayanan, Atsushi Shirane, Mitsuru Suzuki, Kazuhiro Harasaka, Kazuhiko Adachi, Shinya Yanagimachi, Kenichi Okada, "An ultra-low-power atomic clock based on CMOS probing and locking loop," *LSI and System workshop*, Tokyo, May 2019.

- **Haosheng Zhang**, Hans Herdian, Aravind Tharayil Narayanan, Atsushi Shirane, Mitsuru Suzuki, Kazuhiro Harasaka, Kazuhiko Adachi, Shinya Yanagimachi, Kenichi Okada, "Ultra-Low-Power Atomic Clock for Satellite Constellation with 2.2×10^{-12} Long-Term Allan Deviation Using Cesium Coherent Population Trapping," *ISSCC Domestic Report*, Osaka, March 2019.

- **Haosheng Zhang**, Ashbir Aviat Fadila, Atsushi Shirane, Kenichi Okada, "A High-Power-Efficiency Stacked PA and VCO Cell," *IEICE Society Conference*, Kanazawa, C-12-25, Sep. 2018.

- **Haosheng Zhang**, Kenichi Okada and Akira Matsuzawa, "A Synthesizable High Resolution Linear DTC," *IEICE General Conference*, Nagoya, C-12-16, March 2017.

- **Haosheng Zhang**, Aravind Tharayil Narayanan, Kenichi Okada and Akira Matsuzawa, "An Analysis of Pulse-VCO with Tail-Filter," *IEICE Society Conference*, Sapporo, Hokkaido, C-12-6, Sep. 2016.

A.4 Co-author

A.4.1 Journal Papers

- Yun Wang, Rui Wu, Jian Pang, Dongwon You, Ashbir Aviat Fadila, Rattanan Saengchan, Xi Fu, Daika Matsumoto, Takeshi Nakamura, Ryo Kubozoe, Masaru Kawabuchi, Bangan Liu, **Haosheng Zhang**, Junjun Qiu, Hanli Liu, Wei Deng, Naoki Oshima, Keiichi Motoi, Shinichi Hori, Kazuaki Kunihiro, Tomoya Kaneko, Atsushi Shirane, and Kenichi Okada, "A 39-GHz 64-Element Phased-Array Transceiver with Built-in Phase and Amplitude Calibration for Large-Array 5G NR in 65-nm CMOS," *IEEE Journal of Solid-State Circuits (JSSC)*, 2019 **[under review]**.

- Yun Wang, Bangan Liu, Rui Wu, Hanli Liu, Aravind Tharayil Narayanan, Jian Pang, Ning Li, Toru Yoshioka, Yuki Terashima, **Haosheng Zhang**, Dexian Tang, Makihiko Katsuragi, Daeyoung Lee, Sungtae Choi, Kenichi Okada, "A 60-GHz 3.0-Gb/s Spectrum Efficient BPOOK Transceiver for Low-Power Short-Range Wireless in 65-nm CMOS," *IEEE Journal of Solid-State Circuits (JSSC)*, vol. 54, no. 5, pp. 1363-1374, May 2019.

- Bangan Liu, Huy Cu Ngo, Kengo Nakata, Wei Deng, Yuncheng Zhang, Junjun Qiu, Toru Yoshioka, Jun Emmei, Jian Pang, Aravind Tharayil Narayanan, **Haosheng Zhang**, Dongsheng Yang, Hanli Liu, Teruki Someya, Atsushi Shirane, and Kenichi Okada, "A 0.4-ps-Jitter -52-dBc-Spur Synthesizable Injection-Locked PLL With Self-Clocked Nonoverlap Update and Slope-Balanced Subsampling BBPD," *IEEE Solid-State Circuits Letters (JSSC-L)*, vol. 2, no. 1, pp.5-8, Jan. 2019.

- Bangan Liu, Yun Wang, Jian Pang, **Haosheng Zhang**, Dongsheng Yang, Aravind Tharayil Narayanan, DaeYoung Lee, SungTae Choi, Rui Wu, Kenichi Okada, and Akira Matsuzawa, "A low-power pulse-shaped duobinary ASK modulator for IEEE 802.11ad compliant 60GHz transmitter in 65nm CMOS," *IEICE Transactions on Electronics*, vol. E101-C, no. 2, pp.126-134, Feb. 2018.

A.4.2 Conferences

- Hans Herdian, **Haosheng Zhang**, Aravind Tharayil Narayanan, Atsushi Shirane, Kenichi Okada, "10GHz Varactor-less VCO with Helium-3 Ion Irradiated Inductor," *IEEE Asia-Pacific Microwave Conference (APMC)*, Singapore, Dec. 2019 [**Accepted].**

- Yun Wang, Rui Wu, Jian Pang, Dongwon You, Ashbir Aviat Fadila, Rattanan Saengchan, Xi Fu, Daiki Matsumoto, Takeshi Nakamura, Ryo Kubozoe, Masaru Kawabuchi, Bangan Liu, **Haosheng Zhang**, Junjun Qiu, Hanli Liu, Naoki Oshima, Keiichi Motoi, Shinichi Hori, Kazuaki Kunihiro, Tomoya Kaneko, Atsushi Shirane and Kenichi Okada, "A 39GHz Phased-Array CMOS Transceiver with Built-in Calibration for Large-Array 5G NR," *IEEE Radio Frequency Integrated Circuits Symposium (RFIC)*, Boston, MA, USA, pp. 279-282, June 2019.

- Bangan Liu, Yuncheng Zhang, Junjun Qiu, Wei Deng, Zule Xu, **Haosheng Zhang**, Jian Pang, Yun Wang, Rui Wu, Teruki Someya, Atsushi Shirane, and Kenichi Okada, "An HDL-described Fully-synthesizable Sub-GHz IoT Transceiver with Ring Oscillator based Frequency Synthesizer and Digital Background EVM Calibration," *IEEE Custom Integrated Circuits Conference (CICC)*, Austin, TX, USA, pp. 1-4, April 2019.

- Bangan Liu, Huy Cu Ngo, Kengo Nakata, Wei Deng, Yuncheng Zhang, Junjun Qiu, Torn Yoshioka, Jun Emmei, **Haosheng Zhang**, Jian Pang, Aravind Tharayil Narayanan, Dongsheng Yang, Hanli Liu, Kenichi Okada, and Akira Matsuzawa, "A 1.2ps-jitter fully-synthesizable fully-calibrated fractional-N injection-locked PLL using true arbitrary nonlinearity calibration technique," *IEEE Custom Integrated Circuits Conference (CICC)*, San Diego, CA, USA, pp. 1-4, April 2018.

- Yun Wang, Bangan Liu, Hanli Liu, Aravind Tharayil Narayanan, Jian Pang, Ning Li, Torn Yoshioka, Yuki Terashima, **Haosheng Zhang**, Dexian Tang, Makihiko Katsuragi, Daeyoung Lee, Sungtae Choi, Rui Wu, Kenichi Okada, and Akira Matsuzawa, "A 100mW 3.0Gb/s spectrum efficient 60GHz Bi-Phase OOK CMOS transceiver," *IEEE Symposium on VLSI Circuits (VLSI)*, Kyoto, Japan, pp. C298-C299, June 2017.

- Hans Herdian, **Haosheng Zhang**, Atsushi Shirane, Kenichi Okada, "Wide Tuning-Range VCO Implementation with Helium-3 Irradiated Inductor," *IEICE Society Conference*, Kanazawa, C-12-26, Sep. 2018.

Appendix B

List of Abbreviations

AC: alternating current

ADC: analog to digital converter

AM: amplitude-modulated

BBPD: bang-bang phase detector

CMOS: complementary metal-oxide-semiconductor

CP: charge pump

CPT: coherent population trapping

CSAC: chip-scale atomic clock

DAC: digital analog converter

DBR: Distributed Bragg reflector

DFF: D-type flip flop

DKS: dissipative Kerr-solition

DSM: delta-sigma modulator

DSSFLL: de-sensitized sub-sampling phase detector

DZ: dead-zone

dc: direct current

ECDL: external cavity diode laser

ENF: excess noise factor

FCW: frequency control word

FLL: frequency locking loop

FM: frequency-modulated

FoM: figure of merit

FWHM: full width at half maximum

GEO: geosynchronous

GNSS: global navigation satellite system

GPS: global positioning system

HPF: high pass filter

IL: injection-locked

LANS: local area networks

LC: inductor-capacitor

LEO: low earth orbit

LF: low pass filter

LFSR: linear-feedback shift register

MCU: microcontroller unit

MCXO: microcomputer compensated crystal oscillator

MEMS: micro-electro-mechanical system

MIMO: multiple-input and multiple-output

MMD: multiple-module divider

MOT: magneto-optical trap

MU: multiple-cell upset

ND: neutral density

NIST: National Institute of Standards and Technology

NTF: noise transfer function

OA: oxide aperture

OCXO: oven compensated crystal oscillator

PA: power amplifier

PCB: printed circuit board

PD: photodetector

PDOP: position dilution of precision

PFD: phase frequency detector

PLL: phase-locked loop

PM: phase-modulated

PN: phase noise

PVT: process, voltage and temperature variations

RC: resistor-capacitor

RF: radio frequency

RMS: root-mean-square

SET: single-event transient

SEU: single-event upset

SI: International System of Units

SOI: silicon on insulator

SPI: serial peripheral interface

SSA: signal source analyzer

SSPD: sub-sampling phase detector

SoC: system on chip

S/N: signal to noise

TAI: International Atomic Clock

TCXO: temperature compensated crystal oscillator

TDC: time to digital converter

TMR: triple-modular-redundant

ToF: time of flight

ULPAC: Ultra-low-power atomic clock

UTC: Coordinated Universal Time

VAU-BS: unmanned-aerial-vehicle base stations

VCO: voltage-controlled oscillator

VCSEL: vertical-cavity surface-emitting laser

1-PPS: one-pulse-per-second

3D: three dimensional